Climate Change Implications on Rainfall Erosivity and Intensity Duration Frequency Curves over the Southeast United States

by

Takhellambam Bijoychandra Singh

A dissertation submitted to the Graduate Faculty of
Auburn University
in partial fulfillment of the
requirements for the Degree of
Doctor of Philosophy

Auburn, Alabama
August 5, 2023

Keywords: Climate Change, Precipitation Disaggregation, Erosivity
Neural Network, IDF Curves, Uncertainty

Approved by

Jasmeet Lamba, Chair, Associate Professor, Department of Biosystem Engineering
Puneet Srivastava, Co-chair, Professor, Associate Dean for Research, and Associate Director of Maryland Agricultural Experiment Station in the College of Agriculture and Natural Resources, University of Maryland
Di Tian, Associate Professor, Department of Crop, Soil, and Environmental Sciences
Roberto Molinari, Assistant Professor, Department of Mathematics and Statistics

Abstract

Climate change impacts on precipitation characteristics will alter the hydrologic characteristics, such as peak flows, time to peak, and soil erosion potential. However, many of the currently available climate change datasets are provided at temporal and spatial resolutions that are inadequate to quantify projected changes in the hydrologic characteristics of a watershed. Therefore, it is critical to temporally disaggregate coarse-resolution precipitation data to finer resolutions for studies sensitive to precipitation characteristics. First, this study generated novel 15-minute precipitation datasets from hourly precipitation datasets obtained from five NA-CORDEX downscaled climate models under Representative Concentration Pathway (RCP)8.5 scenario for the historical (1970-1999) and projected (2030-2059) years over the Southeast United States using a modified version of a stochastic method. The results showed the conservation of mass of the precipitation inputs. Furthermore, the probability of zero precipitation, variance of precipitation, and maximum precipitation in the disaggregated data matched well with the observed precipitation characteristics. The generated 15-minute precipitation data can be used in all scientific studies that require precipitation data at that resolution.

Secondly, the datasets generated from objective one were further applied to estimate projected erosivity (R-factor), which determines the erosive power of rainfall. The magnitude and scope of these future changes in the erosive power of rainfall remain largely unknown, particularly at finer resolutions and local scales because previous studies have relied on aggregated (hourly, daily) rainfall data. The erosivity for the region was calculated using the RUSLE2 erosivity calculation method without data limitation. Ensemble results for projected values (as compared to historical values) showed a projected increase in annual average precipitation, erosivity, and erosivity density by 14%, 47%, and 29%, respectively, over the southeast region from 2030 to 2059. The

future ensemble model showed an average annual R-factor of 11237±1299 MJ mm ha^{-1} h^{-1} yr^{-1}. These findings suggest that changes in rainfall intensity, rather than only precipitation amount, may drive future changes in erosivity. However, the study is associated with limitations due to bias correction and downscaling of the precipitation dataset and obscuring the result of projected erosivity. In general, coastal and mountainous regions are expected to experience the greatest absolute increase in erosivity, while other inland areas are expected to experience the greatest relative change. This study offers a novel examination of projected future precipitation characteristics in terms of erosivity and potential future erosion.

Furthermore, future projected rainfall Intensity-Duration-Frequency (IDF) curves were developed for the Southeast United States using Generalized extreme value (GEV) distribution with disaggregated sub-hourly (15-, 30-, and 45-min) monthly maximum rainfall from 2030 to 2059 using the five climate models under the RCP8.5 scenario. A computationally efficient feed-forward back-propagation Artificial Neural Network (ANN)-based approach was found to be significantly superior for disaggregating rainfall compared to the stochastic model with an average Nash–Sutcliffe efficiency (NSE) ranging from 0.67 to 0.84. Kolmogorov-Smirnov (KS) test confirmed at a 5% significance level that the annual maximum rainfalls come from Gumbel extreme value distributions. The study found that there is an increasing intensity of future projected rainfall in the range of 7% to 36% in comparison to the historical period. The spatial variation in future projected extreme rainfall depths showed that the Gulf-Atlantic coast and the Appalachian Mountains are expected to receive more extreme rainfalls.

Finally, uncertainties associated with climate studies are of considerable interest, particularly extreme rainfall analysis for providing confidence to the relevant stakeholders for designing hydrological structures. Therefore, this study quantified the uncertainties associated with the

rainfall IDF Curves for the largest cities of the Southeast United States using the ANN and bootstrapping resampling technique along with Gumbel distribution. Results showed no significant differences while disaggregating hourly to sub-hourly (15-, 30-, and 45-min) monthly maximum rainfall with or without hyperparameter tuning using random search. Additionally, bias correction significantly improved the rainfall IDF curves rejecting the null hypothesis of no difference using Welch two sample t-test. Overall, the minimum and maximum of annual maximum rainfall intensities were found in a range of 38 to 55 mm h^{-1} and 143 to 210 mm h^{-1}, respectively. Further studies are needed to improve the uncertainty quantification of human error in climate modeling and the randomness of natural processes in datasets.

Acknowledgments

First and foremost, my heartfelt gratitude goes to my supervisors, Dr. Jasmeet Lamba and Prof. Puneet Srivastava, for guiding me throughout the Ph.D. journey. This journey would not have been possible without their help. I would also like to thank my committee members, Drs. Di Tian and Roberto Molinari, for their help and advice in steering me in the right direction. In addition, Prof. Latif Kalin for serving as my thesis reader. I would also like to extend my sincere thanks to Prof. Nedret Billor for allowing me to pursue a minor in statistics.

My sincere gratitude goes to the Department of Biosystem Engineering's faculty and staff members, Richard Morbidelli, Amber Denham, Bionca King, Caroline Whiting, Bobby Epling, and Erin Wittwer, and to USDA ARS Scientist Dr. Tom Way. In addition, many thanks to Sherry Ray (graduate advisor) and the Office of Information Technology (OIT) staff members. Their constant support along with other Auburn University facilities support helped in the smooth completion of my degree work.

I would also want to say thank you to Dr. Ryan P. McGehee and Dr. Wenpeng Zhao for their collaborative work. Also, I would like to thank my friends Dr. Hemendra Kumar, Tayler Schillerberg, Danielle Tadych, Dr. Parisa Asadi, Rashmi Sahu, Suman Budhathoki, Dr. Ritesh Karki, Dr. Tawsif Rahman, Dr. Poulamy Roy, Kritika Malhotra, Preetika Kaur, Vishawjot Sandhu, & Gurparshad Brar for their friendship and support.

A special thanks to all family members of Richard Morbidelli; Nicholas Morbidelli and his family, Louann, Mike, Tessa, Granny (Teresa), and Jake and his family. Their support and help made another home away from home.

I would be remiss if I didn't acknowledge my friends and brothers Bijeshor Mayanglambam, Dr. Suranjoy Singam, Sardananda Yengkhom, Dr. Vipej Sansam, Olivia Hidangmayum, Chinglen

Tensubam, Mahesh Salam, Roben Salam, Bijen Khumukcham, Dr Doreshor Khwairakpan, Er. Dayananda Huidrom and Er. Jiten Hijam. Their support was vital in my completing this long Ph.D. journey.

Finally, my sincere thanks to my family members; ema/mom (Takhellambam ongbi Thingujam Jamini), dad (Bheigyachandra Takhellambam), sister (Loitongbam ongbi Takhellambam Brojeshori), brother (Gopi Takhellambam), grandma/ebok (Akashini Thingujam), epu or grandpa (Late Ningthoujao Thingujam), Bidyashori Oinam and others for their support.

I will cherish the memories of this adventure until the day I die. Thank you for your wonderful hospitality, Auburn. WAR EAGLE!

Bijoychandra Takhellambam

August 2023

Table of Contents

List of Tables

List of Figures

List of Abbreviations

AH	Agricultural Handbook
AMS	annual maxima series
ANN	Artificial Neural Network
BC	Bias correction
BF	Brown and Foster
CDD	consecutive dry days
CMIP	Coupled Model Intercomparison Project
COV	Coefficient of variation
DS	Downscaling
ED	Erosivity density
Eq.	Equation
F	Future
GCM	Global Circulation Model
GEV	generalized extreme value
H	historical
h	hour
ha	Hectare
H_O	Null hypothesis
I	Intensity
IQR	Inter quartile range
Max.	maximum
Med.	median

Min. minimum

min minute

MJ Megajoule

MM McGregor and Mutchler

mm millimeter

NA CORDEX-North American Coordinated Regional Climate Downscaling Experiment

Obs.Abs.Diff. Observed absolute difference

Obs.Rel.Diff. Observed relative difference

PRCPTOT annual total precipitation

QDM quantile delta mapping

R Annual Rainfall Erosivity

R-factor Annual Rainfall Erosivity

RCM Regional Circulation Model

RCP Representative Concentration Pathway

RX5day maximum consecutive-5-day precipitation

R2 Revised Universal Soil Loss Equation 2

RUSLE2 Revised Universal Soil Loss Equation 2

R20mm Very heavy precipitation days

R95pTOT annual total precipitation with daily precipitation above 95th percentile

Sim.Abs.Diff.Simulated absolute difference

Sim.Rel.Diff.Simulated relative difference

Std.Dev. Standard deviation

Stoch Stochastic

CHAPTER 1

Introduction

1.1 Background and Problem Statement

The term *climate* is defined as the average weather for a given period of time i.e., months, thousands, or millions of years (IPCC, 2018). The World Meteorological Organization specifies 30 years as the classical period for averaging weather variables, particularly surface variables of temperature, precipitation, and wind. However, in the last few decades, there is a change in climate due to natural and anthropogenic activities such as volcanic eruption, burning of fossil fuels, deforestation, and other activities that increase the greenhouse gases in the atmosphere. According to United Nations Framework Convention on Climate Change (UNFCCC), "climate change" is defined as "*a change of climate which is attributed directly or indirectly to human activity that alters the composition of the global atmosphere and which is in addition to natural climate variability observed over comparable time periods*" (IPCC, 2018).

The media and decision-makers, especially in the United States, routinely claim that climate science is highly uncertain (Oreskes, 2004). However, there is a consensus on climate change due to human activities among scientists, particularly in group reports of the Intergovernmental Panel on Climate Change (IPCC) (Cook et al., 2016; IPCC, 2018; Oreskes, 2004). Hansen et al. (2006) reported that there is an increase in global surface temperature at a rate of 0.2℃ per decade. In addition, Hoegh-Guldberg et al. (2018) found the global mean surface temperature increased up to 0.87°C in 2006-15 relative to the pre-industrial period of 1850-1900. With the current trends of greenhouse gases in the atmosphere, the temperature is projected to increase by 1.5℃ above the pre-industrial level by end of 2052 (Takhellambam et al., 2023).

Climate change is associated with extreme rainfall events leading to more frequent droughts, floods, and soil erosion. For instance, precipitation intensity increases by about 7% with unit degree Celsius of temperature (Trenberth, 2011) resulting in increasing flooding events. An additional effect of climate change is a higher rate of evaporation, thereby, decreasing soil moisture leading to agricultural drought and reducing water supply in many parts of the world (Adams and Peck, 2008).

The southeastern United States in particular has the greatest potential for change in rainfall characteristics (McGehee and Srivastava, 2018). USGCRP (2018) recorded the highest number of daily extreme rainfalls with 3 inches or more during 1990-2010. During this period, extreme rainfall has increased in the range of 16-23% as compared to that of 1900s. This region requires proper adaptation and mitigation measures for climate change, particularly for water resources and the agriculture sectors for sustainable development. This could be achieved through proper planning and actions through reliable and accurate research.

Although there are a large number of future projected climate models that are published or available, all climate models are available in aggregated or fixed intervals such as hourly or daily scales, particularly precipitation datasets. Using these datasets for studies sensitive to precipitation intensity are prone to underestimation. For instance, McGregor et al. (1980) asserted rainfall erosivity calculated with the methodology presented in Agricultural Handbooks 537 (Wischmeier and Smith, 1978) is underestimated. Previous erosion maps, especially those of three Agricultural Handbooks (AH) i.e., AH282 (Wischmeier and Smith, 1965), AH537 (Wischmeier and Smith, 1978), and AH703 (Renard, 1997), underestimated erosivity by 30% compared to the benchmarking studies (McGehee, 2016; McGehee and Srivastava, 2018; McGregor et al., 1995). Moreover, the hydrological modeling using Soil Water Assessment Tool (SWAT) and sub-hourly

data was found to give better performance than both sub-daily and daily scale data (Jeong et al., 2010). One of the main reasons is due to the smoothing or averaged rainfall intensity while using fixed intervals (Takhellambam et al., 2023). A previous study reported that rainfall maximum intensity occurs during 15-min rainfall intervals, therefore using a larger rainfall interval, the intensity is compromised due to averaging (McGehee and Srivastava, 2018).

Previous studies used two broad methods for rainfall disaggregation, i.e., Poisson-cluster models (stochastic simulation) and random cascade models (Choi et al., 2008). These methods use an extensive number of parameters (Choi et al., 2008; Islam et al., 1990; Kossieris et al., 2018; Li et al., 2018; Rodriguez-Iturbe et al., 1988, 1987). These methods involving a greater number of parameters were overcome by Socolofsky et al. (2001) through an efficient stochastic method while generating hourly rainfall datasets from daily scale. The method was further confirmed for successfully generating hourly observed precipitation using daily data (Choi et al., 2008). Mirhosseini et al. (2013) further modified the stochastic method for developing 15-min rainfall using 3-hour data over Alabama, United States. Therefore, our first goal was to develop high-resolution precipitation datasets (15-min) for the projected future scenario under RCP8.5 under five different climate models, owing to the limited availability of reliable rainfall datasets essential for all applicable hydrologic studies sensitive to rainfall intensities.

Additionally, soil erosion which is the removal of topsoil has resulted in reducing crop yield through loss of nutrients and shallowing of reservoirs. One of the major drivers for soil erosion is water through rainfall and runoff. However, the southeastern United States has the greatest potential change in rainfall characteristics under changing climate. Therefore, the potential of rainfall to erode soil also known as rainfall erosivity needs to be quantified. To our knowledge, Biasutti and Seager (2015); Hoomehr et al. (2016); Nearing (2001); Panagos et al. (2022); and

Segura et al. (2014) have estimated future projected rainfall erosivity in the United States. These studies used aggregated rainfall datasets which led to the underestimation of projected rainfall erosivities. Therefore, the second objective of this dissertation was to develop future projected rainfall erosivity map for the southeastern United States using 15-min rainfall data under the RCP8.5 scenario.

Furthermore, hydrologic and hydraulic structures such as dams and culverts are designed based on the stationarity of the rainfall intensity duration frequency (IDF) curves which give a probability of rainfall intensity in a given period (Perica et al., 2013; Soltani et al., 2020; Sun et al., 2019; Zhao et al., 2022a). However, the projected rainfall characteristics under changing climate are found to be non-stationary. This necessitates an update of existing IDF curves using high-temporal resolution rainfall datasets. Moreover, there is an underprediction of rainfall extremes particularly the monthly maximum rainfall dataset while using a stochastic approach. Therefore, the state-of-the-art artificial neural network (ANN) model was hypothesized to perform better in generating the sub-hourly rainfall datasets from the hourly scale. The third goal of this dissertation was to develop rainfall IDF curves using the generated rainfall dataset empowered by ANN.

Lastly, the climate impact assessment for hydrologic and hydraulic modeling is associated with uncertainties mainly due to a lack of understanding of physical processes, insufficient information, or analytical resources (Mirhosseini et al., 2015; Solaiman, 2011). In addition, uncertainty in future projected rainfall models are required to be quantified as rainfall generation mechanism are based on greenhouse gas concentrations in the atmosphere and the carbon cycle (Solaiman, 2011). These associated uncertainties result in inaccurate hydrological modeling that could have an impact on the reliability drawn from the research analysis (Ng et al., 2019). Quantifying uncertainty in climate impact assessment, particularly for extreme rainfall events is necessary for adaptation and

mitigation to climate change. Therefore, an accurate uncertainty estimates help in better decision-making by relevant stakeholders (Katz et al., 2013; Guttorp, 2012). The fourth goal of this dissertation was to quantify the uncertainty associated with the future projected rainfall IDF curves for selected 11 largest cities of the Southeast United States under the RCP8.5 scenario using rainfall datasets of 2030 to 2059.

In summary, the research findings from this dissertation have attempted to significantly improve the understanding of the effect of climate change on precipitation, particularly on soil erosion and extreme rainfall events through developing high-temporal resolution precipitation datasets assuming there is no snowfall in the region. This will make it possible for the stakeholders, including academics, policymakers, and researchers, to develop and assess adaptation and mitigation measures under changing climate in the Southeast United States.

1.2 Objectives

The objectives of this dissertation are provided below:

1. Temporally disaggregate hourly precipitation under changing climate over the Southeast United States.
2. Quantify projected mid-century rainfall erosivity under climate change over the Southeast United States.
3. Develop artificial neural network-empowered projected future rainfall intensity-duration-frequency curves under changing climate; and
4. Quantify uncertainty in rainfall intensity-duration-frequency curves using artificial neural network and bootstrapping resampling technique.

1.3 Dissertation Organization

This dissertation includes five chapters. Chapter 1 discusses the introduction, research background, research gap, and objectives. Chapters 2 – 5 discussed research works that focus on the four distinct objectives. Chapter 2 is focused on the development of 15-minute precipitation for the entire Southeast United States between 2030 and 2059 from 1-hour datasets using a modified stochastic approach. This objective has been published in *Scientific Data* (Takhellambam et al., 2022a). Chapter 3 estimated future projected rainfall erosivity using the data generated from objective 1 for the entire region. This study has also been published in *Science of The Total Environment* (Takhellambam et al., 2023). Chapter 4 improved the disaggregated rainfall of the stochastic approach using ANN for monthly maximum rainfall. Using these improved datasets, future projected rainfall IDF curves were developed. The manuscript is currently under review. Chapter 5 focuses on the quantification of uncertainty associated with projected IDF curves. This is done using state-of-the-art statistical and machine-learning techniques. Finally, chapter 6 provides both summary and suggestions for future work.

CHAPTER 2

Temporal Disaggregation of Hourly Precipitation Under Changing Climate Over the Southeast United States

2.1 Background & Summary

Precipitation is a fundamental input in all practical scientific studies that deal with the hydrological cycle (Savina et al., 2012; Song et al., 2016). For instance, precipitation is the main driver in the Soil and Watershed Assessment Tool (SWAT) (Abbaspour, 2013; Abbaspour et al., 2007; Gassman et al., 2014; Li et al., 2018; Schuol and Abbaspour, 2006; Tuo et al., 2016). In addition, precipitation data is needed for the estimation of rainfall intensity-duration-frequency curves (Ganguli and Coulibaly, 2019; Mirhosseini et al., 2015, 2014, 2013; Srivastav et al., 2014), rainfall erosivity (Almagro et al., 2017; Biasutti and Seager, 2015; Fullhart et al., 2020; Hoomehr et al., 2016; Nearing, 2001; Zhang et al., 2010), and soil loss estimation using Universal Soil Loss Equation (USLE), Revised USLE, and Global Soil Erosion Modeling (Borrelli et al., 2020; Nearing et al., 2017; Oliveira et al., 2013).

In these previous studies, higher-temporal resolution precipitation performed better than aggregated (e.g., hourly, daily) precipitation data. For instance, Jeong et al. (2010) found that the SWAT model built using sub-hourly (15-minute) precipitation outperformed the model built using both coarser sub-daily and daily precipitation data. This is because, among many other reasons, high-temporal resolution precipitation is capable of better prediction of peak flows. While many researchers have estimated rainfall erosivity using aggregated precipitation data(Almagro et al., 2017; Hoomehr et al., 2016; Mondal et al., 2016; Nearing, 2001), using aggregated rainfall data has resulted in underestimation of rainfall erosivity up to or exceeding 30% as compared to the

fixed-intensity precipitation or 'breakpoint' precipitation data (McGregor et al., 1995, 1980; Renard, 1997). The main reason for using fixed-interval precipitation data is the limited availability of high-resolution precipitation data (McGehee, 2016; McGehee and Srivastava, 2018; McGehee et al., 2021b).

Climate projections play a significant role in understanding the future scenarios of scientific studies related to climate (Mishra et al., 2020). In the case of RCM-based climate impact studies, it is recommended to use an ensemble approach for better performance in both model uncertainty and potential outcomes (Meyer et al., 2021). To-date, there are two coordinated RCM ensemble projects for North America, i.e., the North American Regional Climate Change Assessment Program (NARCCAP) and North American-Coordinated Regional Climate Downscaling Experiment (NA-CORDEX) (Mearns et al., 2017, 2009; Scinocca et al., 2016). NARCCAP used four global climate models (GCM) from the third phase of the Coupled Model Inter-comparison Project (CMIP3) along with six RCMs. NA-CORDEX used GCMs from CMIP5 for downscaling with the RCMs. There have been various studies using NA-CORDEX for the assessment of climate impacts, which range from regional to continental in scale (Ganguli and Coulibaly, 2019; Meyer et al., 2021).

In the absence of breakpoint precipitation data, relatively high-resolution, fixed-interval data may serve as a viable alternative when it has been properly corrected for gaps, biases, and precision limitations (McGehee and Srivastava, 2018; McGehee et al., 2021b). There are different types of temporal rainfall disaggregation methods available. These methods can be broadly categorized into two broad methods, i.e., Poisson-cluster models (stochastic simulation) and random cascade models (Choi et al., 2008). However, these methods require a large number of parameters (Choi

et al., 2008; Islam et al., 1990; Kossieris et al., 2018; Li et al., 2018; Rodriguez-Iturbe et al., 1988, 1987).

To overcome the requirement of a large number of parameters in rainfall disaggregation, Socolofsky et al. (2001) presented a more computationally efficient stochastic method to disaggregate daily to hourly precipitation. This method relies on a single parameter, which is the smallest storm event value for each month/season. The method had been further evaluated for its performance and was found to be satisfactory in the replication of hourly observed precipitation using daily data (Choi et al., 2008). The method was modified and found to be satisfactory for generating 15-min precipitation over Alabama, USA using 3-hour precipitation (Mirhosseini et al., 2013). Therefore, in this study, we used precipitation from NA-CORDEX with the highest temporal resolution available, i.e., hourly data from the RCP8.5 scenario for five GCM-RCMs. As a result, we have developed 15-min precipitation datasets for each of the five climate models of NA-CORDEX under the RCP8.5 scenario over the Southeast US using a modified stochastic disaggregation method. We used the quantile delta mapping method for removing the bias associated with the precipitation data generated by the climate models. Bias-correction significantly improved the intensities as well as the annual precipitation frequencies for all the climate models. The bias-corrected hourly precipitation data were disaggregated to generate 15-min precipitation for both historical (1970-1999) and projected (2030-2059) years. The quality assessment of the generated 15-minute precipitation over the Southeast US showed that all the climate models provided similar results. We can conclude that the resulting finer temporal resolution precipitation data can be used in scientific studies that deal with the hydrological cycle (requires precipitation) over the Southeastern US. However, given the limitations of the disaggregation method, some precipitation characteristics such as intensities may still differ from

observed precipitation characteristics. Potential users should still evaluate these qualities before using this dataset in their respective studies. Therefore, while this dataset represents an improvement in intensities over using hourly climate projections from climate models, it may still be of insufficient quality for those applications that are sensitive to precipitation intensity.

2.2 Methods

A summary of the methods used in this study is organized as follows: 1) study area and data 2) bias correction of the climate model data, 3) the modified stochastic disaggregation method, and 4) performance assessment and characterization.

2.2.1 Study area and data

The climate of the Southeast United States is distinct from the rest of the country due to its proximity to the Atlantic Ocean and Gulf of Mexico (Ingram et al., 2013; Kunkel et al., 2013). The region experiences frequent extreme weather due to its warm humid climate (Allan and Soden, 2008; Easterling et al., 2017; Ingram et al., 2013). In the past 30 years (1990-2020), the region has received the highest number of daily extreme rainfalls of 76.2 mm or more (Carter et al., 2018). The contiguous United States has also experienced an above-average number of extreme precipitation events during the period 1986-2015 (Easterling et al., 2017).

The study area covers 11 states of the Southeast United States - Alabama, Arkansas, Florida, Georgia, Kentucky, Louisiana, Mississippi, North Carolina, South Carolina, Tennessee, and Virginia - having an area of approximately 2 million km^2. In this region, the annual precipitation received is in the range of 1000-1250 mm inland that rises to 1500 mm in the peripheral areas of the Gulf coast such as Alabama, Mississippi, and Florida Panhandle. The average precipitation over the entire country is 856 mm (Ingram et al., 2013; Kumar et al., 2021). Up to 40 years (1971-

2010) of 15-minute precipitation (herein denoted as O15) data for 575 land-based stations (Fig. 2.1) were obtained from NOAA NCEI (2014), which were quality-checked by McGehee et al. (2022). Out of these 575 stations, 388 were found to have datasets of less than 20 years and were excluded from further analysis, leaving 187 stations for this study. The historical and future projected precipitation for the period 1970-1999 (30 years) and 2030-2059 (30 years), respectively, were obtained from NA-CORDEX (Mearns et al., 2017) herein denoted as H60 and P60 respectively. NA-CORDEX contains various outputs from regional climate models (RCM) that cover North America using GCM simulation in CMIP5 archive (Mearns et al., 2017; Scinocca et al., 2016). These data have a temporal scale of 1 hour and spatial resolution of 0.44^{o}, which is approximately 50 km x 50 km. It should be noted that analysis of point measured precipitation data with areal (grid) averaged data has certain limitations (Herold et al., 2016; Trenberth et al., 2017). For instance, areal averaged show a higher frequency of lower intensities than the point measurement precipitation. However, Ganguli and Coulibaly (2019) used a similar approach of using point observed precipitation and 0.5^{o} latitute/longitude NA-CORDEX. This study focuses on improving the availability temporal scale, i.e., from 1-hr to 15-min, climate datasets at the same spatial resolution at which precipitation datasets are available.

The details of the climate models used in this study are given in Table 2.1. In the following sections, these models are denoted as CANESM, HadGEM, GFDL, MPI-RegCM, and MPI-WRF.

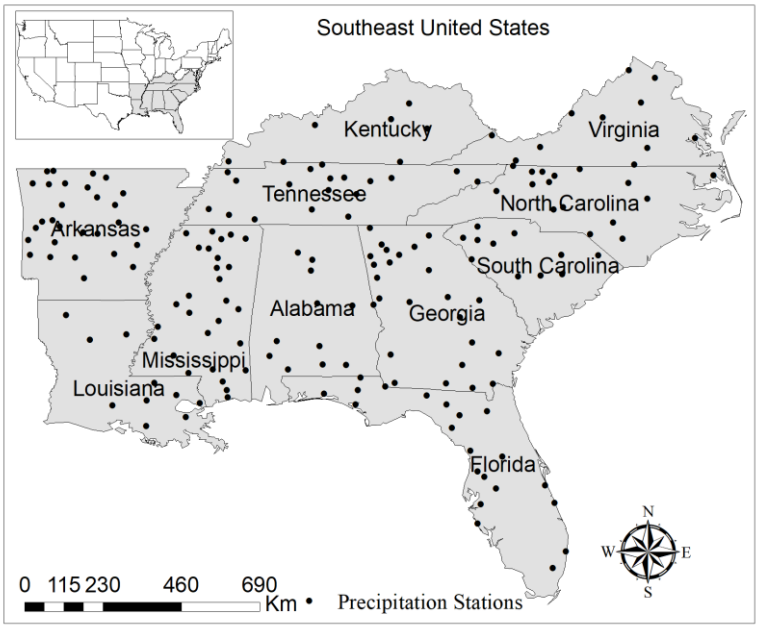

Fig. 2.1 Locations of 187 observed precipitation (O15) stations over the southeastern US.

Table 2.1 Description of climate models from NA-CORDEX.

Acronym	Regional climate model	Contributing institution	References
CANESM2_CANRCM4	Canadian Regional Climate Model version 4	Canadian Earth System Model	Scinocca et al. (2016)
HadGEM2-ES.WRF	Weather Research and Forecasting	Hadley Centre Global Environment Model version 2 Earth system model	Skamarock et al. (2005)
GFDL-ESM2M.WRF	Weather Research and Forecasting	Earth System Model – Geophysical Fluid Dynamics Laboratory	Skamarock et al. (2005)
MPI-ESM-LR. RegCM4	Regional Climate Model version 4	Max Planck Institute for Meteorology Earth System Model LR	Giorgi and Anyah (2012)
MPI-ESM-LR.WRF	Weather Research and Forecasting	Max Planck Institute for Meteorology Earth System Model LR	Skamarock et al. (2005)

2.2.2 Bias correction

The impact assessment of climate change on hydrological related studies using GCMs (especially precipitation) comes with limited representation at the regional scale (Li et al., 2010; Wood et al., 2004). This is primarily due to simplified physical laws, representation of large scale or incomplete

representation of climate system and its feedbacks (Hempel et al., 2013; Ramirez-Villegas et al., 2013). Thus, the bias correction of GCM-RCMs precipitation may be necessary for a more realistic representation of projected climate models by relating both observations and climate models rather than choosing the best guess of the climate models (Mirhosseini et al., 2013; Sharma et al., 2007). Quantile mapping has been used for bias correction of precipitation, particularly at daily or monthly scales (Gudmundsson et al., 2012; Yang et al., 2018). Whereas, at the sub-daily scale, it has been used for at least at a 3-hour scale (Mendes and Maia, 2020). One of the drawbacks for quantile mapping is the assumption of stationarity of the precipitation dataset, i.e., relationship between the historical model and observed precipitation applied to the projected simulated precipitation (Yang et al., 2018). However, according to Intergovernmental Panel on Climate Change (IPCC, 2007), the projected precipitation may not necessarily follow stationarity assumption. Therefore, the quantile delta mapping method of bias correction was used in this study which allows to incorporating the distribution associated with the projected precipitation scenarios (Cannon et al., 2015; Li et al., 2010). It is given by equation (2.1)

$$\hat{x}_{m,p.adjst\,.} = x_{m,p}\frac{F_o^{-1}\left(F_{m,p}\left(x_{m,p}\right)\right)}{F_{m,h}^{-1}\left(F_{m,p}\left(x_{m,p}\right)\right)} \qquad 2.1$$

Where F denotes the cumulative probability distribution function (CDF) of observed (0) or climate model (m) for both historical (h) and projected (p) scenarios. In addition, the frequency of low-intensity precipitation of GCM-RCMs has led to the over simulation of wet days (Herold et al., 2016; Trenberth et al., 2017). This is corrected by replacing precipitation smaller than a specific threshold value with zero in such a way that the observed wet-hour frequency matches with the historical model precipitation (Smitha et al., 2018; Teutschbein and Seibert, 2012; Velasquez et al., 2020).

The bias correction was executed on a monthly basis for each station and climate model in order to capture the intermittency of the rainfall as well as to preserve the rainfall characteristics. The advantage of using this method is that it enables the incorporation of distributions of future climate models as the observed or historical model may not always be stationary.

2.2.3 Temporal disaggregation

To disaggregate the hourly to 15-minute precipitation data, we adopted a modified stochastic storm selection approach initiated by Socolofsky et al. (2001). In this method, the O15 for a given location is grouped into precipitation events, where an event is defined as a continuous sequence of precipitation separated by at least a 1-hour interval of the dry period. These precipitation events are further grouped by months for each station. Further, the precipitation events were sorted based on accumulated precipitation depth for each monthly database. This is followed by the creation of the CDF for 15-minute precipitation depth for each precipitation event. Each point on the CDF will provide the O15 precipitation data with an associated probability.

The modified version of stochastic disaggregation of hourly precipitation starts with the selection of various precipitation events from the monthly CDFs. As described in Fig. 2.2 (for more detail, see. Mirhosseini et al. (2013)), suppose D_t is the hourly-precipitation depth. At first, the algorithm searches the monthly CDF for observed precipitation and selects an ordinate "a" for the given precipitation depth (D_t). Therefore, the probability of occurrence of precipitation depth (D_t) from the given CDF is "a". This is followed by the selection of a uniformly distributed random number between 0 and "a" which is denoted by "u_1"where it is the probability of selecting a random historical precipitation event. The corresponding observed event depth, "D_1" is obtained from the CDF. Using this precipitation depth, its distribution is extracted from the precipitation database that was created earlier.

Likewise, the subsequent precipitation depth will be given by $D_t = D_t - D_1$ as the same procedure is repeated. This process stops when $D_t < \varepsilon$, where ε is the threshold precipitation event depth. Precipitation depth below the threshold depth is randomly added.

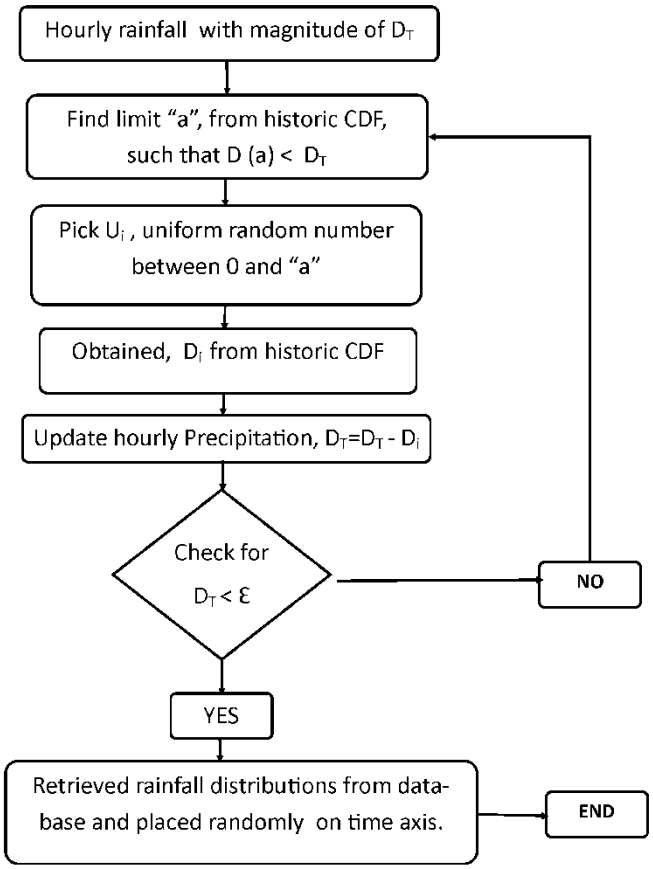

Fig. 2.2 The flowchart for the disaggregation of rainfall.

2.2.4 Evaluations of disaggregation performance

To assess the performance of the stochastic method employed, the statistical performances for both O15 and temporally downscaled 15-min precipitation herein signifies as DS15, were compared to evaluate accuracy in the replication of precipitation events. At first, the O15 data were aggregated to hourly data (denoted as O60) for each station. The aggregated precipitation data (O60) were used to test the ability to generate the DS15 data. The performance of the DS15 data

was evaluated against O15 as suggested by Socolofsky et al. (2001) Four measures are considered important in the assessment of precipitation disaggregation, viz., probability of zero precipitation, variance, lag-1 autocorrelation coefficient, and conservation of mass of precipitation on monthly basis to overcome the uncertainty associated with the start of storms in the modelled precipitation (Gutierrez-Magness and McCuen, 2004). Out of these measures, the probability of zero precipitation is considered the most important parameter since it summarizes the precipitation intermittency. As suggested by the previous studies (Choi et al., 2008; Moriasi et al., 2007; Pampaloni et al., 2021; Socolofsky et al., 2001; Willmott, 1982), the quantification of disaggregation performance used several measures for both model errors as well as model bias. Therefore, the magnitude of model error is defined by mean absolute error (MAE) and root relative square error (RRSE), which are given in equation (2.2) and equation (2.3) respectively.

$$MAE = \frac{1}{n}\sum |f_m - f_0| \tag{2.2}$$

Where, n= number of observations, f_0=observed data, and f_m=model data.

$$RRSE = \sqrt{\sum \frac{(f_0 - f_m)^2}{(f_0 - \bar{f_0})^2}} \tag{2.3}$$

Where, f_0=observed data, f_m=model data, and $\bar{f_0}$=averaged of observed data.

Whereas, the magnitude of the model bias is evaluated by developing a linear regression model between the O15 and DS15 data, the coefficient of determination, r^2,of the linear regression model can provide the degree of spread of precipitation dataset from its mean value.

The validation of disaggregation was performed by running 30 iterations for disaggregation of precipitation, as the method is stochastic and reports the average statistical measures for each location.

2.3 Data Records

The generated 15-min precipitation (DS15) data for both historical (1970-1999) and projected (2030-59) scenarios of five climate models are made available in comma-separated files (CSV). The unit of precipitation is in millimetres (mm). In addition, the details of 187 stations covering the whole southeastern, US were provided in a separate CSV file (station.csv) that includes the station number, name of station, latitude, longitude, and elevation (m). The precipitation dataset generated in this study is available through Figshare (https://doi.org/10.6084/m9.figshare.c.5671393.v1). More detail of the datasets can be found from the readme file provided at the above link.

2.4 Technical Validation

2.4.1 Bias correction

The performance of bias correction was assessed using the annual average precipitation, precipitation intensity, as well as annual wet-hour precipitation frequency for each station (Fig. 2.3- 2.4 show the result for a randomly selected station). Fig. 2.3 shows that the annual wet-hour precipitation frequency is greatly improved after bias correction with zero being the best performance (*see* Appendix A1 for all the stations). It is further observed among the models that annual wet-hour frequencies are close to zero (a good matched with the O60). We found that the main reason for the higher frequency of wet-hour precipitation in the H60 is due to the low-intensity precipitations associated with them. Also, the ratio of average annual precipitation between the H60 and O60 shows close to one (a good match with the O60). From the boxplots, it follows that there is not much difference between the bias-corrected and H60 precipitation. However, from the visual interpretation, it can be concluded that the H60, as well as bias-corrected

annual average precipitation, are close to the range of O60. We found the precipitation threshold value for each month and stations were in the range of 0.217-2.626 mm h^{-1}.

Lastly, Fig. 2.4a shows the quantile-quantile plot between the O60, H60, and bias-corrected precipitation data. It shows that bias-correction improved the H60 precipitation data for all the climate models as all the points are near to the perfect line (represented by the black line). It is further confirmed from the Taylor diagram (Fig. 2.4b) that the bias-correction satisfactorily improved the H60 precipitation for all the climate models (*see* Appendix A2-4 for all the stations). Further, the Taylor diagram shows a higher coefficient of correlation with smaller centred RMS error. All the models had a correlation coefficient of more than 95%. Whereas, the centered RMS error was less than 0.5, which is smaller than the H60. In addition, the normalized standard deviation also shows a nearly same spread of precipitation around the mean. Overall, the results for all models confirm a better performance after bias correction as all of them are near to the reference or O60 (Cannon et al., 2015; Taylor, 2001).

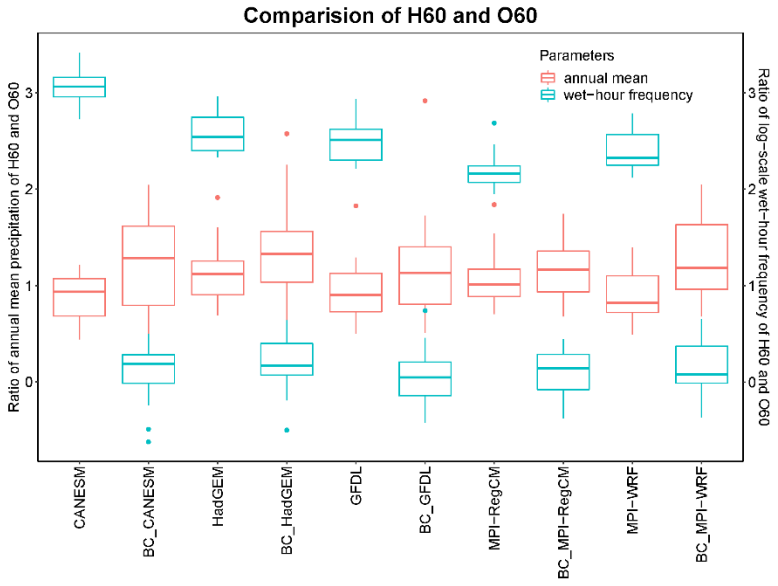

Fig. 2.3 Comparison of the H60 and O60 for NCDC station 16980300 (located at 38.96° N, 92.66° W) for annual wet-hour frequency and annual average precipitation (Note: BC-bias-corrected).

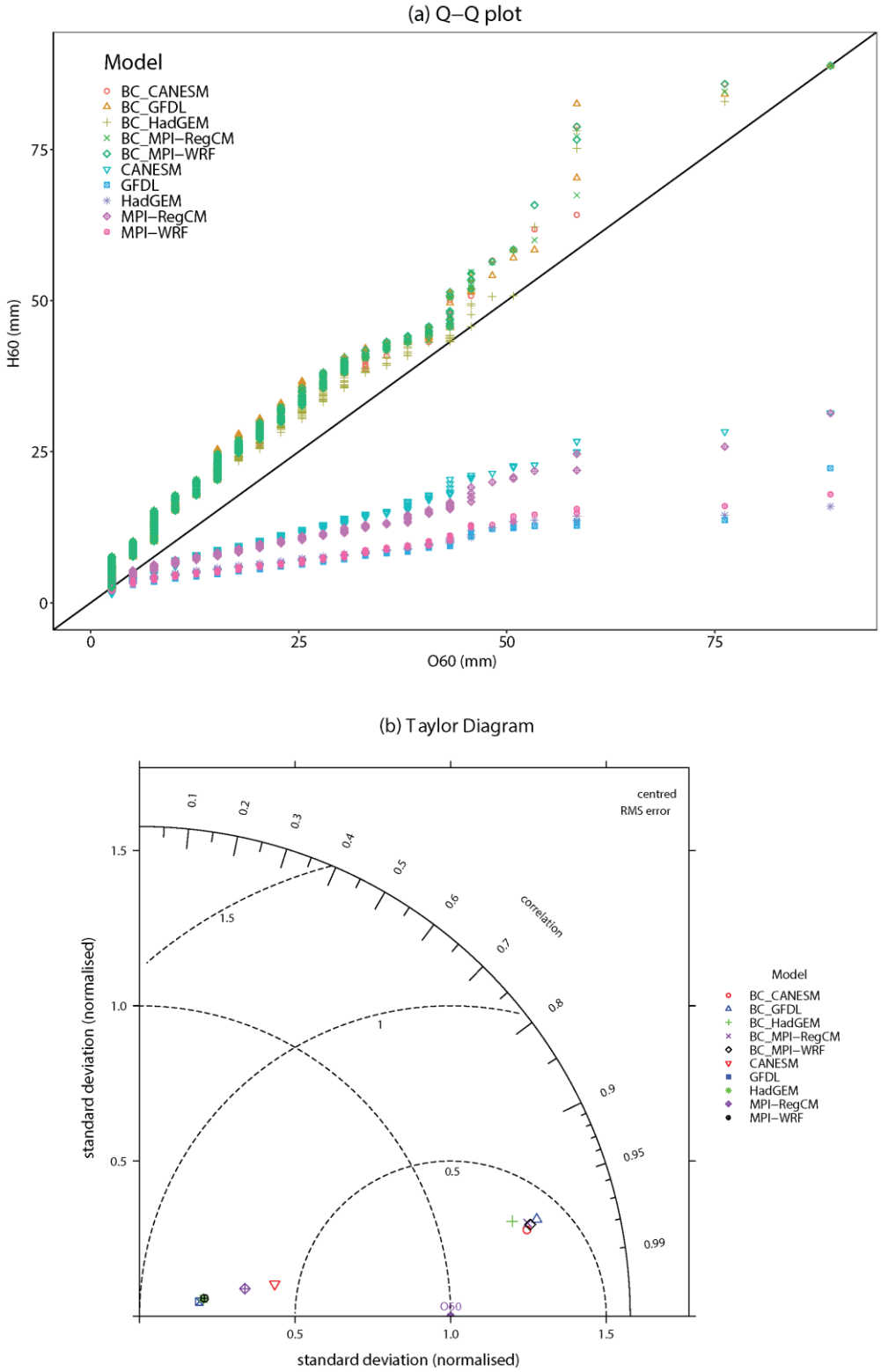

Fig. 2.4 (a) Quantile-quantile plot and (b) Taylor diagram showing the performance of the H60 and bias-corrected precipitation for hourly precipitation intensity under different climate models for the NCDC station 16980300 located at 38.96° N, 92.66° W.

2.4.2 Performance of rainfall disaggregation

The performance assessment using the statistical measures in estimating the probability of zero rainfall between the O15 and DS15 precipitation for the intermittency of rainfall are shown in Fig. 2.5-2.6 and Table 2.2. Fig. 2.5a shows the boxplot of the probability of zero rainfall for each month of all stations. The mean, as well as the distribution of all the probability of zero rainfall for DS15 precipitation, is nearly equal to that of the O15 precipitation with more than 95% coefficient of correlation. In addition, the outliers show a lower probability of zero rainfall (i.e., higher probabilities of rainfall) than the mean with minimum a value of 75% in both August and December. The large whiskers indicate that there are wide ranges of the probability of zero rainfall with a similar pattern between both the 015 and DS15. Fig. 2.5b and Fig. 2.6 show the barplot and scatterplot for the probability of zero rainfall between the O15 and DS15, respectively.

All the values of probabilities of zero rainfall (P_0) has a coefficient of determination (R^2) value of more than 0.9 with the minimum value of 0.9 in November (Table 2.2). It indicates that more than 90% of P_0 for O15 can be described by the DS15 representing closely simulated intermittency of the observed precipitation process. Furthermore, the performance of generating the probability of zero rainfall is shown by the model error indices that are estimated using mean absolute error (MAE).

It was found that MAE is less than half the standard deviation (represented by 0.5*SD), indicating a satisfactorily low-error in replicating the observed precipitation events (Moriasi et al., 2007; Singh et al., 2005). Additionally, the relative root square error (RRSE) shows a satisfactory performance of disaggregated rainfall (Choi et al., 2008).

Moreover, we anticipate that P_0 for DS15 are always less than or equal to O15. This occurs when there are precipitation events with similar magnitudes. In this case, the stochastic method randomly

choose an event leading to smaller P_0 (Choi et al., 2008; Mirhosseini et al., 2013; Socolofsky et al., 2001). For instance, let's say there is an observed precipitation event of 10.16 mm for a given duration (say 1h) that was recorded at 15-min intervals, e.g.,0,0,0,10.16. This is can be recorded as 1) 0, 0, 0, 10.16 or 2) 0, 0, 2.54, 7.62 or 3) 0, 2.54, 5.08, 2.54 or 4) 0, 0, 5.08, 5.08 or many more. In such a case, the stochastic method randomly chooses a precipitation database from the given different types of precipitation events that leads to lower both P_0 and intensities in the DS15 when it chose any event except option-1. This lower precipitation intensities of DS15 (red dashed line) than O15 (solid blue line) can also be seen from Fig. 2.10. In addition, the higher number of similar magnitudes of precipitation were because of the fact that the O15 were originally measured to the nearest inch (multiple of 0.1 in) and then converted to mm and majority of data was found with lower intensities (McGehee and Srivastava, 2018).

Overall, the process of representing the most important parameter in rainfall disaggregation (i.e., precipitation intermittency) using the probability of zero rainfall was found to be satisfactory (Choi et al., 2008; Socolofsky et al., 2001). From these results, it can be concluded that the stochastic disaggregation of precipitation closely imitates the intermittency of observed precipitation. Fig. 2.6 (P_o– February, August) also show the comparison of both O15 and DS15 value of the probability of zero rainfall for typical months of summer and winter.

Table 2.2 Statistical performance measures of rainfall disaggregation using the modified version of the stochastic method over the southeastern US.

	Probability of zero rainfall				Variance				Laa-1 autocorrelation			
	R^2	MAE	RRSE	0.5*SD	R^2	MAE	RRSE	0.5*SD	R^2	MAE	RRSE	0.5*SD
Jan	0.94	0.08	0.26	0.43	0.92	0.02	0.3	0.06	0.54	0.08	0.7	0.09
Feb	0.92	0.1	0.29	0.47	0.92	0.02	0.31	0.06	0.53	0.09	0.71	0.09
Mar	0.91	0.11	0.32	0.48	0.9	0.03	0.37	0.08	0.5	0.09	0.73	0.09
Apr	0.93	0.1	0.32	0.39	0.91	0.03	0.37	0.1	0.47	0.1	0.78	0.09
May	0.92	0.12	0.35	0.38	0.92	0.04	0.4	0.11	0.42	0.11	0.83	0.09
Jun	0.95	0.13	0.33	0.34	0.93	0.06	0.39	0.14	0.37	0.11	0.87	0.08
Jul	0.95	0.14	0.35	0.31	0.92	0.07	0.42	0.13	0.34	0.11	0.89	0.08
Aug	0.96	0.12	0.27	0.37	0.93	0.06	0.41	0.13	0.35	0.12	0.88	0.09
Sep	0.94	0.11	0.3	0.39	0.89	0.04	0.41	0.11	0.47	0.11	0.78	0.09
Oct	0.93	0.08	0.3	0.41	0.93	0.02	0.33	0.09	0.53	0.1	0.71	0.1
Nov	0.9	0.1	0.35	0.44	0.97	0.03	0.56	0.43	0.52	0.1	0.72	0.09
Dec	0.93	0.09	0.29	0.49	0.92	0.02	0.31	0.06	0.54	0.09	0.69	0.09

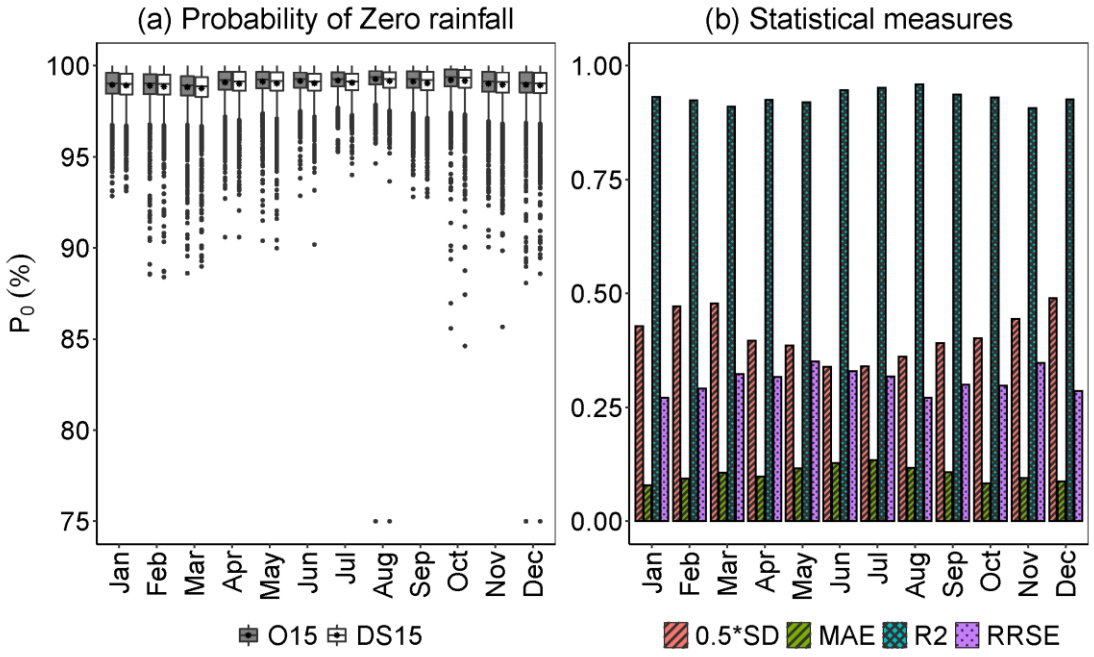

Fig. 2.5 (a) Box-and-whisker plot and (b) comparison of statistical measures in estimating the probability of zero rainfall for both O15 and DS15 for all stations.

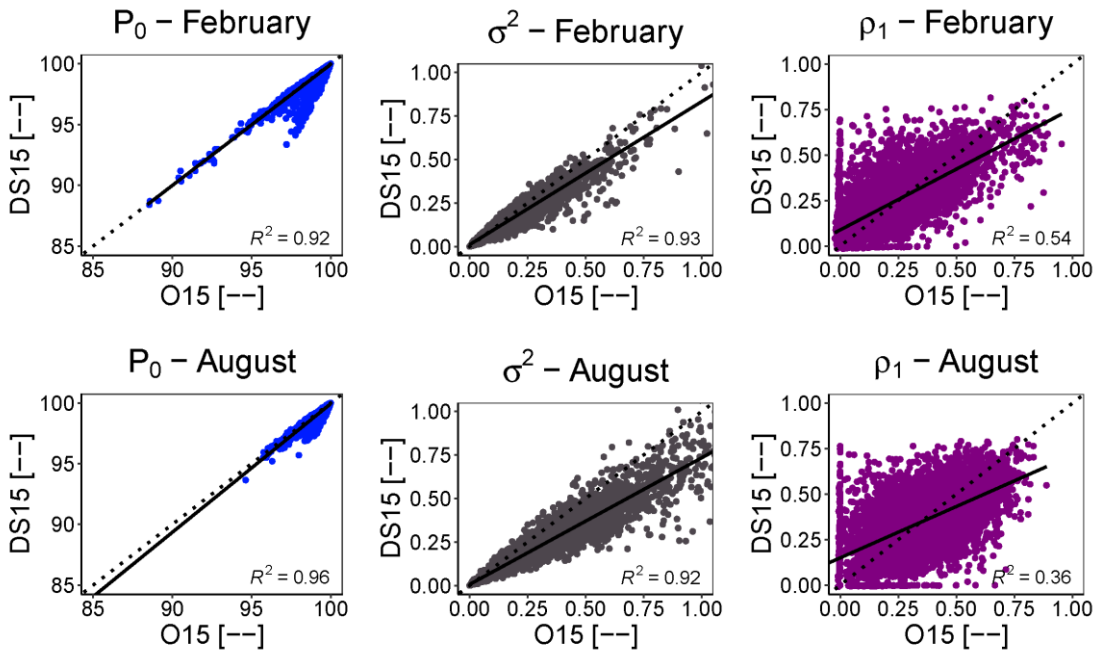

Fig. 2.6 Scatter plot of statistical measures for the estimation of the probability of zero rainfall for both O15 and DS15 in typical months of Winter (February) [top-row] and Summer (August) [bottom-row] months. The solid line represents the linear regression model.

Likewise, the comparison of the spread between O15 and DS15 about the mean is reported in Fig. 2.7 and Table 2.2. Fig. 2.7a shows the boxplot of variance of all stations for each month. It shows the mean of all variances for DS15 is nearly equal to that of O15 with a minimum value of 0.1 mm^2.However, there are outliers that nearly matched between both O15 and DS15 and that go up to 6.3 mm^2 in O15 (5 mm^2 in DS15) in June. The large whiskers also show the wide ranges of spread with a similar pattern among both O15 and DS15. Fig.2.7 and Table 2.2 show that all values of coefficient of determination are approximately 0.9 with a minimum value of 0.89 in September. Similarly, as mentioned above, the MAE values are less than half that of the respective standard deviations. Also, the model error indicated by RRSE is insignificantly different (Choi et al., 2008). The spread of variance in the scatter plots (Fig. 2.6 σ^2- February, August) for the typical months

of summer and winter show better performance for lower values and under-prediction for higher values.

In both typical months (Fig. 2.6 σ^2- February, August), the spread has low values at the beginning indicating a slight under-prediction of observed variance in both the months and this tendency seems clearer in the case of August. Such variation in both months may mainly be due to differences in seasons, which have different mechanisms of precipitation such as convective and frontal precipitation in summer and winter, respectively.

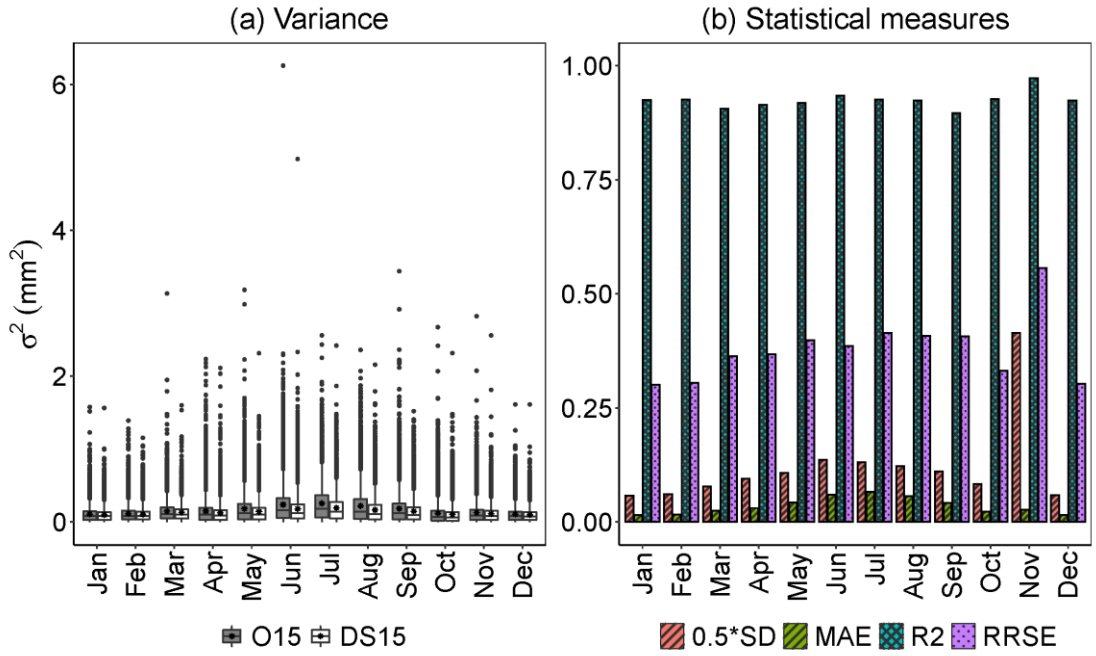

Fig. 2.7 (a) Box-and-whisker plot for both O15 and DS15 and (b) comparison of statistical measures in estimating the variance over the entire stations.

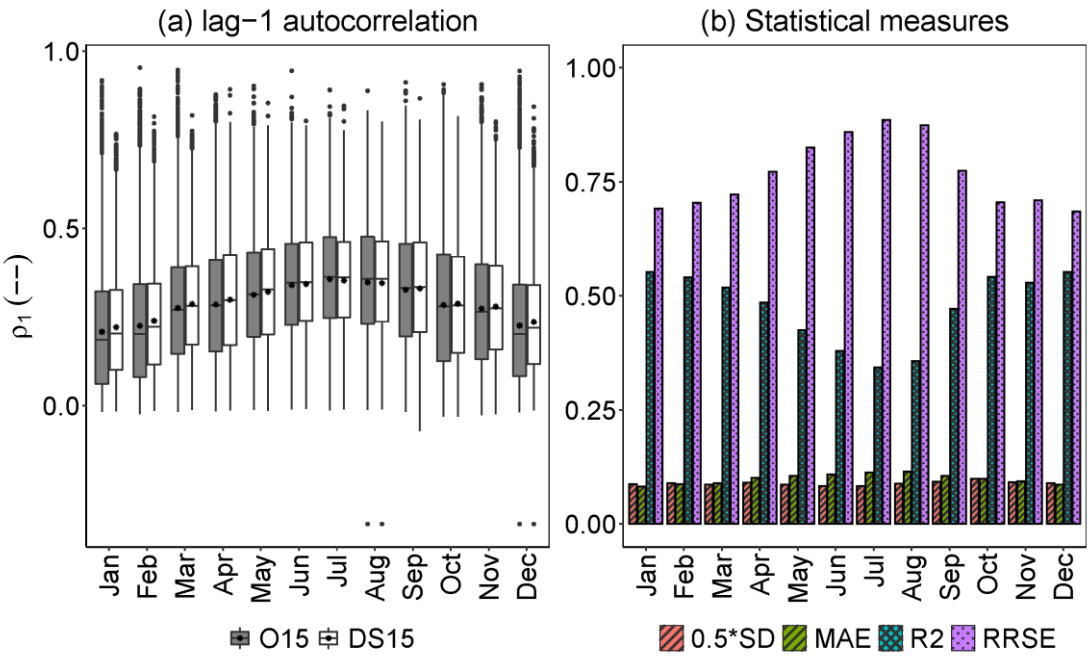

Fig. 2.8 (a) Box-and-whisker plot for both O15 and DS15 and (b) comparison of statistical measures in estimating the ρ_1 autocorrelation over the entire stations.

Lastly, the performance of lag-1 autocorrelation (ρ_1) between the DS15 and O15 are reported in Fig. 2.8 and Table 2.2. Fig. 2.8a shows the boxplot of ρ_1 for each month for all stations. In this figure also, the mean of all the ρ_1 for DS15 is nearly equal to that of O15 that ranges from 0.2 (January) to 0.35 (July). However, there are outliers with nearly matching values between both O15 and DS15 with minimum values found in both August and December. The maximum ρ_1 has value of 0.95 for O15 (0.81 in DS15) in February. Moreover, larger whiskers with similar pattem indicate a wide range of ρ_1, i.e., large scatter in both O15 and DS15.Table 2.2 and Fig. 2.8b report a low value of the coefficient of determination and high model error. Also, the scatter plot in Fig. 2.6 (ρ_1- February, August) show, for both the typical months of summer and winter. It over-predicted the O15 for lower values and vice versa. Such large scatter in ρ_1 cannot be significantly improved as it provides the best result (Choi et al., 2008).

Results were further compared with Mirhosseini et al. (2013) for the typical months of summer and winter (Table 2.3). The coefficient of determination for the probability of zero rainfall and variance in both the months outperformed those of Mirhosseini et al. (2013).In the case of model error, Mirhosseini et al. (2013) showed lower MAE values but higher values in RRSE. The relative differences in both MAE and RRSE values may have been due to the fact that both the studies used different temporal scale for rainfall, i.e., 3-hour by Mirhosseini et al. (2013) .However, in both cases, the model error is satisfactory as discussed above. Our study was expected to meet or exceed their performance since we used a 1-hour precipitation dataset as opposed to the 3-hour precipitation dataset used by Mirhosseini et al. (2013).

A limitation in this study is that it used observed dataset from the same location for each station due to the limited availability of observed precipitation. It might be wise to check for other climatologically similar dataset. Another caveat of the methodology is the assumption of the same precipitation characteristics between the historical as well as the projected period while creating the precipitation database.

Table 2.3 Comparison of statistical performance measures between DS15 with. Mirhosseini et al. (2013) . (Note: Temporal scale of precipitation in our study and Mirhosseini *et al.* are 1-hour and 3-hour respectively)

Month	**Statistic**	**MAE**		**RRSE**		p^2	
		This study	Mirhosseini et al. (2013)	This study	Mirhosseini et al. (2013)	This study	Mirhosseini et al. (2013)
February	p_o	0.1	0.01	0.29	0.31	0.92	0.91
	σ^2	0.02	0.0003	0.31	0.62	0.92	0.82
August	p_o	0.12	0.005	0.28	0.69	0.96	0.82
	σ^2	0.06	0.002	0.41	0.81	0.93	0.78

2.4.3 Validation of the stochastic disaggregation method

Here, we randomly selected a station for the validation of the stochastic disaggregation of precipitation. As mentioned earlier, validation of the disaggregation method was performed by using 30 iterations due to its stochastic nature. Fig. 2.9 shows the statistical performance of station 16980300 located at 30.25° N, 83.26° W that was randomly selected. The probability of zero rainfall and variance for DS15 is nearly equal to that of O15. In addition, values for May-July were generally under-predicted for both the variance as well as intermittency of precipitation. In the case of lag-1 correlation, there are over-predicted values in June and under-predicted values in the remaining months except in March and October. However, all of the three parameters of DS15 are within the range of ±1 standard deviation of O15 indicating satisfactory performance of the stochastic method of precipitation generation (Socolofsky et al., 2001).

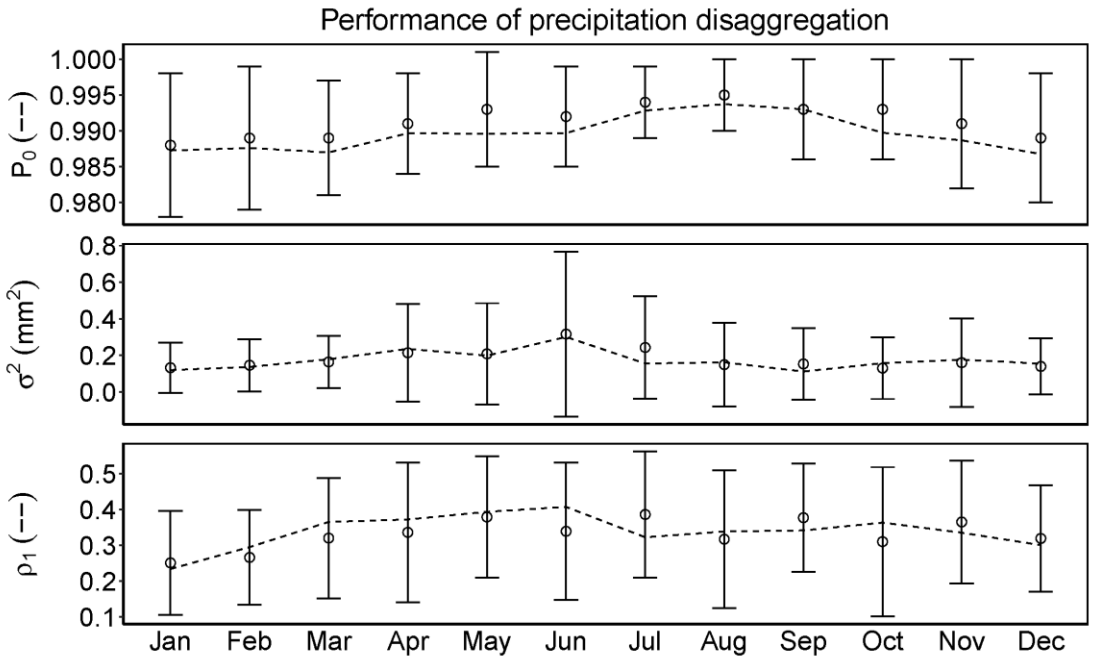

Fig. 2.9 Statistical comparison for the performance of disaggregation of precipitation for the NCDC station 44915900 located at 38.179° N, 79.58° W. The symbols and error bars denote O15 with ±1 standard deviation. The dotted line indicates DS15.

The method was further checked for generation of the precipitation intensities. Fig. 2.10 shows the precipitation intensity along with the percentage of precipitation meeting or exceeding a given value for both O15 and DS15 precipitation having a coefficient of determination approximately 0.75. This result shows that the stochastic disaggregation method was able to reproduce high as well as low intensities. Moreover, the DS15 has better intensities than the 060 dataset. However, this study's approach resulted in consistent under-prediction of moderate intensities.

The main reason was due to the stochastic selection and starting of the rainfall event. As suggested by Choi et al. (2008), the starting of the event cannot be significantly improved. Therefore, it may not be possible to make improvements given the assumptions and limitations of the disaggregation method. Moreover, the comparison among the intensities of O60 and DS15 show that there are higher intensities in the DS15. One of the main reason is that precipitation gets peaked in less than 15-minute, which results in averaging intensity for fixed-interval rainfall (e.g. 1-hour) (McGehee and Srivastava, 2018).

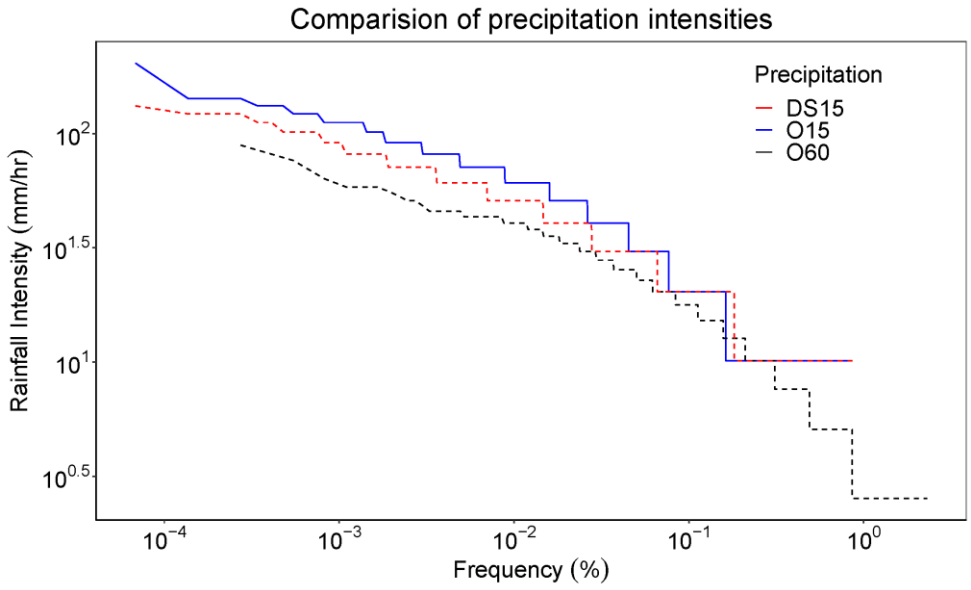

Fig. 2.10 Performance comparison of precipitation intensities under O15, O60, and the DS15 for the NCDC station 44915900 located at 38.179° N, 79.58° W.

2.4.3 Generation of projected precipitation

Subsequently, the modified version of stochastic disaggregation method was used to disaggregate P60 from bias-corrected GCM-RCM outputs. Every station used their respective CDF and was disaggregated to 15-minute precipitation for the period of 2030-2059. The quality of these data was checked, which is discussed below.

As suggested by Einfalt and Michaelides (2008), the disaggregated 15-minute precipitation data should be assessed by its quality. First, precipitation was analysed for the detection of gaps, physically impossible values, improbable zero values, unusually low values, and high values of precipitation.

Secondly, similarly to Feng et al. (2016), precipitation for all stations during the period of 2030-59 was analysed for its mean, median, SD, coefficient of skewness (C_s), coefficient of kurtosis (C_k), and coefficient of variation (CV) on the yearly and monthly basis. Fig.2.11a shows the annual average precipitation (red dots) in the range of 799-4015 mm. Table 2.4 shows the spread of precipitation around the mean, indicated by the standard deviation in the range of 331-321 mm. Coefficient of variation, i.e., the relative spread of the precipitation from its mean is in the range of 18-27 %. Moreover, three of the climate models were right-skewed (C_s >1) with mesokurtic kurtosis (C_k >1).

Similarly, Fig.2.11b shows the monthly average precipitation (red dots) ranging from 28 to 630 mm for all the climate models for the 12 months. Most of the precipitation occurred in the months of July-August. Table 2.4 also shows the spread of precipitation around the mean indicated by the standard deviation in the range of 22 to 106 mm. In terms of coefficient of variation, i.e., the relative spread of the precipitation around its mean, is in the range of 16 to 56 %. Moreover, the skewness for each month's data is different for different models. In all of the models, October and

November have more precipitation events as coefficient of kurtosis and coefficient of skewness are greater than one.

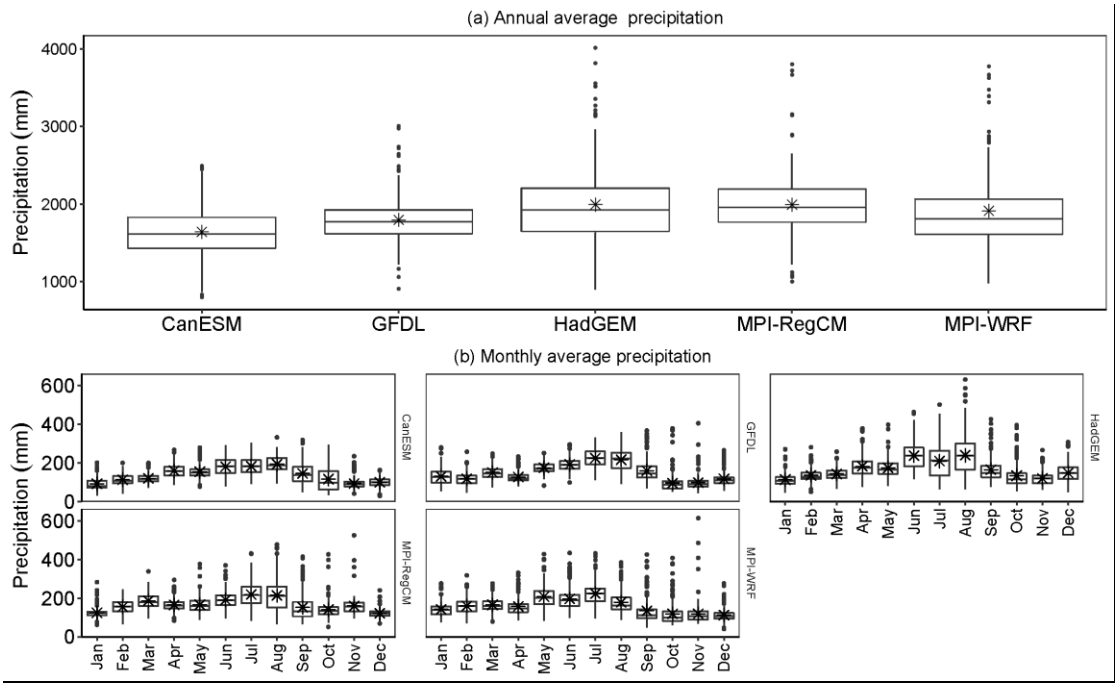

Fig. 2.11 Boxplot for (a) annual average precipitation and (b) monthly average precipitation of 15-minute data under RCP8.5 scenarios using different climate model for the period of 2030-59. Red dots represent the mean value of precipitation.

Table 2.4 Summary for DS15 using different climate models for the period of 2030-59. Units of SD and CV are in mm and %, respectively, whereas, other parameters are unit less.

Models		Annual	Jan	Feb	Mar	Apr	May	Jun	Jul	Aug	Sep	Oct	Nov	Dec
CANESM	SD	331	32	31	23	34	34	45	41	39	55	65	28	25
	CV	20	35	27	19	21	22	25	23	20	38	56	31	26
	C_s	0.3	1.1	0.3	0.9	0.2	1.1	0	0.1	0.3	0.7	0.8	1.9	-0.1
	C_k	0.2	0.6	-0.2	1	0	2	-0.6	-0.3	0	0.3	-0.5	5.5	0.4
HadGEM	SD	529	32	35	34	53	48	66	86	106	62	63	34	47
	CV	27	29	26	24	29	27	28	41	44	38	47	29	32
	C_s	1.2	1.9	1.1	0.5	1	1.4	0.6	0.5	0.8	1.7	1.9	1	0.5
	C_k	1.9	5.8	1.7	0.5	1.5	3.1	0.3	0.1	1.1	3.3	4.1	2	0.5
GFDL	SD	321	39	30	36	28	28	33	47	56	55	48	41	36
	CV	18	30	26	24	22	16	17	21	26	35	50	41	31
	C_s	0.8	0.8	0.9	0.6	1.4	0.3	0.4	-0.1	0	1.5	3.5	3.7	1.8
	C_k	2	1.2	1.9	0.1	2.3	0.2	0.6	-0.5	-0.6	2.5	15.8	20	3.9
MPI-RegCM	SD	403	27	38	39	31	41	44	64	81	68	49	46	22
	CV	20	22	24	21	18	24	23	29	38	45	35	29	18
	C_s	1.3	2.1	-0.1	0.6	0.7	1.7	0.8	0.5	0.7	1.5	3	4	1.2
	C_k	4.7	8.8	-0.3	0.7	1.9	5.6	1.6	0.4	0.6	2.1	13.1	25.6	5.3
MPI-WRF	SD	487	39	40	35	45	56	53	58	57	65	58	60	38
	CV	25	27	25	21	29	27	27	26	32	48	49	51	34
	C_s	1.4	1.1	0.7	0.6	1.5	1.1	1.3	0.7	1.3	2.2	2.4	5.1	1.4
	C_k	2.6	1.4	0.8	0.7	2.4	1.7	2.8	1.2	1.6	5	6.9	33.3	4

2.5 Usage Notes

We developed a 15-min precipitation data over the southeastern US for both historical (1970-1999) and projected (2030-2059) periods for five climate models of NA-CORDEX using a modified version of a stochastic disaggregation method. There are 187 stations that cover the whole southeastern US. We also provide station metadata such as latitude, longitude and elevation.

The dataset provides an improvement over O60 for intensity-sensitive applications such as IDF curves, rainfall erosivity, USLE and RUSLE. Precipitation intensity showed satisfactory results in the reproduction of observed precipitation of high and low intensities. However, moderate intensities were found to be generally under-predicted as the precipitation event start times were generated using uniform probability distribution and are less likely to have same start times as the observed precipitation events. The generated precipitation data can be used in most

scientific studies that deal with hydrological cycle (i.e., require precipitation). The limitation of this disaggregation method is that the generated precipitation characteristics might not sufficiently represent as same with the observed characteristics. This is an area of ongoing research, and addressing issues of precipitation characteristics in projected climate data is a major research priority.

2.6 Code Availability

Codes used in this study were done using R-Studio with R version 4.0.4. The codes are available through the GitHub link (https://github.com/bijoychandraAU/Temporal-disaggregation-of-precipitation).

CHAPTER 3

Projected Mid-Century Rainfall Erosivity Under Climate Change Over the Southeastern United States

3.1 Introduction

According to the United Nations Food and Agriculture Organization, soil erosion has been reported as one of the greatest challenges for sustainable soil management (FAO et al., 2019; Grillakis et al., 2020). Soil erosion has a severe impact on the land productivity, water bodies, and socioeconomics of a region (Almagro et al., 2017; Biasutti and Seager, 2015). During soil erosion events, nutrients and organic matter are carried away through runoff which reduces soil fertility, effective root depth, and negatively impacts water quality by increasing turbidity of surface waters (Biasutti and Seager, 2015; Segura et al., 2014). Globally, soil erosion has reduced both cropland area and crop yield at rates of 10 million ha (Grillakis et al., 2020; Pimentel, 2006) and 0.4% every year, respectively (FAO et al., 2019), resulting in an annual economic loss of $400 billion (Borrelli et al., 2017).

Among various drivers causing soil erosion (i.e., water, wind, change in land use, and cultivation practices (Borrelli et al., 2017; Naipal et al., 2018; Webb et al., 2017), water is considered the primary natural cause of soil erosion through both rainfall and runoff processes (Cerdà et al., 2009). The potential of rainfall to erode soil or rainfall erosivity is a function of both rainfall kinetic energy and maximum 30-min rainfall intensity (McGehee and Srivastava, 2018; Renard, 1997; Wischmeier and Smith, 1978, 1965, 1958). Characteristics of rainfall mostly responsible for changes in erosivity include energy, intensity, frequency, and duration (McGehee, 2016; McGehee and Srivastava, 2018). Climate change is projected to alter the rainfall characteristics due to increases in atmospheric specific humidity, warmer climate, and seasonal

rainfall (Konapala et al., 2020; Panagos et al., 2022). This will likely increase the extreme rainfall events and may act as one of the main drivers for increasing land degradation, loss of agricultural productivity, as well as soil erosion (Borrelli et al., 2021).

The effects of climate change on extreme precipitation events (greater than 50.8 mm in a day) in the United States have been observed since 1910 (Karl et al., 1996; Pruski and Nearing, 2002). The frequency of extreme precipitation events has increased more than the average number of events in the last three decades. In a similar way, the Southeast United States has also recorded historically the highest number of daily extreme rainfalls with 76.2 mm or more during the decadal periods of the 1990s, 2000s, and 2010s, with 1st, 3rd, and 2nd highest number of rainfall events, respectively (USGCRP, 2018). Extreme events have increased during these time periods of the 1990s, 2000s, and 2010 by 23%, 16%, and 20%, respectively, compared to the estimated average of 0.95 days per year in the 1900s.

According to the Intergovernmental Panel on Climate Change (IPCC, 2018), temperature at the end of 2052 is likely to increase by 1.5^{o}C from pre-industrial levels with the current rate of greenhouse gas emission. This will affect the precipitation characteristics; for instance, intensity is expected to increase up to 7% for each 1^{o}C increase in temperature (Easterling et al., 2017). Precipitation in the Southeast United States is anticipated to increase in all seasons except summer. The decrease in precipitation in summer could be as high as 15% in parts of Arkansas, Louisiana, and South Florida (Ingram et al., 2013; Keim et al., 2011). Therefore, climate change will affect future precipitation characteristics, thereby increasing the complexity of precipitation patterns of intensity, amount, duration and frequency (Almagro et al., 2017; Pruski and Nearing, 2002; Seager et al., 2009).

Rainfall erosivity of the Southeast United States may be more susceptible to climate change than other parts of the country owing to the extensive range of erosivity (2,000 to more than 10,000 MJ mm $ha^{-1}h^{-1}yr^{-1}$) and high intensities in lower latitudes (Kunkel et al., 2013; McGehee, 2016; McGehee and Srivastava, 2018; Trenberth et al., 2003). Therefore, quantifying projected changes in rainfall erosivity for the southeastern US will be key for strategic identification of regions prone to soil erosion.

The estimation of erosivity can be categorized mainly in two approaches based on the temporal scale of rainfall data i.e., i) high resolution rainfall data and ii) aggregated (hourly, daily or monthly) rainfall data (see Appendix B1 for their pros and cons) (Fischer et al., 2018; McGehee, 2016; McGehee and Srivastava, 2018; McGehee et al., 2022). Previous erosion maps, especially those of three Agricultural Handbooks (AH) i.e., AH282 (Wischmeier and Smith, 1965), AH537 (Wischmeier and Smith, 1978) and AH703 (Renard, 1997), were found to be about 30% lower than the same erosivity values from benchmarking studies (McGehee, 2016; McGehee and Srivastava, 2018; McGregor et al., 1995). Considering the discrepancies, McGehee (2016) recommended a better procedure for generating erosivity maps from 15-minute data, which was more consistent with breakpoint precipitation observations from McGregor et al. (1995) and the original erosivity work by Wischmeier and Smith (1958). The term "breakpoint" data refer to precipitation data that are measured using "breaks" in rainfall characteristics such as intensity. This should not be confused with "breakpoint format" data, which could be derived from any precipitation measurements and represented with "breaks" that do not necessarily preserve precipitation characteristics. So, breakpoint data rainfall characteristics are preserved within the level of gauge's accuracy and precision (McGehee et al., 2021). McGehee and Srivastava (2018) used non-breakpoint, 15-minute precipitation data to estimate rainfall erosivity (R-factor) in the

Southeast US for the period 1970-2013. They validated their approach using breakpoint data from McGregor et al. (1995) after making proper adjustments or corrections to account for differences between the two data types. Therefore, with proper accounting, it is possible to approximate breakpoint erosivity using 15-minute, fixed-interval precipitation data.

It is important to determine how future erosivity values may change in response to climate change. There have been numerous previous works on the estimation of rainfall erosivity around the world (Almagro et al., 2017; Ballabio et al., 2017; Beguería et al., 2018; Bonilla and Vidal, 2011; Grillakis et al., 2020; Meusburger et al., 2012; Mondal et al., 2016; Nyssen et al., 2005; Panagos et al., 2022; Riquetti et al., 2020; Shiono et al., 2013; Zhang et al., 2010). However, to our knowledge, only a few have studied projected erosivity in the United States (Biasutti and Seager, 2015; Hoomehr et al., 2016; Nearing, 2001; Panagos et al., 2022; Segura et al., 2014). Nearing (2001) used the erosivity method developed by Renard and Freimund (1994) that relies upon both monthly rainfall and annual rainfall amounts from two coupled atmospheric ocean Global Circulation Model (GCM). Biasutti and Seager (2015) used a statistical relationship between daily precipitation and rainfall erosivity. The relationship between 20 years (1981-2000) of observed precipitation and erosivity was developed and subsequently applied for future scenarios at both daily and monthly time scales. Hoomehr et al. (2016) investigated the future daily rainfall erosivity for 2010-2099 under three climate scenarios (A1F1, A1B, and B1) using monthly precipitation for the southern Appalachian region of the US. Panagos et al. (2022) used a regression model known as Gaussian Process Regression for the estimation of projected rainfall erosivity around the globe for 2041-2060 and 2061-2080. The model used a relationship between the rainfall erosivity and monthly climatic variables of average rainfall depth, maxima and minima of temperature, and 19 bioclimatic variables from WorldClim (Fick and Hijmans, 2017; Panagos et al., 2017).The prior

studies' results were based on aggregated precipitation data (e.g., daily, monthly precipitation) or statistical relationships, and therefore, they obscure the effects of rainfall intensity, especially smoothing of intensity, which are critical for erosivity calculation (Fischer et al., 2018; Flanagan et al., 2020; Hollinger et al., 2002; McGehee et al., 2022).

To-date, studies of erosivity derived from projected precipitation data have been limited by a lack of projected sub-hourly precipitation data comparable to the breakpoint precipitation data used in its original discovery (Wischmeier and Smith, 1958). Recent research has tentatively confirmed that fixed-interval data of about 5-minute resolution is roughly equivalent to breakpoint data in the few locations those data products have been compared (Flanagan et al., 2020; Hollinger et al., 2002). The equivalent fixed-interval resolution could be slightly different for other locations. The single greatest limiting factor in studies of future erosivity is the resolution of even dynamically-downscaled climate data from GCM- Regional Circulation Models (RCM), which is currently available at hourly resolutions. Takhellambam et al. (2022a) further downscaled hourly climate projection data to 15-minute resolution for several climate models at 187 locations with matching observed data over the Southeast United States. Though this data is subject to underestimation biases for erosivity (Takhellambam et al., 2022a), it is still one of the best options presently available for an analysis of future erosivity. Therefore, the objective of our study is to estimate the future (2030-59) rainfall erosivity using temporally downscaled 15-min rainfall datasets over the Southeast Unites States. Moreover, the projected future values will be compared to historical (1970-1999) values and historical values to observed values to inform the interpretation of the results.

3.2 Material and Methods

Precipitation data from observed station data and GCM-RCM historical and projected future simulations were acquired and pre-processed for subsequent erosivity calculations and comparisons. Relevant procedures for acquiring and pre-processing the original precipitation data and for calculating erosivity and erosivity density values are provided below.

3.2.1 Data and study area

The area of interest for this study includes southeastern states of Alabama, Arkansas, Florida, Georgia, Kentucky, Louisiana, Mississippi, North Carolina, South Carolina, Tennessee, and Virginia (Fig. 3.1). The region receives annual rainfall of 1000-1250 mm on average in inland areas and can receive up to 1500 mm near the coastline, which are both above the average annual rainfall for the contiguous US of 856 mm (Ingram et al., 2013; Kumar et al., 2023, 2022a, 2022b). A warming climate is likely to bring more frequent extreme climates (Allan and Soden, 2008; Easterling et al., 2017). In addition, higher frequencies of rainfall intensities, especially in the lower altitudes are observed due to disproportionate moisture convergence. Moreover, the Gulf of Mexico and the Atlantic Ocean play a key role in distinguishing this region's climate from rest of the country (Ingram et al., 2013; Kunkel et al., 2013).

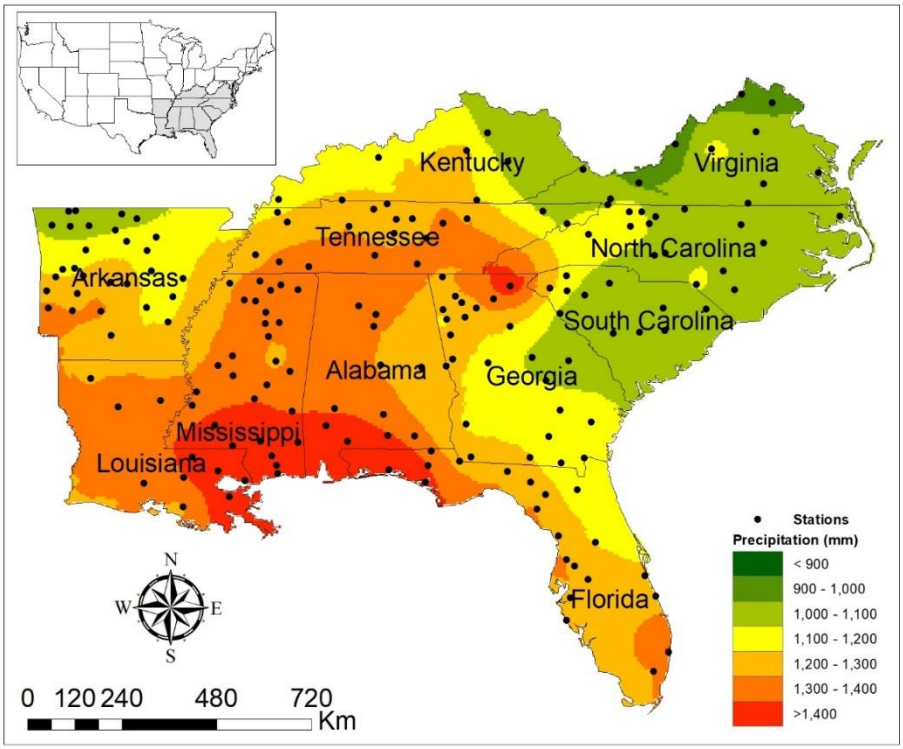

Fig. 3.1 Map showing the spatial distribution of observed (1970-2013) average annual precipitation with 187 precipitation stations over the Southeast United States.

Observed 15-minute precipitation data (DSI-3260) from 1970-2013 was obtained from the National Oceanic and Atmospheric Administration (NOAA NCEI, 2014). The data were post-processed from raw tape format by McGehee and Srivastava (2018). This data was quality checked and gap-filled by McGehee et al. (2022) who used WEPPCLIFF, which is a command-line tool to process climate inputs for soil loss models. This should not be confused with erosivity calculations which were performed for this study using the same tool and is discussed more later. The quality checked and gap-filled data from McGehee et al. (2022) was provided to Takhellambam et al. (2022a) who filtered the datasets to 187 stations (Fig. 3.1) using 20.11 screening method provided by McGehee and Srivastava (2018). The 20.11 screening method means that a given station to pass screening requires at least 20 years of measured precipitation data with at least 11 months of complete observations per year.

Historical and projected future precipitation data was acquired for five different RCM-GCMs (Table 3.1) hourly products with a spatial resolution of approximately 50 km x 50 km in the North American Coordinated Regional Climate Downscaling Experiment (NA-CORDEX). We choose these models owing to the highest available temporal resolution of 1-hour for future scenarios. Moreover, RCP8.5 represents the most pessimistic or worst-case emissions scenario which would be expected to produce the greatest changes to rainfall characteristics and erosivity (Panagos et al., 2022). If we can address this level of erosivity through various erosion control practices, we will be able to greatly reduce erosion/soil loss resulting from future climate changes. After applying quantile delta mapping (QDM) bias correction, these datasets were temporally downscaled to 15-minute by Takhellambam et al. (2022a). As recommended by McGehee and Srivastava (2018), 15-min rainfall datasets were used as a viable option to breakpoint rainfall for the estimation of rainfall erosivity (McGehee and Srivastava, 2018).

Table 3.1 Climate models used in this study.

Acronym	**GCM**	**RCM**	**References**
CANESM2_CANRCM4	Canadian Earth System Model	Canadian Regional Climate Model version 4	Scinocca et al., 2016
HadGEM2-ES.WRF	Hadley Centre Global Environment Model version 2 Earth system model	Weather Research and Forecasting	Skamarock et al. 2005
GFDL-ESM2M.WRF	Earth System Model – Geophysical Fluid Dynamics Laboratory	Weather Research and Forecasting	Skamarock et al., 2005
MPI-ESM-LR. RegCM4	Max Planck Institute for Meteorology Earth System Model LR	Regional Climate Model version 4	Giorgi and Anyah, 2012
MPI-ESM-LR.WRF	Max Planck Institute for Meteorology Earth System Model LR	Weather Research and Forecasting	Skamarock et al., 2005

NA-CORDEX coverage included all of North America for the historical and future periods of 1970-1999 and 2030-2059, respectively. GCM simulations were forced with Coupled Model

Intercomparison Project Phase 5 (CMIP5) under RCP8.5 scenario. Other scenarios (RCP2.5 and RCP4.5) were not downscaled to an hourly resolution. The original CMIP5 GCM outputs were downscaled via the NA-CORDEX to approximate temporal and spatial scales of 1-hour and 50-km, respectively (Mearns et al., 2017; Scinocca et al., 2016). It should be noted that recent studies have reported that the CMIP Phase 6 (CMIP6) is an updated climate projection based on scenarios premises of CMIP5 and used socioeconomic pathways (van Vuuren and Riahi, 2011). The projections of CMIP5 are based on the radiative forcing values of four greenhouse gas concentration pathways of 2100 (Kamruzzaman et al., 2021; O'Neal et al., 2005). Chen et al., (2020) found that overall CMIP6 performed better than CMIP5 in simulating climate extremes of precipitation, especially with very heavy precipitation days (R20mm), maximum consecutive-5-day precipitation (RX5day), and consecutive dry days (CDD). Further, the uncertainty in CDD using the interquartile range (IQR) of CMIP6 was found to be smaller than CMIP5 (Li et al., 2021). Similarly, Li et al. (2021) found the uncertainty analysis for both annual total precipitation (PRCPTOT) and annual total precipitation with daily precipitation above 95^{th} percentile (R95pTOT) of CMIP6 are found greater than that of CMIP5. In addition, Martel et al. (2022) found that CMIP6 has a narrow band of uncertainty with future climate projections, especially over North America. Overall, CMIP6 has better projection of future climate scenarios than CMIP5 (Chen et al., 2020). However, we are not considering CMIP6 in this study as CMIP6 has a coarser temporal resolution with the highest resolution of 1-hour. We used recently developed 15-min rainfall which is downscaled from CMIP5 archive of NA-CORDEX as hourly rainfall datasets smoothed the rainfall intensities, resulting in an underestimation of erosivity (McGehee, 2016; McGehee and Srivastava, 2018; Takhellambam et al., 2022a). However, future studies can use CMIP6 after the data has been appropriately downscaled.

3.2.2 Erosivity and Erosivity Density Calculations

This study utilized WEPPCLIFF version 1.6 (McGehee et al., 2020) to perform erosivity calculations based on its Agricultural Research Service (ARS) energy equation option. This option returns results for all six of the major ARS erosivity and accompanying kinetic energy calculations (Table 3.2). Options include AH282, AH537, AH703, MM (McGregor and Mutchler, 1976), BF (Brown and Foster, 1987), and R2 (USDA-ARS, 2013, 2008). R2 is shorthand for RUSLE2. Therefore, this study computed six erosivity results for all GCM-RCM products and observed stations. Only the results based on the RUSLE2 energy equation were reported in this manuscript since that is the most popular rainfall erosivity in the United States currently. Although the RUSLE2 energy equation was used to calculate erosivity (equation 3.1-3.3), not all RUSLE2 rules were applied due to concerns raised in McGehee et al. (2022, 2021) over the omission of some storms, where 'storm' is defined as a continuous sequence of precipitation, separated by 6 hours or more with less than 1.27 mm of precipitation (Wischmeier and Smith, 1978). More specifically, small storms were not omitted and storms of return period greater than 50-years were not omitted from the analysis. The prior references provide strong cases for decisions to retain all storms in various erosivity analyses if one requires more information. Similar to McGehee and Srivastava (2018), all precipitation was assumed to be rainfall in both observed and modeled climate data. Snowfall amounts in particular should not be used to calculate erosivity, and snowfall should be removed from analyses of rainfall erosivity elsewhere in the United States (McGehee et al., 2022). However, snowfall is uncommon in the vast majority of the Southeast US, and it is projected to become rarer in the future. Therefore, this assumption would have negligible effects on results of this study.

Table 3.2 The most used six rainfall kinetic energy equations. Units are in kinetic per unit volume of rain in MJ mm^{-1} ha^{-1}, and i is the rainfall intensity in mm h^{-1}.

Sl. No	Name of rainfall Kinetic energy	Energy Equation
1	Agricultural Handbook No. 282 (AH282)	$e_{AH282} = 0.119 + 0.0873\ log_{10}(i)$
2	Agricultural Handbook No. 537 (AH537) *	$e_{AH537} = 0.119 + 0.0873 log_{10}(i)$
3	Agricultural Handbook No. 703 (AH703) *	$e_{AH703} = 0.119 + 0.0873\ log_{10}(i)$
4	McGregor and Mutchler (MM)	$e_{MM} = 0.273 + 0.2168e^{(-0.048i)} - 0.4126e^{(-0.072i)}$
5	Brown and Foster (BF)	$e_{BF} = 0.29(1 - 0.72\ e^{(-0.05i)})$
6	Revised Universal Soil Loss Equation version 2 (RUSLE2 or R2)	$e_{R2} = 0.29 * (1 - 0.72\ e^{(-0.082i)})$

*Both AH537 and AH703 have kinetic energy limits imposed at 76 mm h^{-1} and AH537 has a 30-minute maximum intensity limit imposed at 64 mm h^{-1}.

$$R\ (\text{MJ mm ha}^{-1}\text{h}^{-1}\text{yr}^{-1}) = \frac{1}{n}\sum_{j=1}^{n}\left[\sum_{k=1}^{m}(E_s)_k\right] \quad 3.1$$

where R is rainfall erosivity also known as R-factor (MJ mm $ha^{-1}h^{-1}yr^{-1}$); n is number of years; m is number of storms in each year; j and k are index of number of years and storms in each year, respectively, and E_s is storm erosivity (equation 2).

$$E_s\ (\text{MJ mm ha}^{-1}\text{h}^{-1}) = \left(\sum_{t=1}^{p} e.P\right).I_{30} \quad 3.2$$

where e is the rainfall kinetic energy per unit depth (equation 1); t is single time interval; p is number of time segments in the event; P is rainfall depth (mm); and I_{30} is maximum 30-minute rainfall intensity.

$$e(\text{MJ ha}^{-1}\text{mm}^{-1}) = 0.119 + 0.0873 * \log_{10}(\text{I}) \quad 3.3$$

where, I is rainfall intensity (mm h^{-1}).

Erosivity density (ED) calculations were not supported by WEPPCLIFF at the time this study was conducted. To obtain erosivity density values, the storm data export option in WEPPCLIFF was used, and erosivity densities were calculated from the resulting storm R and precipitation values. The same procedure used by Kinnell (2010) was used for these calculations. as provided in equation 3.4.

$$\text{ED}_j\ (\text{MJ ha}^{-1}\text{h}^{-1}) = \frac{\text{R}_j}{\text{P}_j} \quad 3.4$$

where, R and P are annual rainfall erosivity and precipitation depth (mm), respectively, for j^{th} year. Erosivity density provides both erosivity pattern as well as precipitation type for erosive events. For instance, high erosivity density resulted from a high intensity rainfall event of short duration (Zhu et al., 2021). ED are typically favored in cases with shorter station record lengths, excessive data gaps, no locally measured precipitation characteristics, or more generally when the variability of erosivity presents a challenge. On the other hand, the standard approach, in which all precipitation data is used for erosivity calculation and no extrapolation relationship is necessary, may offer more insight into more subtle patterns of erosivity. This is the same approach used in the original Wischmeier and Smith (1958) discovery and underlying theory, which were established using breakpoint precipitation data. Unfortunately, some inconsistent application of that theory and other erosivity practices have resulted in published discrepancies in peer-reviewed literature (McGehee et al., 2021). This presents a challenge for studies of projected erosivity, since in addition to modeling and climate change uncertainty, there appear to be uncertainties in how to apply the original erosivity theory to various precipitation data types and their impacts on precipitation characteristics, especially intensity. Hopefully, with time, both of these sources of

uncertainty will be reduced or eliminated. Until then, it is important for readers to take note of the methods utilized to arrive at various erosivity results.

3.2.3 Extreme value analysis of rainfall and erosivity

We used the annual maxima series (AMS) method for comparing the extreme rainfall events between projected future and historical climate simulations. A generalized extreme value (GEV) probability distribution was selected as suggested by Op de Hipt et al. (2018) and Mirhosseini et al. (2013) to fit the rainfall distribution of annual daily maximum values. This distribution combines three parameter distributions i.e., Gumbel, Frechet, and Weibull which is based on the extreme value theory (Coles, 2001; Op de Hipt et al., 2018). The fitted distribution was then used to obtain the annual daily maximum rainfall for the following return periods: 2-, 5-, 10-, 25-, and 50-years. Additionally, the effects of extreme events on rainfall erosivity were analyzed using these annual maximum storm frequencies.

Moreover, the null hypothesis (H0: historical and future projected parameters come from the same distribution) was tested using either paired sample t-test, Wilcoxon sign test, or both (Op de Hipt et al., 2018). The test method was selected based on the characteristics of datasets according to the following rules. Both the paired sample t-test and the Wilcoxon sign test were used when the assumptions of normality were satisfied. Only the Wilcoxon sign test was used when the datasets were not normally distributed. The Shapiro-Wilk Test was used to determine normality for the selection of other test methods.

3.3 Results and Discussions

In this section, we report results obtained for observed (1970-2013) station data and five RCM-GCM products with both historical (1970-1999) and future (2030-2059) time periods for

precipitation, rainfall erosivity, and erosivity density. The similarity of observed and historical climate results is discussed first. Then, results based on future projections are compared to historical simulations.

3.3.1 Precipitation

The observed average annual precipitation across all stations ranged from 835 to 1689 mm yr^{-1} with a mean of 1231 mm (Fig. 3.1). The spatial distribution of observed precipitation shows that greater rainfalls are received at Gulf-Atlantic coast and the Appalachian Mountain. Moreover, bias-corrected historical model simulations (1970-1999) of average annual precipitation were generally greater than observed precipitation patterns (Fig. 3.2). Almost all statistical measures of the ensemble-average historical simulations were more than 20% different from observed measures. The values for standard deviation, coefficient of variation, and maximum average annual precipitation were most different from observed measures (Table 3.3).

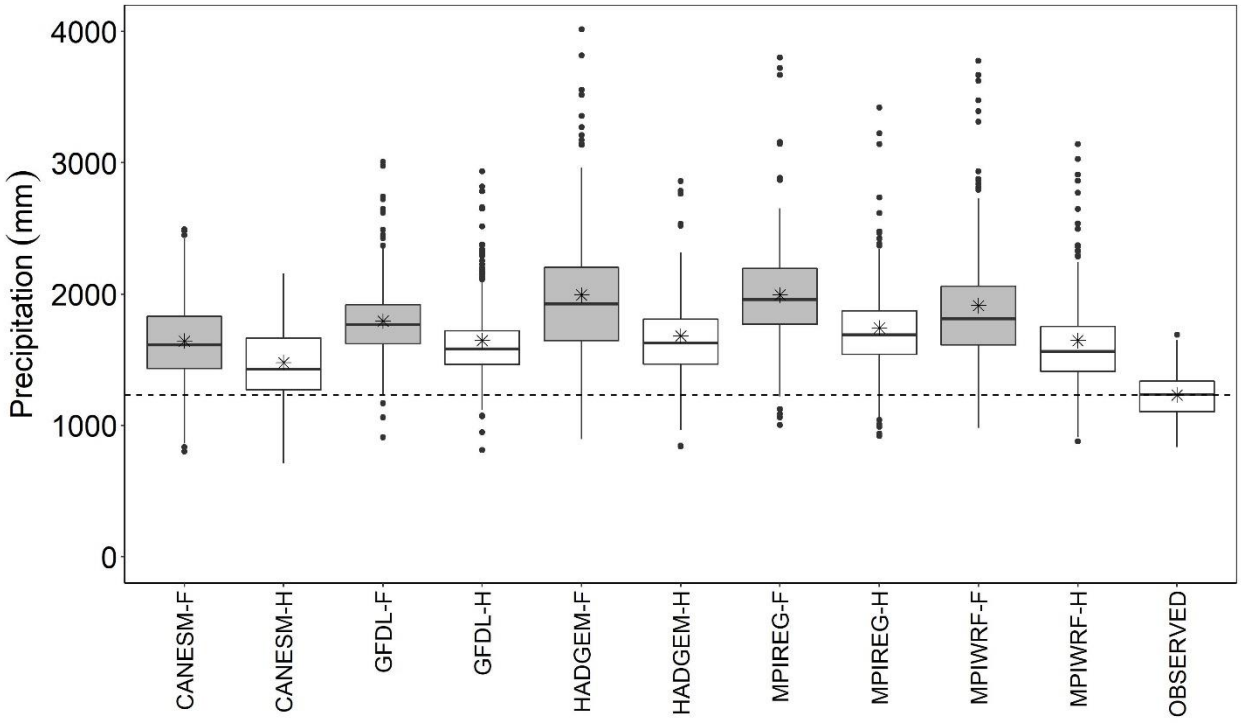

Fig. 3.2 Boxplots for observed, historical and future average annual precipitation over the Southeast US. Each point represents an average annual precipitation for a single station. 'H' and 'F' at the end of model's name indicate 'historical' and 'future' model simulations, respectively. Asterisk (*) indicates the average value. Dotted line represents the mean value of observed average annual precipitation of 187 stations from 1970-2013.

The average annual precipitation for projected future simulations was significantly greater as compared to historical simulations (Fig. 3.2). All the models reject the null hypothesis of equal average annual precipitation between the historical and future period (p-value < 0.05) favoring the alternate hypothesis at 5% significance level using the Wilcoxon Rank test. Future (2030-2059) average annual precipitation ranged from 1641-1993 mm yr^{-1}. The minimum and maximum average annual precipitation were 800 and 4015 mm yr^{-1}, respectively. Outliers (as determined by 1.5 times the interquartile ranges (IQR) in both upper and lower quartile) in average annual precipitation were present in all climate models which showed a relatively high spatial variability

of average annual precipitation for this region which tends to be less varied than in the western US. Among the five models in this study, HADGEM, MPIREG and MPIWRF resulted in greater mean, median, and variability (IQR and outliers) of average annual precipitation. The ensemble mean of projected future precipitation showed an increase in average annual precipitation of 14% as compared to the historical model ensemble mean of 1638 mm yr^{-1}. This was as little as 7% and as great as 25% when considering individual stations in the Southeast US, so according to this analysis there is a substantial amount of spatial variability in projected changes to precipitation in this region.

3.3.2 Rainfall Erosivity

The annual rainfall erosivity was calculated for 187 stations using the RUSLE2 energy equation without omitting any storms based on recommendations from McGehee and Srivastava (2018) and McGehee et al. (2022, 2021) over the Southeast United States (Table 3.4). These erosivities obtained using gauge data were further used to develop the spatial variation using kriging interpolation for ensemble model for the Southeast United States (Fig. 3.3). The erosivity patterns were found consistent from prior maps published in the agricultural handbooks, and spatial patterns were consistent in maps for observed, historical, and future periods. As expected, erosivity in the Gulf and Atlantic coastal areas and Appalachian Mountain regions was greater than in other inland regions. This shows a similar trend with the patterns of greater precipitation found in these regions (Fig. 3.1). The observed annual R-factor of 187 stations from 1970-2013 was obtained ranging from 1273 to 10587 MJ mm $ha^{-1}h^{-1}yr^{-1}$(Table 3.4 and Fig. 3.4). In addition, the observed average annual R-factor has value of 4546 MJ mm $ha^{-1}h^{-1}yr^{-1}$. As anticipated, the maximum annual R-factor was found in the eastern Louisiana which is in close proximity to the Gulf of Mexico. Whereas the minimum annual R-factor was found in the north boundary of

Virginia, where the precipitation decreases further inland from the Gulf-Atlantic coast. These observed erosivity results are consistent with previous erosivity mapping studies (McGehee and Srivastava, 2018; McGehee et al., 2022) and were consistent with the erosivity benchmarking study by McGregor et al. (1995).

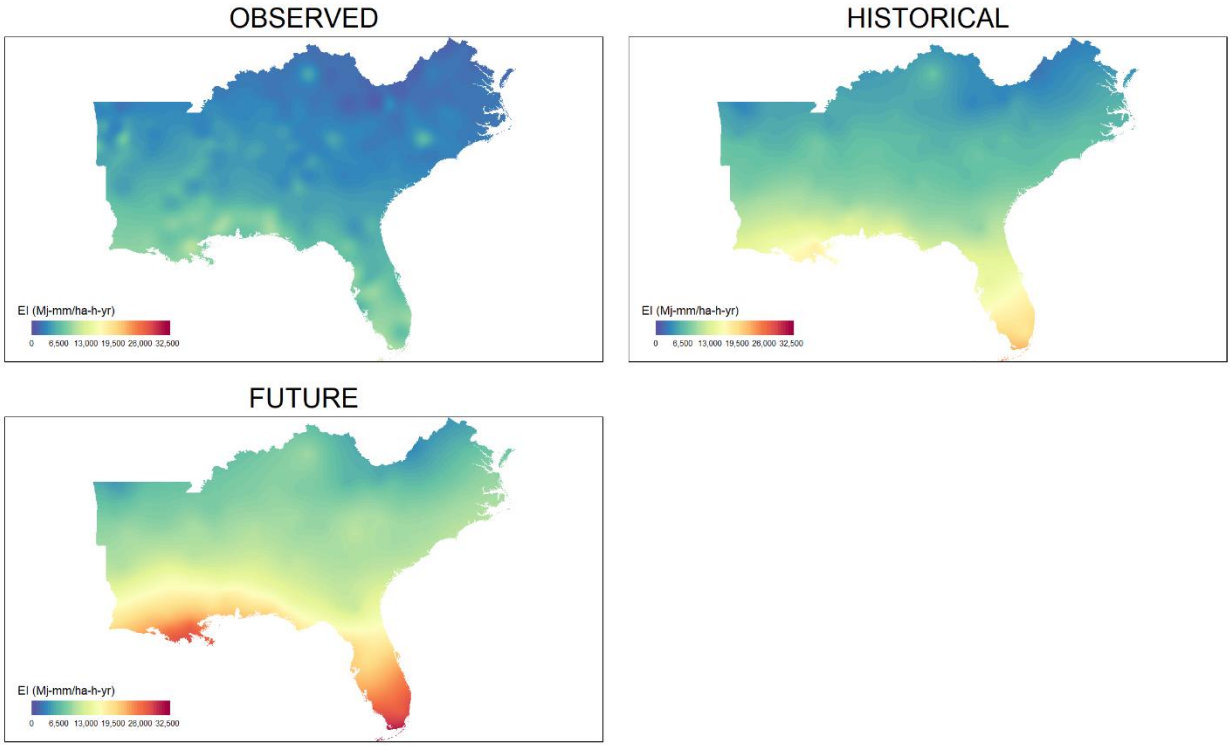

Fig. 3.3 Observed (1970-2013) and ensemble mean annual rainfall erosivity (R-factor) over the Southeast United States using the RUSLE2 energy equation (without data limitations) via WEPPCLIFF v1.6 for the historical (1970-1999) and projected future (2030-59) periods.

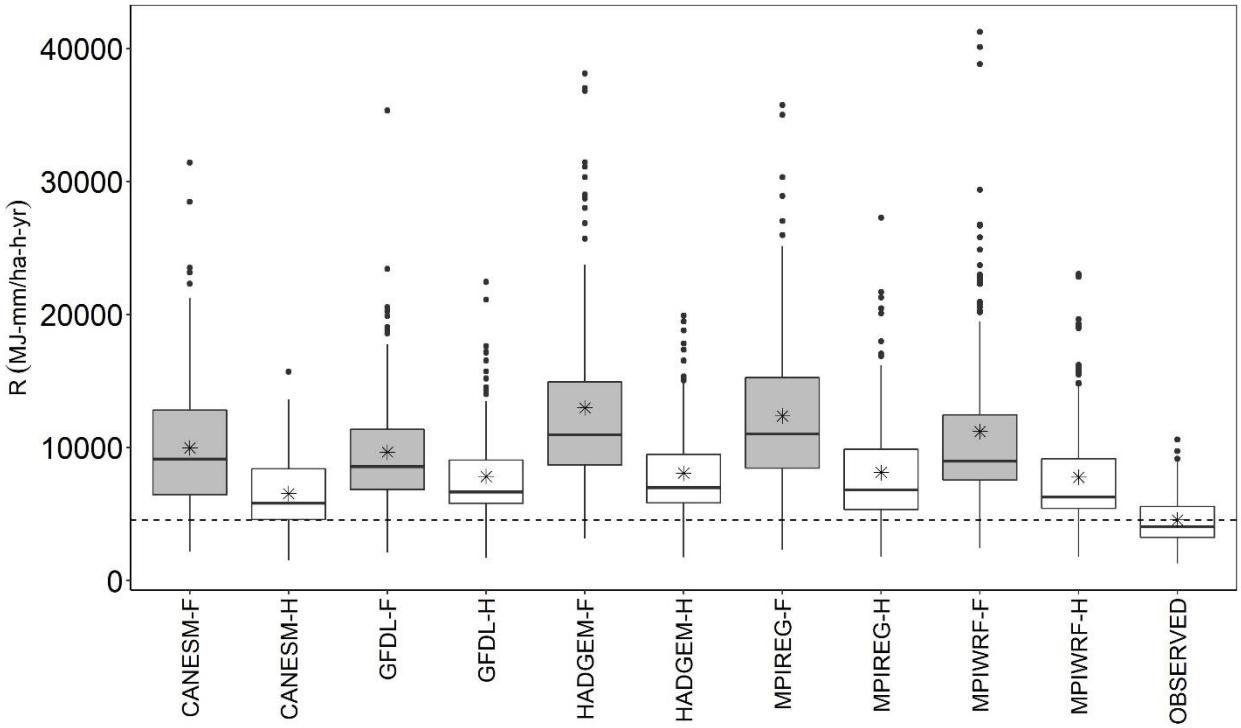

Fig. 3.4 Boxplots for observed, historical and future average annual erosivity over the Southeast United States. Asterisk (*) indicates the average value. Dotted line represents the mean value of observed average annual rainfall erosivity of 187 stations from 1970-2013.

Although, the minimum and maximum annual R-factor under five historical models from 1970-1999 were found in CANESM and MPIREG with 1501 and 27286 MJ mm $ha^{-1}h^{-1}yr^{-1}$, respectively. This range was a much greater than observed, and was as much as 158% greater for some stations. The observed data was gap-filled, but they were not corrected for gauge undermeasurement bias. This bias can range from 0% to 10% for gauges installed above ground level in various wind conditions (Rodda, 1967; Rodda and Dixon, 2012). However, this potential downward bias is small compared to the differences obtained in this analysis. Similar to that of precipitation, reasons for these differences in erosivity, are discussed later in detail.

Table 3.3 Bias-corrected average annual precipitation statistics for 187 locations in the southeastern US for observed DSI-3260 gauge data (1970-2013) and five RCM-GCM simulations of historical (1970-1999) and future (2030-2059) periods from NA-CORDEX. Both observed and simulated differences were calculated using the observed data and mean as the baseline.

Statistic	OBSERVED	CANESM-H	GFDL-H	HADGEM-H	MPIREG-H	MPIWRF-H	CANESM-F	GFDL-F
Min.	835	711	811	839	919	878	800	909
Med.	1233	1427	1583	1627	1688	1563	1611	1768
Max.	1689	2156	2933	2859	3419	3143	2492	3007
Std.Dev.	160	300	340	347	379	382	332	320
COV	0.13	0.20	0.21	0.21	0.22	0.23	0.20	0.18
Mean	1231	1478	1645	1681	1742	1646	1641	1795
Obs.Abs.Diff.	0	247	414	450	511	414	410	564
Obs.Rel.Diff.	0%	20%	34%	37%	42%	34%	33%	46%
Sim.Abs.Diff.							164	149
Sim.Rel.Diff.							11%	9%

Table 3.4 Average annual erosivity statistics for 187 locations in the southeastern US for observed DSI-3260 gauge data (1970-2013) and five RCM-GCM simulations of historical (1970-1999) and future (2030-2059) periods from NA-CORDEX using R2 approach (without data limitations). Both observed and simulated differences were calculated using the observed data and mean as the baseline.

Statistic	OBSERVED	CANESM-H	GFDL-H	HADGEM-H	MPIREG-H	MPIWRF-H	CANESM-F	GFDL-F
Min.	1273	1501	1686	1742	1807	1760	2186	2112
Med.	4043	5806	6641	6975	6814	6272	9116	8546
Max.	10587	15699	22439	19918	27286	23058	31408	35333
Std.Dev.	1860	2748	3549	3566	4165	3953	4742	4283
COV	0.41	0.42	0.45	0.44	0.51	0.51	0.48	0.44
Mean	4546	6527	7821	8075	8130	7773	9971	9655
Obs.Abs.Diff.	0	1981	3275	3528	3583	3226	5425	5108
Obs.Rel.Diff.	0%	44%	72%	78%	79%	71%	119%	112%
Sim.Abs.Diff.							3444	1834
Sim.Rel.Diff.							53%	23%

Table 3.5 Average annual erosivity density statistics for 187 locations in the southeastern US for observed DSI-3260 gauge data (1970-2013) and five RCM-GCM simulations of historical (1970-1999) and future (2030-2059) periods from NA-CORDEX. Both observed and simulated differences were calculated using the observed data and mean as the baseline.

Statistic	OBSERVED	CANESM-H	GFDL-H	HADGEM-H	MPIREG-H	MPIWRF-H	CANESM-F	GFDL-F
Min.	1.36	1.92	2.07	2.06	1.92	2.00	2.40	2.31
Med.	3.35	4.14	4.43	4.46	4.15	4.26	5.58	4.95
Max.	6.59	7.38	8.06	7.91	7.98	8.32	13.73	11.75
Std.Dev.	1.14	0.98	1.15	1.14	1.34	1.22	1.83	1.41
COV	0.32	0.23	0.25	0.25	0.30	0.27	0.31	0.27
Mean	3.60	4.25	4.58	4.63	4.45	4.52	5.83	5.21
Obs.Abs.Diff.	0.00	0.64	0.98	1.03	0.85	0.91	2.23	1.61
Obs.Rel.Diff.	0%	18%	27%	29%	24%	25%	62%	45%
Sim.Abs.Diff.							1.58	0.63
Sim.Rel.Diff.							37%	14%

In the case of future period of 2030-2059, average annual R-factor in five models ranged from 9655 (GFDL) to 12985 (HADGEM) MJ mm $ha^{-1}h^{-1}yr^{-1}$. In addition, the minimum and maximum annual R-factor were found under GFDL and MPIWRF with 2112 and 41256 MJ mm $ha^{-1}h^{-1}yr^{-1}$, respectively. These results show that the average annual future projected rainfall erosivity are significantly greater than the historical period (1970-1999) of CANESM, HADGEM, GFDL, MPIREG, and MPIWRF models (Table 3.4). Among the various climate models, HADGEM MPIREG, and MPIWRF resulted in the greatest projected average annual rainfall erosivities consistent with each of these models projecting the greatest average annual precipitations as well (Table 3.3).

Given that these simulated climate data were downscaled as part of standard NA-CORDEX procedures and further downscaled by Takhellambam et al. (2022a), we investigated whether these erosivities were being driven by a few high-intensity events. The same erosivity analysis was performed excluding events with intensities greater than 401 mm h^{-1} which may be considered as outliers (Lewis et al., 2021). Unfortunately, the resulting erosivities were not significantly different

from the previous datasets, which reduced average annual values by less than 1%. Provided the insignificant impact of these relatively extreme events, we retained all events in our various analyses. Therefore, the main reason for large differences and variation of erosivity among the different models was due to the large storm depths which may have been introduced by bias correction or downscaling.

To quantify the projected change in average annual erosivity, we computed the relative change in erosivity with reference to the respective historical model as the baseline (Table 3.4). The results show that the projected relative change in the average annual R-factor ranged from 23% to 61% or an ensemble average of 47%. Results were consistent with previous studies which also showed a similar trend in increasing projected rainfall erosivity for the region (Biasutti and Seager, 2015; Hoomehr et al., 2016; Nearing, 2001). This analysis indicated that parts of the Southeast US with the greatest precipitation may see the greatest increase in R-factor (Fig. 3.3). These areas include the most southern part of Florida, the Appalachian region, and the Gulf-Atlantic coast. However, it is unclear how much of these potential increases were influenced by suboptimal bias correction or downscaling and is discussed in detail later.

The effect of extreme rainfall events on R-factor was investigated using the annual maximum storm events from historical and future scenarios. Under all of the models, increase in the erosivity due to maximum storm events ranged from 30% to 87% (Fig. 3.5). We further found that majority of the stations have significantly increased erosivity in the future projected scenarios as compared to the historical scenario. We found range of annual maximum erosivity ranges from -10% to 393%. One of the main reasons is due to the significant increase in the extreme rainfall intensity.

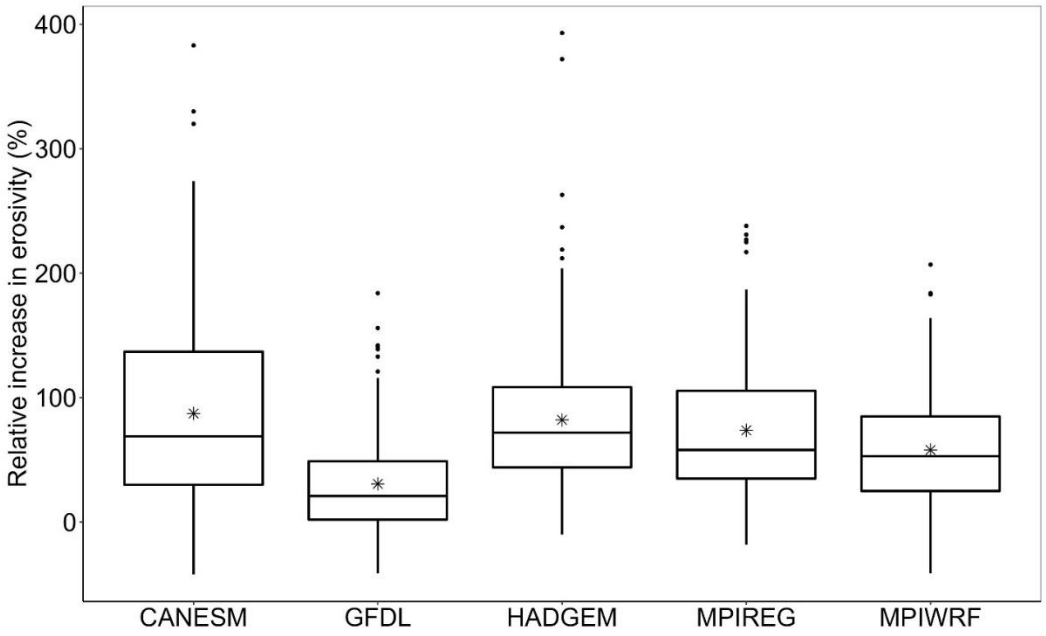

Fig. 3.5 The relative increase in the annual maximum erosivity due to the annual maximum storm event using five climate models under the RCP8.5 scenario. Asterisk symbols denote the mean value.

3.3.3 Erosivity density

Erosivity density (ED) was calculated for each station with an observed average annual value of 3.6 MJ $ha^{-1}h^{-1}yr^{-1}$ (Table 3.5 and Fig. 3.6). The historical and future ensemble mean of annual ED was 4.49 and 5.76 MJ $ha^{-1}h^{-1}yr^{-1}$, respectively (Table 3.5). In relative terms, ED based on historical simulations was 25% greater than observed ED, but this was smaller than differences for both precipitation and erosivity which were 33% and 69%, respectively. The results from both paired sample test and Wilcoxon rank test found rejecting the null hypothesis of equal erosivity density between the historical and future scenarios at a 5% significance level with p-value < 0.05. Therefore, projected ED was 29% significantly greater than historically simulated ED, which means that simulated changes due to climate were greater than differences between historical simulations and observed data.

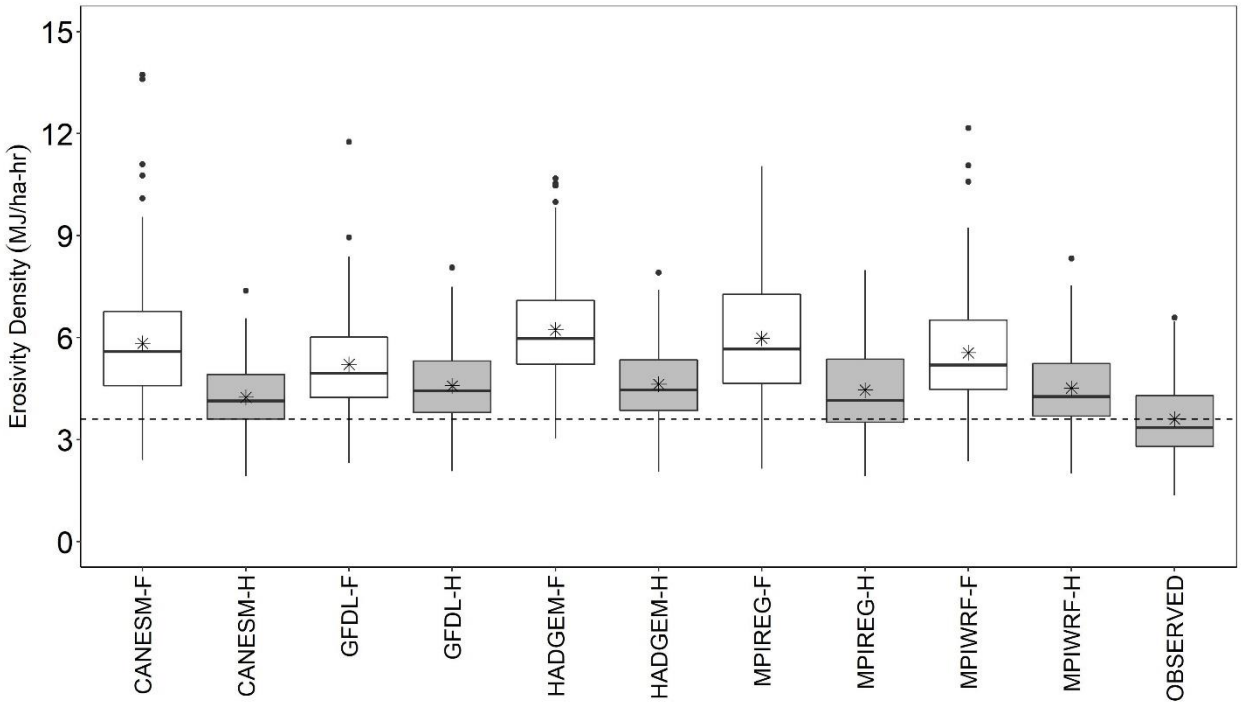

Fig. 3.6 Boxplots for observed, historical and future average annual erosivity density over the Southeast United States. Asterisk (*) indicates the mean value. Dotted line represents the mean value of observed average annual rainfall density of 187 stations from 1970-2013.

Similar to precipitation and erosivity analyses presented earlier, ED results could have been impacted by bias correction of downscaling methods. It is possible that impacts on the wettest stations' precipitation and resulting erosivity calculations could result in biased ED calculations due to the nonlinear behavior of erosivity. Therefore, although ED accounts for differences in precipitation amount, it would not account for a potential nonlinear bias in wetter parts of the Southeast. These issues and the actions taken to account for them are discussed below.

3.3.4 Comparison of rainfall erosivity map among different studies

The comparison of estimated future erosivity with previous studies is challenging. This is due to the different erosivity estimation methods and frameworks employed by various studies. In

addition, the different time scales and uncertainty associated with different GCMs and downscaling methods further contributed to the differences in erosivity estimations (Panagos et al., 2022). The climate models are associated with different variations depending upon the type of model, e.g., initial and boundary conditions of the rainfall generation mechanism (Mirhosseini et al., 2013). However, we were able to compare the findings of a previous study by Panagos et al. (2022) which projected erosivity for 20 years (2041-2060) using 30-min rainfall, estimated with HADGEM and MPIREG models under RCP8.5 scenario over the Southeast United States. We estimated the annual R-factor using 30-min (aggregated 15-min to 30-min rainfall) rainfall data with HADGEM and MPIREG model under the RCP8.5 scenario for the 20 years (2040-2059) to compare with Panagos et al. (2022).

Using the HADGEM model (Fig. 3.7a), Panagos et al. (2022) reported that the annual R-factor from 2041-2060 varies from 1501 to 11249 MJ mm $ha^{-1}h^{-1}yr^{-1}$ with an average value of 7137 MJ mm $ha^{-1}h^{-1}yr^{-1}$. In our study, the average annual R-factor showed 11190 MJ mm $ha^{-1}h^{-1}yr^{-1}$ which is found greater by 56%. The change in annual R-factor based on our approach as compared to the Panagos et al. (20022) ranged from -67% to 1167% (Fig. 3.7b). Similarly, the MPIREG model showed a consistent result with relatively greater annual R-factor in the Gulf-Atlantic coastal regions as compared to the Panagos et al. (2022) (Fig. 3.7c and 3.7d). Under the MPIREG model, the reported range of annual R-factor by Panagos et al. (2022) was 1240 to 10851 MJ mm $ha^{-1}h^{-1}yr^{-1}$ with an average value of 6705 MJ mm $ha^{-1}h^{-1}yr^{-1}$ (Fig. 3.7b). Our study showed an average annual R-factor of 11917 MJ mm $ha^{-1}h^{-1}yr^{-1}$. In addition, the relative change in annual R-factor under MPIREG model in our study shows in the range of -50% to 1234% as compared to that of Panagos et al. (2022).

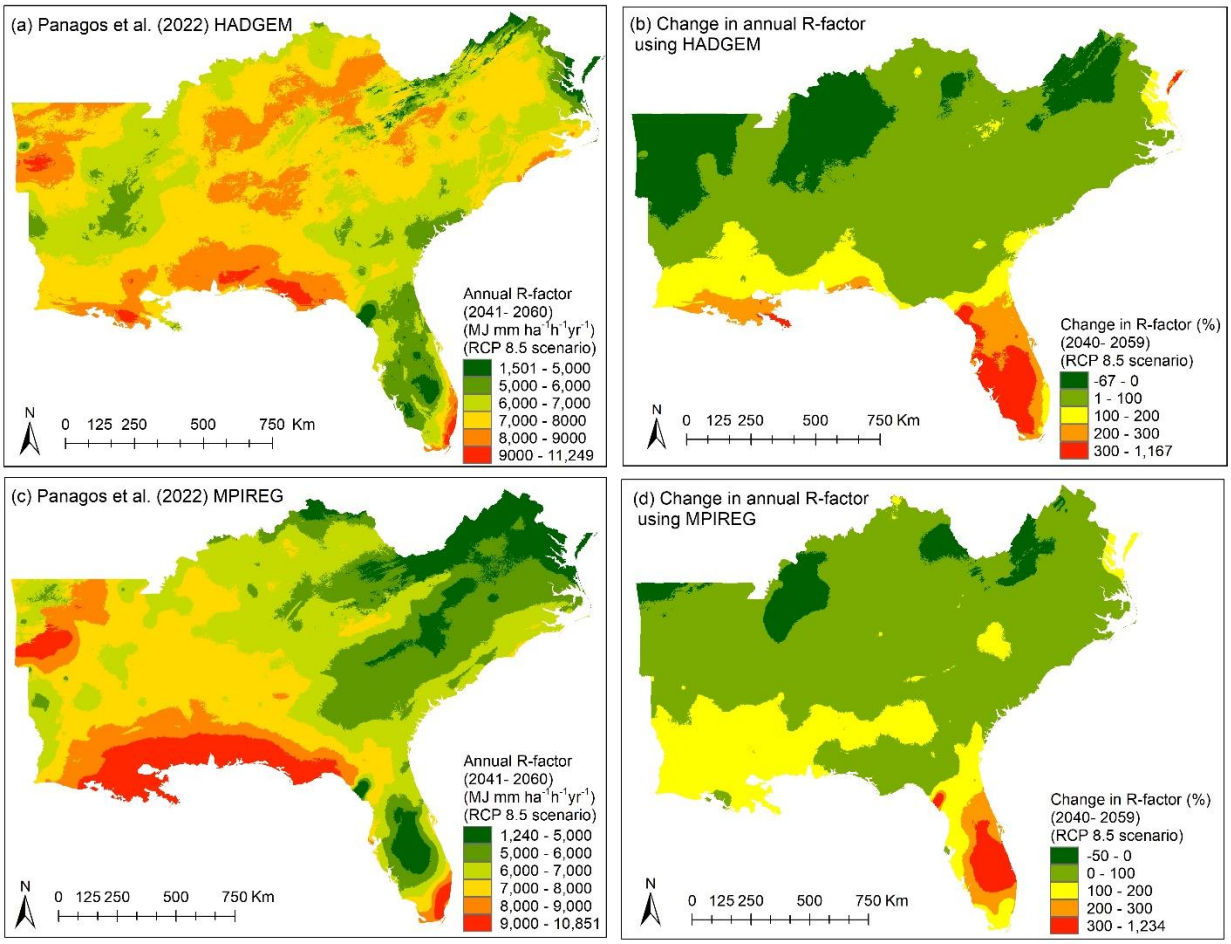

Fig. 3.7 (a) and (c) Reported annual R-factor of Panagos et al. (2022) for HADGEM and MPIREG model under RCP8.5 scenario for 20 years (2041-2060) using Gaussian Process Regression. (b) and (d) relative change in annual R-factor (in percentage) in our study as compared to Panagos et al. (2022) under same HADGEM and MPIREG model for 20 years (2040-2059). Negative and positive value indicates the lower and greater annual R-factor in our study with reference to the Panagos et al. (2022), respectively.

The negative and positive values (Fig. 3.7b and 3.7d) indicate a lower and greater values of annual R-factor in our study with reference to Panagos et al. (2022), respectively. In both models, the lowest and greatest change in annual R-factor was found in the northern and southern parts of the region, especially in the Gulf-Atlantic coastal region. However, the majority of the area showed

relatively smaller change (up to 100%) with 0% indicating no change in the annual R-factor (light green color in Fig. 3.7b and 3.7d).

3.4 Discussion

3.4.1 Future erosivity using high-temporal resolution rainfall datasets

The accurate estimation of rainfall erosivity requires high temporal resolution of rainfall datasets (Kim et al., 2020; McGehee and Srivastava, 2018; McGehee et al., 2022; Panagos et al., 2017). McGehee and Srivastava (2018) and McGregor et al. (1995) further encouraged to use "breakpoint" rainfall datasets for the estimation of erosivity. Therefore, our study used recently developed 15-min rainfall data from CMIP5 archive for future (2030-2059) erosivity estimation over the Southeast United States as a viable option to breakpoint datasets (McGehee and Srivastava, 2018; Takhellambam et al., 2022a). The differences in observed and historical simulated rainfall data could have arisen from slightly different time periods, model or downscaling limitations (e.g., course resolution, incomplete model science, model stochasticity), bias correction, observed data limitations (e.g., gaps or undermeasurement bias), or a combination of these. The impacts of these differences on this study are discussed later at Section 4.2 in detail. Although, the significant different between the historical and future rainfall datasets confirmed that by 2059, the region is expected to receive a significant number of intense rainfalls compared to the historical period of 1970-1999. This necessitates updating the estimation of future rainfall erosivity with high temporal resolution rainfall datasets (McGehee and Srivastava, 2018; Takhellambam et al., 2022a).

Previous studies used aggregated rainfall due to the unavailability of rainfall datasets (Biasutti and Seager, 2015; Hoomehr et al., 2016; Nearing, 2001; Panagos et al., 2022). These rainfall datasets of lower temporal resolution lose the information of true rainfall characteristics. Takhellambam et

al. (2022a) showed that the downscaled 15-min rainfall datasets exhibit intensities that are greater than the 1-hourly scale but lower intensities than the observed 15-min rainfall. The rainfall intensity using aggregated rainfall datasets has often been underpredicted as compared to the 15-min datasets due to the smoothening of the intensities and eventually lower erosivity (McGehee and Srivastava, 2018; McGehee et al., 2022; Op de Hipt et al., 2018). For example, the annual erosivity from Kim et al. (2020) was found to be under-predicted as compared to our study. This was expected because Kim et al. (2020) used 1-hour grided rainfall to estimate erosivity. Kim et al. (2020) reported a maximum value of 6000 MJ mm $ha^{-1}h^{-1}yr^{-1}$ with a mean value of less than 2500 MJ mm $ha^{-1}h^{-1}yr^{-1}$. Whereas, our study showed greater erosivity as compared to Kim et al. (2020) because we use 15-min rainfall datasets that give improved estimates of intensities as compared to the hourly rainfall. Hollinger et al. (2002), McGehee and Srivastava (2018), and USDA-ARS (2008) have suggested that we further increase erosivity obtained from the 15-min rainfall datasets by 4% to compensate for the dampening in intensity with the use of fixed-interval data (e.g., 15-min) as compared to breakpoint data.

The future erosivity showed a large variation among the stations which can be seen from the boxplot (Fig. 3.4) and large standard deviation values in Table 3.4. These variations are owed to the large variation of rainfall due to the extreme rainfall intensities (Fig. 3.2). Furthermore, this can be confirmed by the higher ED (>3 MJ $ha^{-1}h^{-1}$) indicating that the precipitation has higher intensities for short-duration rainfall events (Chen et al., 2022; Panagos et al., 2015).

Each RCM-GCM shows different amounts of rainfall due to the different mechanisms of rainfall generation. Therefore, the ensemble model of five RCM-GCMs allows a representative estimation of future rainfall erosivity under the RCP8.5 scenario. This prevents the result from being influenced by a single model (Panagos et al., 2022). Moreover, kriging interpolation has

enabled us to evaluate the spatial variation of erosivity using the rain-gauge approach (Kim et al., 2020; McGehee and Srivastava, 2018). The greater amount of annual R-factor in the Gulf-Atlantic coast owes to the greater precipitation because of warm air rising through sea breeze circulation. Precipitation decreases further inland and with increasing elevation and reduced moisture holding capacity of cooler air (Ingram et al., 2013). Greater precipitation was observed in the Appalachian Mountains due to orographic effects leading to greater erosivity in the region (Ingram et al., 2013). A comparison of the findings of this study with those of Panagos et. al (2022) shows relatively similar trends of erosivity in majority parts of the region. However, there is a greater estimation of erosivity in this study, especially in the Gulf-Atlantic coastal region and southern Florida. We anticipated a greater amount of erosivity as the region receives a greater amount of rainfall owing to the convective precipitation and tropical cyclones (Ingram et al., 2013; Knight and Davis, 2007). Panagos et al. (2022) used two stations in southern Florida to estimate erosivity, whereas our study used denser rain-gauge data of 16 (Fig. 3.1), which could have resulted in erosivity differences. In addition, the greater amount of annual erosivity in our study, especially in the Gulf-Coastal area could be due to various reasons. For instance, Panagos et al. (2022) estimated the annual R-factor using a regression model, whereas our study estimated the same based on rainfall storm events. The true rainfall characteristics, such as intensity are lost while using the statistical relationships for the estimation of erosivity (Flanagan et al., 2020; Hollinger et al., 2002; McGehee et al., 2022). Our study also used in-situ rainfall datasets which are superior to the grid-based datasets of Panagos et al. (2022), especially with high-intensity rainfall events (Kim et al., 2020). In addition, differences in amounts of annual erosivity among the models is also caused due to different mechanisms of rainfall generation employed within each model (Mirhosseini et al., 2013).

Regardless of the models and erosivity application methods used, the region is expected to have significantly higher future annual erosivity than in the historical period. Furthermore, the region's elevated rainfall erosivity is caused by increased rainfall intensity (Swain and Hayhoe, 2015). However, there are some uncertainties associated with our study, which are discussed in detail below.

3.4.2 Bias Correction and Downscaling Implications

Bias correction (BC) and downscaling (DS) were both potential sources of differences between observed and historical model simulation results. BC led to increasing average annual precipitation and intensities. While downscaling led to a decrease in moderate rainfall intensities. However, the downscaled results showed higher intensities than the hourly although lower than the observed 15-min precipitation (Takhellambam et al., 2022a). In this study, we used relatively high-temporal resolution, 15-minute historical, and projected precipitation datasets generated from hourly NA-CORDEX products by Takhellambam et al. (2022a). That study used quantile delta mapping (QDM) and a modified stochastic disaggregation method for bias correction and further downscaling of NA-CORDEX climate products, respectively. There were substantial differences between historical simulations and observations of precipitation, erosivity, and erosivity density (Table 3.3-3.5 and Fig. 3. 2, 3.4, and 3.6). In comparison to the observed annual R-factor, the bias-corrected and non-bias-corrected annual R-factors had overestimated and underestimated values by 137% and -63%, respectively. It is currently unclear if there are other BC and DS methods that would result in better agreement with observed data especially with hourly scale since, to our knowledge, this has not been studied and published in the peer-reviewed literature for erosivity-based analyses.

The goal of this study was to quantify projected mid-century changes in erosivity for the Southeast US and to do this using an erosivity approach of RUSLE2 with recommendations of McGehee and Srivastava (2018) and McGehee et al. (2022, 2020) rather than an oversimplified erosivity extrapolation or aggregation method that assumes a relationship to historical precipitation characteristics. This approach to analyzing projected future erosivity is more rigorous than others, but there are potential sources of uncertainty in the estimated future rainfall erosivity, especially with the BC and DS.

To assess the performance of bias correction, Takhellambam et al. (2022a) evaluated average annual precipitation, wet-hour frequencies, and precipitation intensities. Although the intensities and wet-hour frequencies were improved, the average annual precipitation was largely over-corrected or overpredicted. As expected, the uncorrected historical model simulations of average annual precipitation were greater than observed due to potential under-measurement biases in the observed data generated by adhesion, evaporation, wind drift, and splashing (Table 3.6) (Fischer et al., 2018) and model biases in the simulated data. However, bias correction of the simulated results worsened average annual precipitation differences which increased by 3.5% to 19.2% over what was already consistently greater than observed. This, along with the increased presence of more extreme event depths and characteristics, was largely responsible for the greater mean and maximum average annual erosivity values obtained in this study. The results showed that the extreme event depths significantly increased as the null hypothesis was rejected at the 5% significant level. The mean relative increase (in percentage) of annual daily maximum rainfall with reference to the historical model ranges from 8% to 46% (Table 3.7).

Table 3.6 Percentage change in average annual precipitation after bias correction of climate models used in Takhellambam et al. (2022a). Here, Raw and BC denotes the ratio of average annual precipitation of historical model and observed precipitation before and after bias correction.

Model	Raw	BC	Change (%)
CANESM	1.09	1.26	15.56
HADGEM	1.39	1.44	3.50
GFDL	1.32	1.41	6.82
MPIREG	1.34	1.50	11.74
MPIWRF	1.19	1.42	19.23

Table 3.7 Mean relative change (%) in future projected annual daily maximum rainfall as compared to the historical model with return period of 2-, 5-, 10-,25-, and 50- years.

Model	2-years	5- years	10- years	25- years	50- years
CANESM	17	32	38	43	45
GFDL	8	12	13	15	15
HADGEM	22	35	39	44	46
MPIREG	21	27	29	31	32
MPIWRF	19	24	26	28	30

While the additional downscaling method used by Takhellambam et al. (2022a) was another potential source of uncertainty in this analysis, it was unlikely that this method resulted in upward biases in this study's analyses. We base this assessment on the results presented by Takhellambam et al. (2022a) showing that there was a substantial downward bias in 15-minute intensities obtained from their DS method as compared to those from observed data. More specifically, the intensities were greater than those of simulated hourly data but less than those of observed 15-minute data. According to Flanagan et al. (2020), this would result in a substantial underestimation (at least 9%) of erosivities that would be obtained from breakpoint precipitation gauges at the same location. We found the temporal downscaling using a modified stochastic approach has led to the underestimation of erosivity with an average value of 17%. This is because the downscaled rainfall characteristics do not adequately represent the observed rainfall characteristics (Takhellambam et

al., 2022a). Overall, these findings highlight the uncertainties of using climate models for high-resolution applications and their limitations in representing rainfall characteristics. In light of potential bias correction limitations, it may be of interest to evaluate downscaled, uncorrected climate simulations for analyses involving erosivity. The newest generation of climate model simulations, which are being conducted at increasingly finer spatial and temporal resolutions, may meaningfully reduce uncertainties from BC and DS methods in subsequent analyses.

3.5 Conclusions

The most significant finding of this study is that precipitation, erosivity, and erosivity density in the Southeast US are projected to increase by 14%, 47%, and 29%, respectively, for 2030-2059 over the historical baseline (1970-1999). These results were obtained using an ensemble of five different climate models in NA-CORDEX which is an archive of CMIP5 under the RCP8.5 scenario. CMIP6 has better future climate projection with a narrower uncertainty band as compared to CMIP5. However, the temporal resolution of CMIP6 is 1 hour, which makes it unsuitable for the estimation of erosivity until it is downscaled to 15-min resolution. Therefore, in this study, we have used a recent 15-min precipitation dataset that was downscaled using the CMIP5 dataset.

We used WEPPCLIFF version 1.6 and the RUSLE2 energy equation without data limitations for the estimation of rainfall erosivity and erosivity density. The future ensemble model showed an average annual R-factor of 11237 ± 1299 MJ mm $ha^{-1}h^{-1}yr^{-1}$. The southern part of Florida, the Appalachian region, and the coastal region of the Gulf of Mexico were areas in the Southeast predicted to experience the greatest absolute increase in erosivity while areas with lower baseline erosivities were generally predicted to see the largest relative changes.

Erosivity and erosivity density outcomes in this study were determined as opposed to aggregation or extrapolation methods which have become more common of late. This was an important decision of this study which can potentially reduce uncertainties associated with assuming historical precipitation characteristics for future periods. However, as discussed earlier, this decision also may have resulted in greater exposure to bias correction and downscaling method limitations. For instance, downscaling alone was determined to suppress erosivity estimates by 17% in an analysis using this study's observed data. The bias correction of rainfall overestimated the annual R-factor with an average of 137%, whereas non-bias corrected data underestimated the R-factor with an average of 62% when compared to the observed annual R-factor. Average annual precipitation, erosivity, and erosivity densities obtained from bias-corrected and downscaled historical model simulations were consistently greater than observed values. Some degree of this should be expected on account of under-measurement biases associated with the observed data; however, the differences obtained in this study were much greater than can be attributed to that dynamic alone. Therefore, alternative bias correction and downscaling methods should be evaluated for potential use with subsequent erosivity analyses which may result in better agreement between historical simulations and observed metrics.

Results of a similar study with different bias correction and/or downscaling methods could result in very different outcomes, especially since erosivity increases with total rainfall depth, rainfall intensity, or frequency of wet days. In addition, future research needs to be conducted with different biases and downscaling methods. Despite these uncertainties, this study affirms that projected climate change is likely to increase erosion in the Southeast US and that this increase will not be driven by changes in precipitation amounts alone but also due to changes in intensity and energy.

CHAPTER 4

Artificial Neural Network-Empowered Projected Future Rainfall Intensity Duration Frequency Curves under Changing Climate

4.1 Introduction

Extreme rainfall events pose a serious threat to the ecosystem and economy by amplifying both the magnitude and frequency of floods (Nerantzaki and Papalexiou, 2022). Therefore, rainfall Intensity-Duration-Frequency (IDF) curves are used when planning and designing hydrologic and hydraulic structures (Mirhosseini et al., 2014; Yan et al., 2018). However, the existing structures for rainfall and floods designed are based on the stationarity of the IDF curves which give a probability of rainfall intensity in a given period, particularly National Oceanic and Atmospheric Administration Atlas 14 (Perica et al., 2013; Soltani et al., 2020; Sun et al., 2019; Zhao et al., 2022a). In addition, the IDF curves are used in the design of erosion control structures, storm, and sewer drainage designs, and bridges (Amatya et al., 2021).

According to the IPCC (2018), by 2052 the temperature is expected to rise by 1.5 ℃ from the Pre-industrial Period with the current emission rate of greenhouse gases, which eventually will affect future extreme rainfall events (Takhellambam et al., 2023). The increase in temperature has resulted in higher water-holding capacity in the atmosphere, i.e., a 7% increase in water-holding capacity per degree Celsius of temperature (Easterling et al., 2017; Trenberth, 2011). The plausible effects include a change in rainfall amount, frequency, and intensities or probable maximum rainfalls (Cheng and AghaKouchak, 2014). Under these conditions, extreme rainfall events are expected to occur more frequently and with greater intensity in most parts of the world, with urban areas being the most vulnerable (Ghasemi Tousi et al., 2021). Therefore, to adapt or reduce the vulnerability of new water management structures, future rainfall characteristics under the

changing climate should be considered while developing IDF curves (Mirhosseini et al., 2014; Noor et al., 2022). For instance, the most critical component of cities' structures includes storm-water drainage and flood mitigation measured which are based on the IDF curves (Crévolin et al., 2023; Ghasemi Tousi et al., 2021). Many studies reported that there might be an underestimation of extreme events considering stationary assumption as changing climate has increased rainfall characteristics (Cheng and AghaKouchak, 2014; Sarhadi and Soulis, 2017; Vu and Mishra, 2019). Previous studies developed future projected IDF curves using aggregated (e.g., hourly or daily scale) and non-stationary nature of rainfall characteristics under changing climate (Cheng and AghaKouchak, 2014; Ganguli and Coulibaly, 2019; Ghasemi Tousi et al., 2021; Mirhosseini et al., 2014, 2013; Sarhadi and Soulis, 2017; Zhu, 2013; Zhu et al., 2012). Cheng and AghaKouchak (2014) reported an underestimation of extreme rainfall of up to 60% under the stationarity assumption compared to nonstationary conditions while using five locations in the United States. Sarhadi and Soulis (2017) developed IDF curves for different durations that range from 1 to 24 h under different return period of 2 to 100-year. The extreme events were found underestimated when considering the stationary nature of rainfalls. Vu and Mishra (2019) incorporate the time-dependent covariate for developing IDF curves for a duration ranging from 1 to 5 days and confirmed approximately 90% of the total extreme events of 378 followed non-stationary conditions. Ganguli and Coulibaly (2019) developed IDF curves under a nonstationary model over eight locations in the densely populated and major financial region of Southern Ontario, Canada. The study has confirmed a significant increase in extreme rainfall intensities for future scenarios (2030-2070) as compared to that of the baseline period of 1970-2010. Ghasemi Tousi et al. (2021) updated the IDF curves for the city of Tucson, Arizona from 2020 to 2051 using eight global climate models. The findings showed a significant increase in future extreme rainfall events which

eventually needed to update IDF curves. An example of stormwater culvert design demonstrated how differences in model output could double the design size and significantly increase the cost. Moreover, Noor et al. (2022) proposed IDF curves along with uncertainty for ungauged locations across Peninsular Malaysia. Shorter duration rainfall with a higher return period was found to increase greater than that of longer duration with a smaller return period.

Similarly, Mirhosseini et al. (2013) assessed future projected IDF curves using 15-min rainfall data in Alabama, United States. The 15-min rainfall was developed with 3-hour rainfall data using a modified stochastic method of Socolofsky et al. (2001). This 15-min rainfall dataset was further used to develop IDF curves using GEV distribution. The results demonstrated that less severe rainfall was anticipated for short-duration occurrences. However, the simulated rainfall intensities were under-predicted compared to the observed data. Mirhosseini et al. (2014) reported consistent results of underpredicted intensities. This was further improved by Mirhosseini et al. (2014) by introducing a feedforward ANN approach. Thus, IDF curves were further updated for future projected climate scenarios for Alabama using GEV distribution and compared with a stochastically generated rainfall of Mirhosseini et al. (2013). The ANN method reported superior performances compared to the stochastic models in developing maximum rainfall depths. Further, rainfall events with less than a 2-hour duration showed decreased intensities, and longer-duration storms with higher uncertainties (Mirhosseini et al., 2014).

Further, Zhao et al. (2021) improved the ANN approach for rainfall disaggregation of Mirhosseini et al. (2014) through a computationally efficient and more accurate approach that was applied over two cities in southern Vietnam. The advantages include computationally efficient training data that used only extreme rainfall data points instead of the whole series and improving accuracy through

the inclusion of previously simulated steps of rainfall. However, the Zhao et al. (2021) method provided a limited assessment of the hourly and multi-hourly scales.

In this study, we aimed to further extend the approach of Zhao et al. (2021) for disaggregating hourly to sub-hourly (15-, 30-, and 45-min) monthly maximum rainfall datasets. This is because sub-hourly rainfall aggregates offer greater intensities than hourly rainfall aggregates (Takhellambam et al., 2022a). McGehee and Srivastava (2018) reported that maximum rainfall intensity occurred within 15 minutes of a storm. So, aggregated datasets are underestimated due to the averaging of sub-hourly data. In addition, McGehee and Srivastava (2018) and (Takhellambam et al., 2022b, 2022a, 2023) reported that the Southeast region of the United States has the greatest potential for change in rainfall characteristics under the changing climate. This necessitates updating the future IDF curves required for adequate hydrologic and hydraulic infrastructure designs, such as dams and culverts under the changing climate. We hypothesize that a feed forward and back propagation ANN model would perform better than the stochastic model in disaggregating hourly to sub-hourly (15-, 30-, and 45-min) monthly maximum rainfall datasets. Therefore, the objectives of this study were to: (1) generate sub-hourly (15-, 30-, and 45-min) monthly maximum rainfall datasets under the RCP8.5 scenario using the feed forward and back propagation ANN model, and (2) develop the projected future rainfall IDF curves using the GEV distribution for the Southeast United States using improved sub-hourly rainfalls.

4.2 Material and Methods

4.2.1 Study Area and Data

The average annual rainfall received in the Southeast United States (Fig. 4.1) is greater than the country's average of 856 mm. The annual rainfall ranges from 1000 to 1250 mm and can go as high as 1500 mm (Ingram et al., 2013; Kumar et al., 2022a, 2021; Takhellambam et al., 2023).

The higher intensity rainfall is received on the Gulf-Atlantic coast and decreases inland. At the same time, the Appalachian Mountain region sees a greater rainfall intensity due to the orographic effect (Takhellambam et al., 2022a). The major factor for the distinctive climate in the region is due to the presence of both the Gulf of Mexico and the Atlantic Ocean (Ingram et al., 2013; Kunkel et al., 2013).

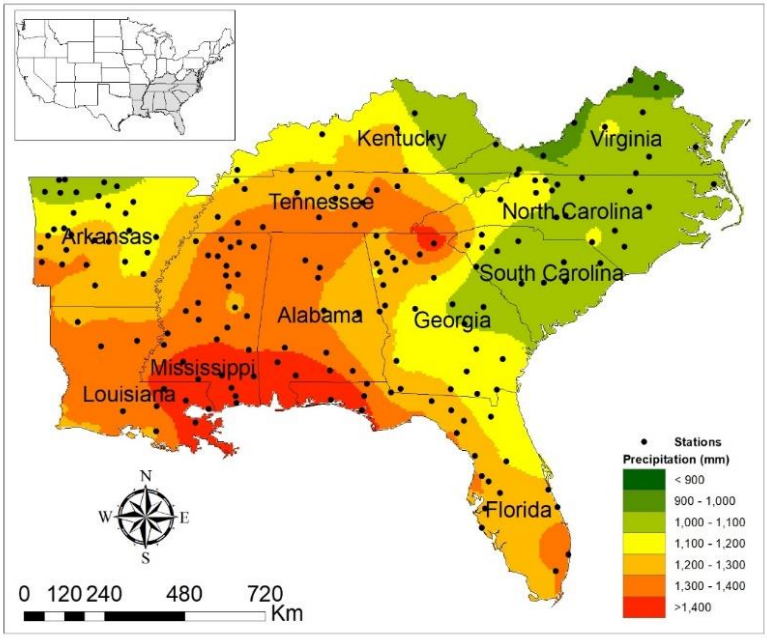

Fig. 4. 1 Study area and location of observed 187 rainfall stations over the Southeast United States.

We obtained 44 years (1970-2013) of observed 15-min rainfall for 528 gauge data from the National Oceanic and Atmospheric Administration, DSI-3260, archived at the National Climatic Data Center (NOAA NCEI, 2014). (McGehee et al., 2022; Takhellambam et al., 2022a, 2022b) recommended using the 20.11 screening method to check the quality of rainfall datasets and eventually found 187 stations that passed the screening method. Passing the 20.11 screening method requires a station to have a minimum of 20 years of complete observed precipitation for 11 or more months per year (Takhellambam et al., 2023). For the future projected 15-min rainfall

data for the period 2030-59, we used five climate models for the future projected period (2030-59) of 15-min rainfall obtained from the North American Coordinated Regional Climate Downscaling Experiment (NA-CORDEX) under the RCP8.5 scenario. The five models included CANESM2_CANRCM4, HadGEM2-ES.WRF, GFDL-ESM2M.WRF, MPI-ESM-LR. RegCM4, and MPI-ESM-LR.WRF (Giorgi and Anyah, 2012; Scinocca et al., 2016; Skamarock et al., 2005; Takhellambam et al., 2022a). Hereinafter, we will refer to the climate model data as CANESM, HADGEM, GFDL, MPIREG, and MPIWRF, respectively. The Regional Climate Model-Global Climate Model (RCM-GCM) used GCM simulation of Coupled Model Intercomparison Project Phase 5 (CMIP5) archive. In addition, both temporal and spatial scales of these models are 1 hour and 0.44°, respectively (Mearns et al., 2017; Scinocca et al., 2016).

4.2.2 Bias correction

The use of climate model data in hydrological-related studies has suffered from errors due to the simplified or limited representation at the regional scale (Takhellambam et al., 2022a). For instance, there are lower rainfall intensities with a large number of wet days which do not represent the observed rainfall intensities. To solve this problem, we used the quantile delta mapping (Cannon et al., 2015) method as suggested by Takhellambam et al. (2022a). The bias correction was carried out on a monthly scale to acquire intermittency of the rainfall while also preserving the rainfall characteristics.

$$\hat{x}_{m,p.adjst.} = x_{m,p} \frac{F_o^{-1}\left(F_{m,p}(x_{m,p})\right)}{F_{m,h}^{-1}\left(F_{m,p}(x_{m,p})\right)} \quad 4.1$$

where x is the rainfall data, and F represents the cumulative probability distribution function for either the observed (o) or model-based (m) historical (h) and future projected (p) scenarios.

4.2.3 Disaggregation of hourly rainfall to sub-hourly monthly maximum rainfall using ANN

The ANN model of Zhao et al. (2021), which was originally developed for disaggregating daily to sub-daily monthly maximum rainfall, was tested in this study for disaggregating hourly to sub-hourly (i.e., 15-, 30-, and 45-min) monthly maximum rainfall. This ANN model is a multi-layered perceptron neural network, where the output layer gives the sub-hourly monthly maximum rainfall based on the hourly information from the input layer. The model has three layers of input, hidden, and output layers. We use rectified linear unit as an activation function due to its simplicity. Furthermore, we selected 20 neurons with a dropout rate of 0.5 which avoid overfitting during training in the hidden layers based on trial and error. The loss function and optimizer were mean squared error and RMSprop, respectively.

We briefly introduce the ANN model below and refer the readers to Zhao et al. (2021) for more details. To estimate the extreme rainfall amount at finer resolutions (sub-hour), the input layer of the ANN model sends input variables of the monthly maximum hourly rainfalls (assume at time t) and both preceding (t-1) and succeeding (t+1) hourly rainfall to the hidden layer (Fig. 4.2). Optimum input variables were selected based on minimum Akaike Information Criterion. Moreover, the hidden layer having nonlinear transformation generates the output variable of sub-hourly monthly maximum rainfall. Further, the ANN model used 70% and 30% of datasets during training and testing, respectively. Overall, we estimated (3 resolutions X 187) 561 models in our study area owing to the different rainfall generation mechanisms at different locations. For instance, the rainfall generation mechanisms in the Gulf-Atlantic coast and Appalachian Mountain are mainly due to the convective and orographic effects respectively.

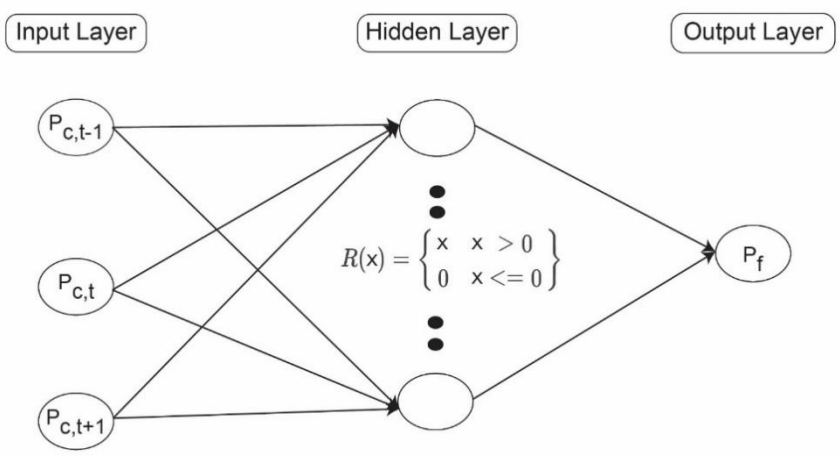

Fig. 4.2 An overview of the disaggregation of hourly (c) to sub-hourly (f) monthly maximum rainfall datasets using activation function (R(x)). Here, P is the monthly maximum rainfall at a given time step (t). The preceding and subsequent hourly rainfall datasets are represented by t-1 and t+1, respectively.

4.2.4 Performance comparison in generating monthly maximum rainfall intensities

The assessment of the ANN's performance in disaggregating hourly to sub-hourly monthly maximum rainfall was conducted using the gauge observed rainfall data. We aggregated the observed 15-min rainfall into 1-h intervals. This rainfall data is then disaggregated to monthly maximum rainfall of 15-min using the feed-forward back-propagation ANN model. Similarly, we disaggregated the remaining temporal scales of 30- and 45-min rainfall datasets.

We compared the ANN-disaggregated monthly maximum 15-, 30-, and 45-min rainfall data with those of stochastically generated rainfall data by Takhellambam et al. (2022a). Since the stochastic data were available in continuous time series of rainfall at 15-min intervals, we also aggregated the 15-min scale to the scales of 30- and 45-min. Further, we extracted the monthly maximum rainfall from each of the 15-, 30-, and 45-min rainfall datasets. Thus, the performance of the

monthly maximum rainfall of each scale using both the ANN and stochastically generated datasets was compared as discussed below.

More specifically, the statistical measures of NSE and Pearson correlation coefficient were used to assess the performance of rainfall disaggregation (Mirhosseini et al., 2014; Takhellambam, 2016). These measures were computed for each station using the observed and disaggregated monthly maximum rainfall for the entire time series. These performance measures are defined below, starting with the NSE given by

$$NSE = 1 - \frac{\sum_{i=1}^{n}(o_i - m_i)^2}{\sum_{i=1}^{n}(o_i - \overline{o}_i)^2} \quad 4.2$$

where, o = observed rainfall, $\overline{o}$ =average observed rainfall, m = model rainfall, and n = number of observations.

The Pearson correlation coefficient, in this setting, is defined as

$$r = \frac{\sum_{i=1}^{n}(o_i - \overline{o}_i)(m_i - \overline{m}_i)}{\sqrt{[\sum_{i=1}^{n}(o_i - \overline{o}_i)^2]}\sqrt{[\sum_{i=1}^{n}(m_i - \overline{m}_i)^2]}} \quad 4.3$$

where $\overline{m}$ =average simulated rainfall.

We hypothesized that the stochastic approach would outperform the ANN model in disaggregating the hourly to sub-hourly rainfall with the null hypothesis, H_0: the stochastic model performed equally with the ANN model. Subsequently, using a significance level of 5%, we used a one-sided paired Student t-test as well as a non-parametric Wilcoxon sign rank test (the latter to confirm that possible outliers do not impact the conclusion of the t-test)

4.2.5 Developing IDF curves

The Type-1 GEV distribution has been employed extensively in past studies owing to its flexibility and simplicity i.e., it only has two parameters (Phien, 1987). Previous studies by Mirhosseini et al.

(2014, 2013) reported that the GEV distribution well fitted developing rainfall IDF curves in the region, particularly the Gumbel distribution. The GEV probability distribution consists of three limiting forms i.e., Gumbel ($\xi \to 0$), Frechet ($\xi > 0$), and Weibull ($\xi < 0$) (Coles, 2001) and is defined as follows.

$$G(\mathrm{x}) = exp\left\{-\left[1+\xi\left(\frac{\mathrm{x}-\mu}{\sigma}\right)\right]^{-1/\xi}\right\} \text{ for } \quad x: 1+\xi\left(\frac{\mathrm{x}-\mu}{\sigma}\right) > 0 \tag{4.4}$$

where x is the rainfall intensity. μ, σ, and ξ are location, scale, and shape parameters respectively. The Gumbel distribution with $\xi \to 0$ is defined as

$$G(\mathrm{x}) = exp\left[-exp\left\{-\left(\frac{\mathrm{x}-\mu}{\sigma}\right)\right\}\right] \text{ for } \quad x: 1+\xi\left(\frac{\mathrm{x}-\mu}{\sigma}\right) > 0 \tag{4.5}$$

In addition, the parameter estimation is performed using maximum likelihood estimation since, if the model is correctly specified, it has optimal statistical properties compared to other methods such as the method of moments (Mahdi and Cenac, 2005). The KS test is used to test the goodness-of-fit at a significance level of 5% assuming the parameters are known (Delignette-Muller and Dutang, 2015), keeping in mind that, this test could be conservative i.e., not reject H_0 when it should Lilliefors (1967). The following procedure was used to obtain the IDF curves.

1) Obtain the annual maximum series of rainfall for a given duration (T) of 15-, 30-, and 45-min.
2) Evaluate the rainfall depth, X_T for a given return period (2-, 5-, 25-, 50-, and 100-year) for the Gumbel distribution which is given by.

$$X_T = \bar{x} + K_T S \tag{4.6}$$

where, $\bar{x}$, K_T, and S are mean, frequency factor, and standard deviation, respectively.

$$K_T = -\frac{\sqrt{6}}{\pi}\left[0.5772 + ln\left(ln\left(\frac{T}{T-1}\right)\right)\right] \tag{4.7}$$

3) The rainfall depths are plotted for each duration for different return periods.

4.3 Results and Discussion

The performance of the ANN in disaggregating 1-hour rainfall to monthly maximum 15-, 30-, and 45-min rainfall is reported below. The annual maximum rainfall intensities are then compared between the stochastic and the ANN models. Finally, using ANN, the results of the generated future IDF curves are presented alongside historical and projected future scenarios.

4.3.1 Performance of Bias correction and ANN for rainfall disaggregation

Bias correction improved the output of the climate models, especially the frequencies of wet days, annual average rainfall amount, and rainfall intensity. A detailed explanation for the performance of bias correction of hourly rainfall is given in Takhellambam et al. (2022a). The performance of disaggregated rainfall using the ANN approach was assessed by employing the Pearson correlation coefficient (r) and the Root mean square error (RMSE) in both training and test data for the generation of 15-, 30-, and 45-min monthly maximum rainfall and reported for the 187 rainfall stations. The minimum and maximum r values of the training datasets were 0.75 and 0.90, respectively (Fig. 4.3). On the other hand, as expected, the r values on the test datasets were found to be lower than those of the training datasets, with minimum and maximum of 0.62 and 0.88, respectively. The average r value for disaggregating to 15-min was found to be 0.84 and 0.77 for training and test data, respectively. Likewise, the RMSE value has an average value of 0.37 and 0.48 for training and test data, respectively.

The r value when disaggregating to 30-min rainfall was found to have an average value of 0.92 in training and 0.90 in test data. The range of values during training and testing were (0.89, 0.96) and (0.8, 0.97), respectively. Furthermore, we found that the RMSE value in both training and test data

ranges from 0.21 to 0.4, and 0.22 to 0.58, respectively (Fig. 4.3). Similarly, the disaggregation to 45-min rainfall was found to have an average r value of 0.95 and 0.93 in training and test data. The r values during training and test range from (0.92, 0.98) and (0.87, 0.98, respectively. RMSE values showed ranges of (0.16, 0.36) and (0.19, 0.48) for training and test data, respectively. These results are in line with the results of Zhao et al. (2021). As expected, the performance of the ANN is satisfactory with r greater than 0.60 in disaggregating to the monthly maximum sub-hourly scale using the hourly rainfall datasets (Mirhosseini et al., 2014). Moreover, we found a better performance for longer periods of 30- and 45-min of rainfall datasets compared to the 15-min disaggregating of monthly maximum rainfall data. This better performance of the ANN with longer durations for disaggregating rainfall datasets is consistent with Mirhosseini et al. (2014). One of the main reasons is that the hourly rainfall provides less information as the gaps in resolution become larger (Zhao et al., 2021), i.e., there is the smoothing of rainfall intensities while aggregating the 15-min to 30- and 45-min rainfall datasets (Op de Hipt et al., 2018).

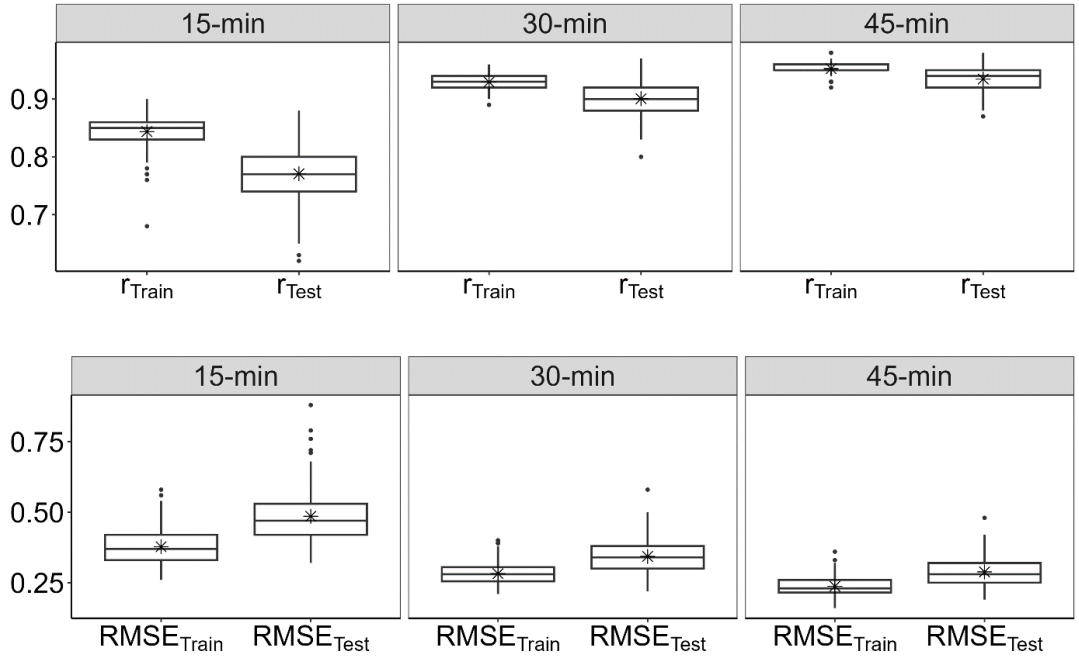

Fig. 4. 3 Boxplots showing the performance comparison of the ANN model for disaggregating hourly rainfall data to sub-hourly monthly maximum rainfall data during training (denoted by test) and testing (denoted by train) for 187 stations. Asterisk denotes the average value of the coefficient of correlation and RMSE value.

We further compared the performance of the ANN in disaggregating hourly rainfall to the sub-hourly monthly maximum with a recently developed stochastically-generated 15-min rainfall dataset of Takhellambam et al. (2022a). We compared the stochastic and ANN methods in generating the monthly maximum rainfall using the 1-hour data (Fig. 4.4 and 4.5). The quantile-quantile plot (at the top row of Fig. 4.4) shows that the performance of the stochastic method is closely related to the observed rainfall for smaller rainfall depths (the solid line represents the perfect model). However, as the rainfall depth increases, the stochastic model shows an increase in the variance in all the temporal scales of 15-, 30-, and 45-min. Takhellambam et al. (2022a) concluded that the stochastic method underestimated the rainfall intensities compared to the

observed datasets with an average NSE and r ranging from 0.48 to 0.8 and 0.78 to 0.9, respectively (Fig. 4.5).

The quantile-quantile plot of the ANN method shows a better performance with smaller variance than the stochastic method (Fig. 4.4), especially with higher rainfall intensities. The average NSE and r values were found in the range of 0.67 to 0.84 and 0.83 to 0.93, respectively (Fig. 4.5). This indicated that the ANN has a satisfactory performance when generating monthly maximum rainfall of 15-, 30-, and 45-min from 1-hour data since its NSE is greater than 0.6 (Mirhosseini et al., 2014).

Moreover, we found the null hypothesis of better performance of stochastic approach than the ANN model in disaggregating hourly data to a monthly maximum of sub-hourly rainfall data is rejected (p-value~0) using one-sided Student t-test and Wilcoxon sign rank test, favoring the alternate hypothesis (at a 5% significance level). Therefore, we conclude that the ANN model's performance is superior compared to the stochastic model in generating 15-, 30-, and 45-min monthly maximum rainfall from 1-hour rainfall. Previous studies also found similar results of superior performance by the ANN model over other disaggregation methods, especially compared to the stochastic method (Mirhosseini et al., 2014; Zhao et al., 2021). This is because neural networks can perform better in approximating complex relationships. The unique structure of the ANN, which connects each hidden layer to the output nodes provides a better approximation of complex non-linear relationships with no major distributional assumptions (Dibike and Coulibaly, 2006; Mirhosseini et al., 2014).

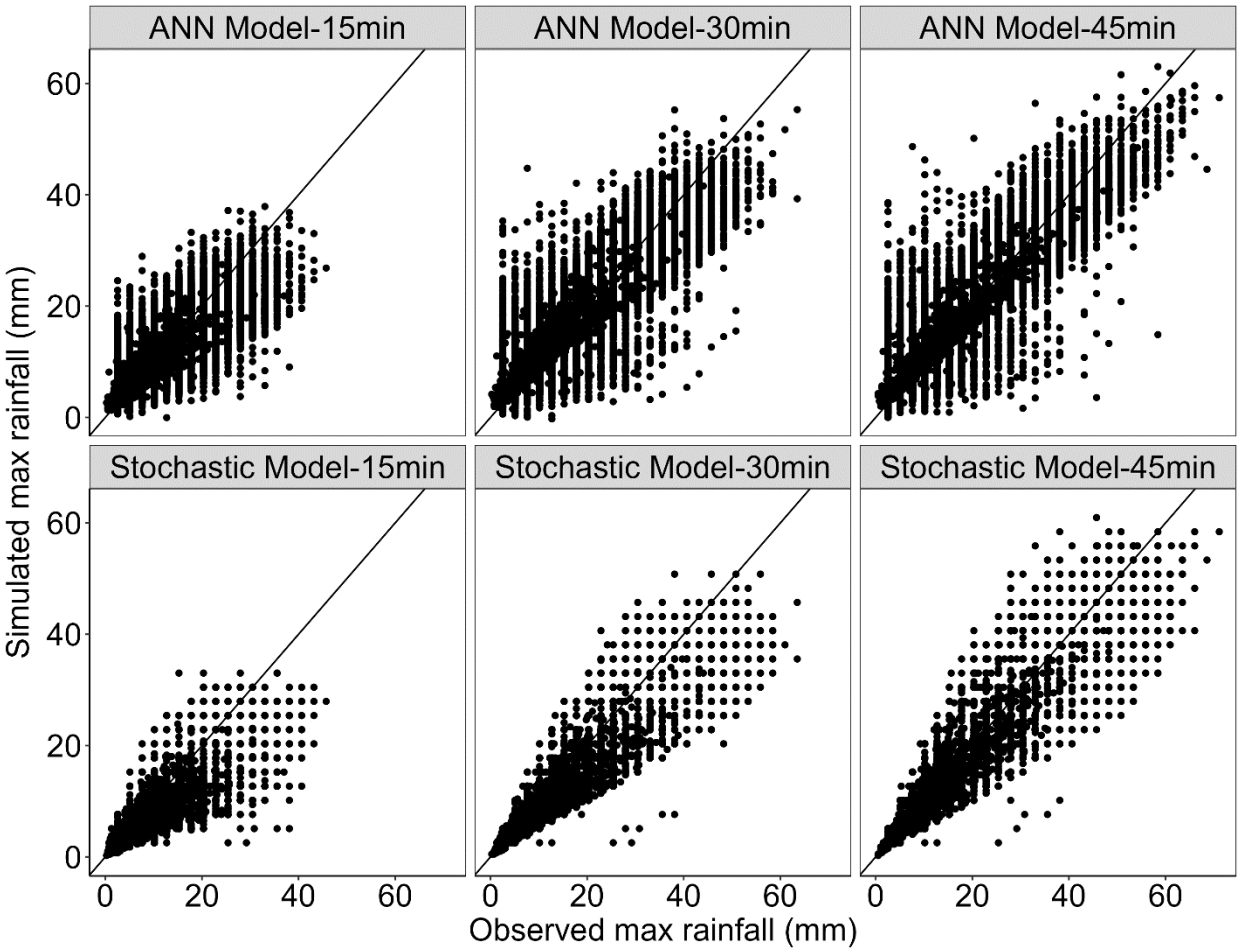

Fig.4.4 Quantile-quantile plot for comparing ANN and stochastic model in downscaling monthly maximum of 15-, 30-, and 45-min rainfall for all 187 stations.

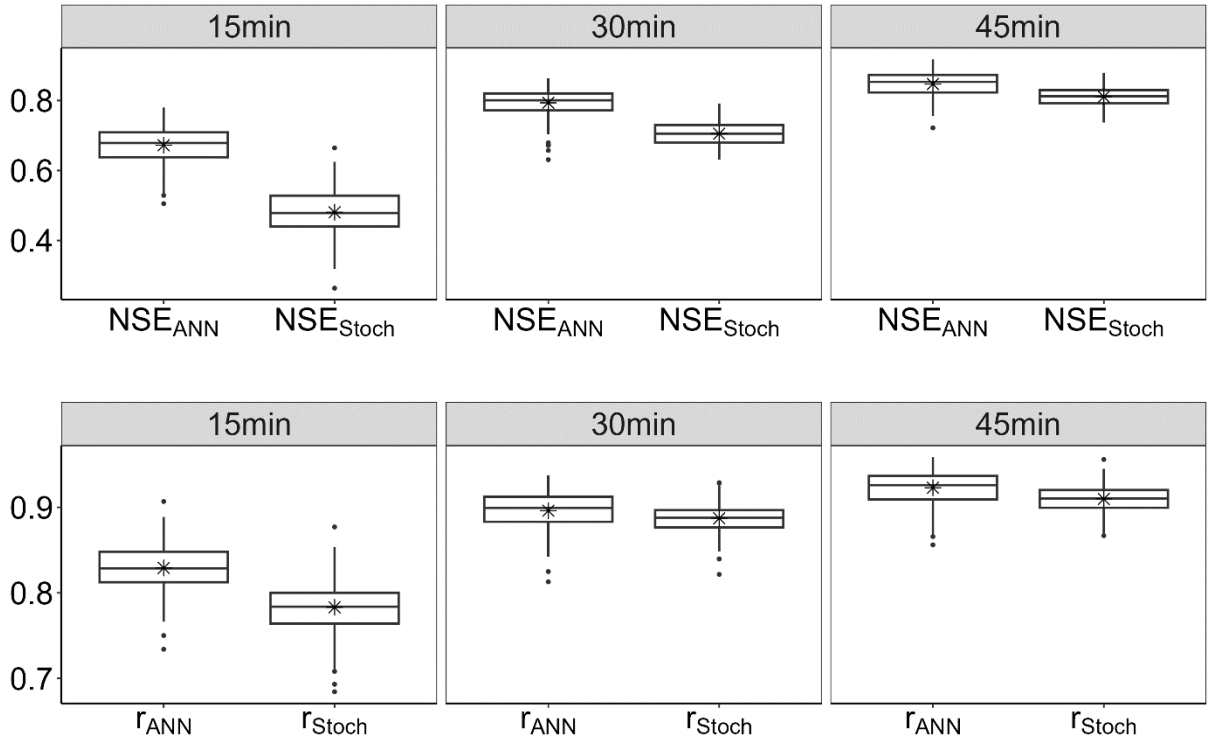

Fig. 4.5 Boxplots showing the statistical comparison between ANN (denoted by ANN) and stochastic (denoted by Stoch) model for disaggregating hourly rainfall data to sub-hourly monthly maximum rainfall for 187 stations. Asterisk denotes the average value of the coefficient of correlation and NSE value.

4.3.2 Rainfall Intensity Duration Frequency Curves

The future projected rainfall IDF curves were developed using durations of 15-, 30-, and 45-min with return periods of 2-, 5-, 10-, 25-, 50-, and 100-year using five climate models under the RCP8.5 scenario for the Southeast United States. We used kriging interpolation to generate a spatial variation of extreme rainfalls that provides an understanding and identification of extreme rainfall areas. This resulted in 90 different maps (5 RCMs per 6 Return Periods per 3 Durations). For brevity, we provide maps for all durations with return periods of 25-, 50-, and 100-year for the CANESM and the remaining models are presented in Fig. 4.6 and Appendix C1 (C1.1-1.4), respectively. Fig. 4.6 shows the spatial variations of future projected annual maximum rainfall of

15-, 30-, and 45-min with a return period of 25-, 50-, and 100-year using the CANESM model. This provides information on rainfall magnitude and recurrence of extreme rainfall depths based on frequency analysis (Ragno et al., 2018).

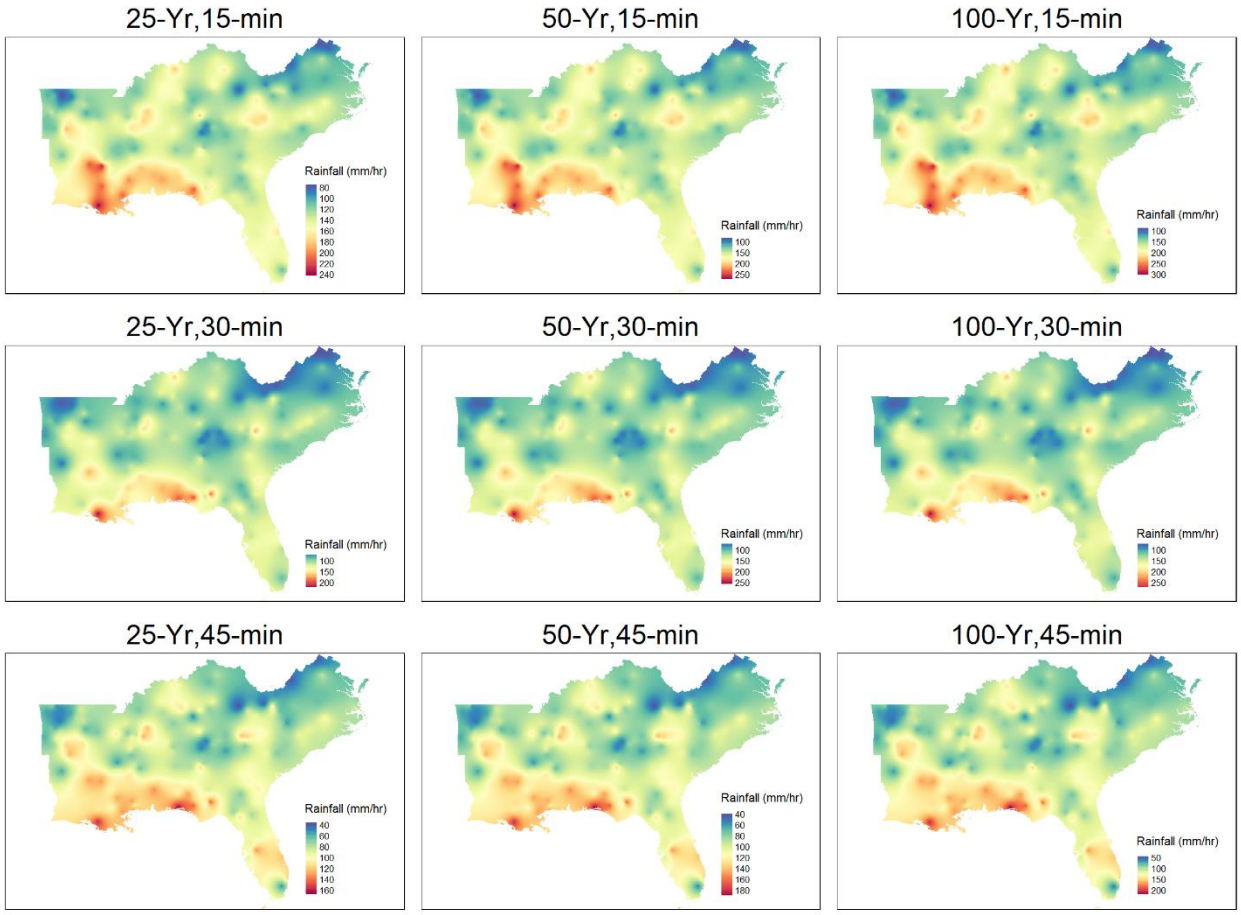

Fig. 4.6 Map showing the spatial variation of rainfall depth for 15-, 30-, and 45-min with a return period of 25-, 50-, and 100-year under CANESM.

The maximum annual rainfall intensity using the duration of 15-min under the CANESM model was found to range from 30 to 234 mm h^{-1} under 2-, 5-, 10-, 25-, 50-, and 100- year return periods. Likewise, the maximum annual rainfall intensity for the remaining duration of 30-, and 45-min ranged from 22 to 193 mm h^{-1} and 15 to 148 mm h^{-1}, respectively. We observed (Fig. 4.6) that the extreme rainfall of annual maximum of 15-, 30-, and 45-min with the return period of 25-, 50-

, and 100-year are mostly found in both the Gulf-Atlantic coast and the Appalachian Mountains. The remaining climate models also found results consistent with this (see Appendix C1). This demonstrates the similar higher and lower trend of both annual average and maximum rainfall over the region (Takhellambam et al., 2022a). Among these models, the MPIREG model found greater maximum rainfall intensities. The remaining models of HADGEM, GFDL, MPIREG, and MPIWRF for all durations showed maximum rainfall intensities ranging from 20 to 227 mm h^{-1}, 16 to 168 mm h^{-1}, 16 to 259 mm h^{-1}, and 16 to 239 mm h^{-1}, respectively, in given return periods of 2-, 5-, 10-, 25-, 50-, and 100-year. The differences among these models, among others, are due to the different mechanisms for generating rainfall (Mirhosseini et al., 2014). These multiple models enable us to quantify the ranges of maximum rainfall intensities.

Convective rainfalls cause more rain to fall along the Gulf and Atlantic coasts. This is due to the warm, humid, and subtropical air from the coastal areas that result in a greater number of intense rainfall events, especially from May to September (Kim et al., 2020; Perica et al., 2013). This further brings intense rainfall inland and provides greater rainfall in the flat regions (Takhellambam et al., 2022b). Moreover, the Appalachian Mountains receive higher rainfalls due to the orographic effect (Takhellambam et al., 2022b). In addition, the 15-min datasets have greater intensities as compared to the aggregated datasets of 30 and 45-min which is due to the smoothing of rainfall intensities. For instance, the peak rainfall intensity of smaller temporal scales is averaged over the scale of 30-min or 45-min resulting in decreased intensity.

For better discussion, we selected five rain-gauge stations across the region (Table 4.1), three of which are in urban areas, namely Venice, New Orleans Audubon, and Mullins, while the other two are in sparsely inhabited areas. Table 4.2 shows the comparison of annual maximum rainfall of 15- and 30-min duration with return periods of 2-, 5-, 10-, 25-, 50-, and 100-year between our

study using the observed data (hereinafter referred to as OBS in Table 4.2) and findings of NOAA's National Weather Service (hereinafter referred to NWS) Atlas 14, volume 9, version 2 (Perica et al., 2013). The NWS findings of annual maximum rainfall of 15-min with a 2-year return period show a range from 82 to 120 mm h^{-1}. Moreover, the extreme rainfall depth of 100-year shows a minimum and maximum of 162 mm h^{-1} and 238 mm h^{-1} respectively. Our study using the observed annual maximum rainfall of 15-min ranged from 65 to 103 mm hr^{-1} with a recurring period of 2-year. In addition, a 100-year return period of 15-min rainfall depth shows rainfall in the range of 122 to 168 mm h^{-1}, respectively. Furthermore, the NWS's annual maximum rainfall of 30-min in all return periods ranges from 60 to 187 mm h^{-1}, while our study shows rainfall was in the range of 43 to 125 mm h^{-1}.

All the annual maximum rainfalls in our study have been underpredicted compared to the NWS findings that range from 10 % to 41%. One of the primary reasons for the disparity in rainfall depths is the parameter estimation approach used for the Gumbel distribution which then allows to delivery of the IDF curves. For example, NWS used L-moment-based regional frequency analysis, whereas our study used maximum likelihood estimation.

Table 4.1 Description of selected locations for the assessment of IDF curves.

Sl No	Name of Station	Latitude (°N)	Longitude (°W)	Elevation (feet)
1	Huntsville 1 SSW	36.07	-93.75	1783
2	Venice	27.1	-82.44	8
3	Unicoi State Park	34.72	-83.72	1594
4	New Orleans Audubon	29.92	-90.13	20
5	Mullins	34.19	-79.25	110

Table 4.2 Comparison of annual maximum rainfall (in mm h^{-1}) of 15- and 30-min duration with return periods of 2-, 5-, 10-, 25-, 50-, and 100-year between our study using the observed data (denoted by OBS) observed data and findings of NOAA's National Weather Service (denoted by NWS).

Station	Dur	Return Period (years)											
		2		5		10		25		50		100	
		NWS	OBS	NWS	OBS	NWS	OBS	NWS	OBS	NWS	OBS	NWS	OBS
Huntsville 1 SSW	15-min	82	65	98	80	112	90	132	103	147	113	162	122
	30-min	60	43	73	50	83	56	97	62	109	67	120	71
Venice	15-min	120	98	142	115	159	125	182	139	200	149	216	158
	30-min	90	64	107	77	120	85	137	96	150	104	163	112
Unicoi State Park	15-min	90	69	108	85	124	96	147	109	166	119	186	129
	30-min	64	44	77	54	89	61	105	70	119	76	133	82
New Orleans Audubon	15-min	114	103	138	120	159	132	189	147	213	157	238	168
	30-min	88	69	107	84	124	94	148	107	167	116	187	125
Mullins	15-min	109	76	128	94	143	106	161	121	175	132	188	144
	30-min	75	48	91	60	104	68	119	77	132	84	144	91

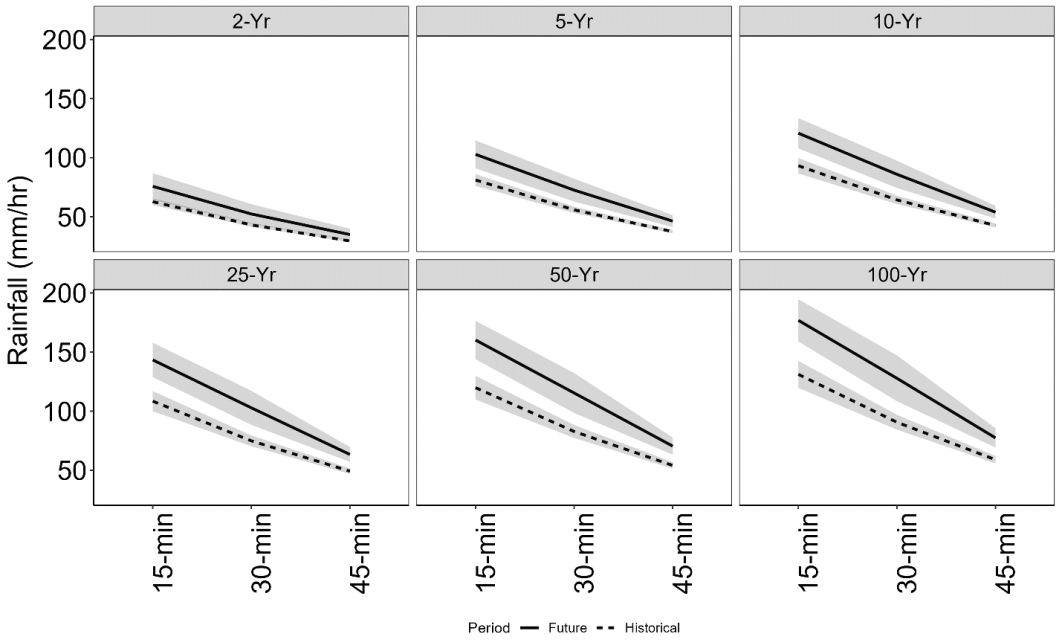

Fig. 4.7 Ensemble IDF curves with 95% confidence interval for historical and future projected located at Unicoi State Park under the RCP8.5 scenario with 2-, 5-, 10-, 25-, 50-, and 100-year return periods using ANN.

Table 4.3 Comparison of relative change (in %) in annual maximum of rainfall between future projected and historical rainfall IDF curves using ANN.

Station	**Dur**	**Return Period (years)**					
		2	**5**	**10**	**25**	**50**	**100**
Huntsville 1 SSW	15-min	12	16	19	21	22	23
	30-min	7	9	9	10	10	11
	45-min	9	14	17	19	21	22
Venice	15-min	11	12	13	14	15	15
	30-min	12	15	16	17	18	19
	45-min	16	18	18	19	19	20
Unicoi State Park	15-min	18	22	23	25	26	27
	30-min	18	23	25	27	28	29
	45-min	16	19	20	22	23	23
New Orleans Audbon	15-min	8	14	18	22	24	26
	30-min	10	18	22	26	28	31
	45-min	12	22	27	31	34	36
Mullins	15-min	10	10	10	11	11	11
	30-min	19	21	21	22	23	23
	45-min	19	21	22	23	23	24

For the same locations discussed above (Table 4.1), we compared annual maximum rainfall between the future projected and historical scenarios. We combine all five climate model outputs as a single ensemble. This allows the combining of various sources of information from different models to minimize the uncertainty associated with each model. We further show the ensemble annual maximum rainfall (Fig. 4.7) of 15-, 30-, and 45-min with return intervals of 2-, 5-, 10-, 25-, 50-, and 100-year between the historical and future periods using the ANN located at Unicoi State Park (34.72°N, -83.72°W). The shaded area represents both future and historical IDF curves with 95% confidence intervals. We refer the reader to Appendix C2 (C2.1-2.4) for the remaining four locations of Huntsville 1 SSW, Venice, New Orleans Audubon, and Mullins. We found that the historical annual maximum rainfall at Unicoi State Park ranges from 26 to 54 mm h^{-1} with a return period of 2-year. The rainfall intensities increase with larger recurring intervals, with the greatest value in 100-year that ranges from 49 to 107 mm h^{-1}. Moreover, we found that the annual maximum rainfall under future scenarios increased compared to the historical period for each duration and recurring interval. The rate of increase in the future rainfall intensity ranges from 16% to 29% (Table 4.3).

Similarly, the historical annual maximum rainfall of 15-, 30-, and 45-min with a return period of 2-, 5-, 10-, 25-, 50-, and 100-year in the remaining locations has a minimum and maximum of 25 to 134 mm h^{-1}. Future scenarios show increasing rainfall intensities in all of the locations as compared to the historical period ranging from 7% to 36%. Overall, the minimum and maximum rainfall intensities under future scenarios were found in the range of 28 to 169 mm h^{-1}. The aforementioned findings indicate that the future projected extreme rainfall depths are significantly increased from the historical scenario for the Southeast United States.

4.3.3 Uncertainty in the IDF Curves

Large uncertainties are associated with developed IDF curves owing to the variety of factors in both observed and model datasets. Most of the observed rainfall measurement methods and products are associated with inaccurate measurements due to the loss of rainfall characteristics i.e., amount, frequency, and intensity. This includes human error, measurement thresholds, evaporation, and wind effects. However, it is challenging to verify these errors in our rainfall dataset of observed events (Zhao et al., 2021).

According to Mirhosseini et al. (2013), uncertainty may result from the physical parametrization of climate models, such as the development of the rainfall process in various models, or the varied boundary conditions of climate projections. In addition, the typical climate model bias is a consequence of many wet days with low rainfall intensities (Takhellambam et al., 2022a). Therefore, we are using multiple climate models to capture the various uncertainties associated with different climate models. The uncertainty associated with each model for future projected rainfall IDF curves was quantified with mean rainfall values along with standard deviation using all stations (Fig. 4.8). Under the CANESM model, the mean rainfall intensities and standard deviation range from 34 to 130 $mm\,h^{-1}$ and 8 to 28 $mm\,h^{-1}$, respectively. Likewise, the remaining models show both mean rainfall intensity and standard deviation in the range of 34 to 135 $mm\ h^{-1}$ and 7 to 28 $mm\ h^{-1}$, respectively. Among all of the models, the minimum and maximum standard deviations were 7 $mm\ h^{-1}$ and 28 $mm\ h^{-1}$ under GFDL and CANESM, respectively.

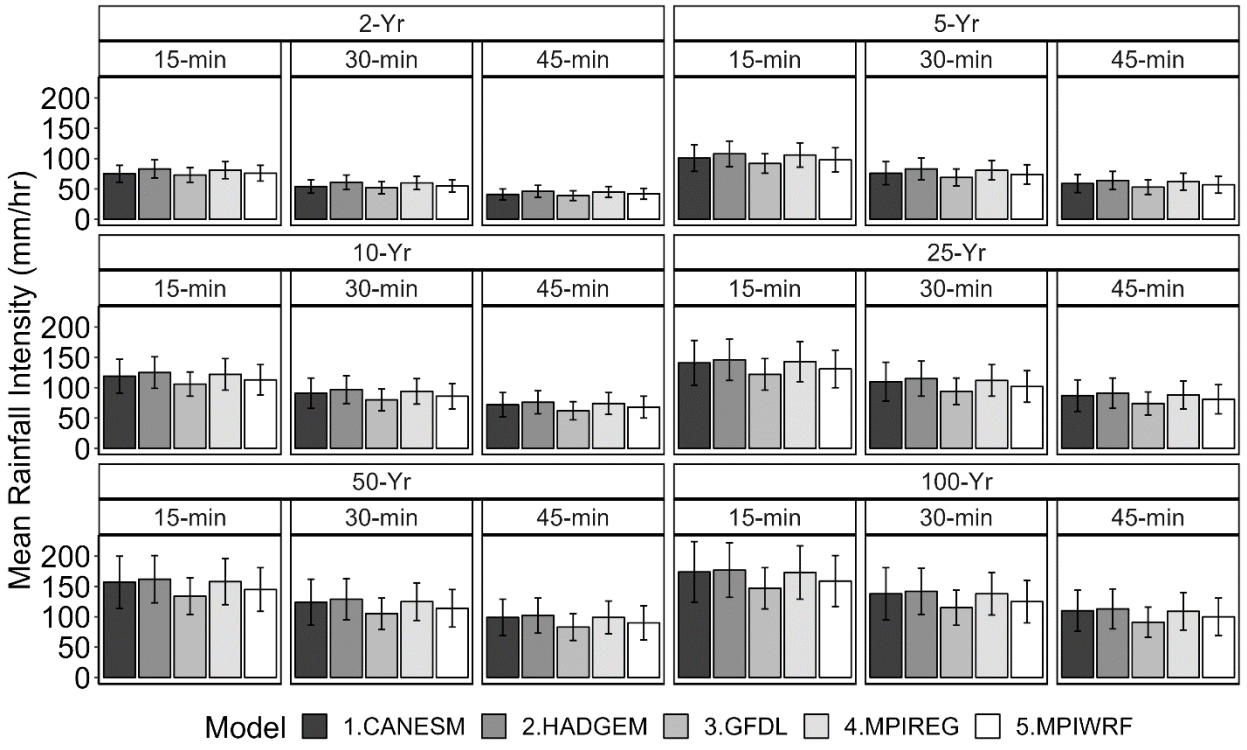

Fig. 4.8 Bar plots showing mean rainfall intensity with ±1standard deviation of projected future rainfall IDF curves for five climate models with 2-, 5-, 10-, 25-, 50-, and 100-year return periods using ANN over the southeastern United States.

The variability in rainfall IDF curves among different climate models is due to the different boundary conditions used for precipitation generation. For instance, the annual maximum of 1-day rainfall (RX1day) varies with each climate model. Supari et al. (2020) found that a climate model shows greater rainfall as much as five times for the same location than the remaining models. One of the main reasons is the inability of the model to represent topography, vegetation, and atmospheric conditions (Vizy and Cook, 2012), although, extreme rainfalls could be represented with a finer resolution of climate models (Kitoh and Endo, 2016). Moreover, the projected rainfall characteristics may not always be similar to that of observed rainfall datasets.

Therefore, Giorgi et al. (2013), Mirhosseini et al.(2013), Supari et al.(2020), and Zhao et al.(2021) recommended using multiple climate models for hydrological applications. Moreover, the superior performance of the ANN over the stochastic model has resulted in reliable IDF curves. This has also been found in various previous studies (Burian et al. 2001; Dibike and Coulibaly,2006; Mirhosseini et al.,2014; Zhao et al.,2021). Burian and Durrans (2002) found the ANN to be a viable option for disaggregating hourly to sub-hourly rainfalls. On the other hand, despite choosing a particular disaggregating method, we found that most of the climate models show an increasing extreme rainfall depth over the Southeast United States.

4.4 Conclusions

We developed future projected rainfall IDF curves using a monthly maximum rainfall sub-hour (15-, 30-, and 45-min) scale of rainfall with a return period of 2-, 5-, 10-, 25-, 50-, and 100-year. These maximum values were obtained by developing 561 ANN models for the Southeast United States. This study confirms the satisfactory performance of the computationally efficient feed-forward back-propagation ANN model in disaggregating monthly maximum rainfalls to sub-hourly scales from hourly scales. Moreover, the model also showed better performance than the stochastic model for generating sub-hour monthly maximum rainfall with an average NSE ranging from 0.67 to 0.84. The training and test results of the ANN models were evaluated with two statistical measures consisting of the coefficient of correlation and the root mean squared error which highlighted its satisfactory performance in disaggregating the monthly maximum rainfall depths. These results were further supported by the quantile-quantile plot and boxplots of NSE. The average NSE using the ANN model for 15-min is greater than 0.6 indicating a satisfactory performance. In addition, we also found that there is a significantly better performance of the ANN over the stochastic model by rejecting the null hypothesis at a 5% significant level. The null

hypothesis of better performance of stochastic approach than the ANN model in disaggregating hourly data to a monthly maximum of sub-hourly rainfall data is rejected (p-value~0) using a one-sided Student t-test and Wilcoxon sign rank test. These findings also showed that the ANN model is superior to the stochastic model in generating monthly maximum rainfall. These results are further improved with larger temporal scales of 30-min and 45-min. The Kolmogorov-Smirnov test supports the assumption that the annual maximum rainfalls come from Gumbel extreme distribution. A comparison of five selected locations showed that the estimated observed annual maximum rainfall of 15-min and 30-min with a recurring interval of 2-, 5-, 10-, 25-, 50-, and 100-year are found to be closely related to reported rainfall values of NWS. The results show an increasing rate of future rainfall compared to the historical period by 7% to 36%. The mean projected future rainfall intensities over the southeast United States range from 34 to 135 mm h^{-1} for a duration of 15-, 30-, and 45-min with a return period of 2-, 5-, 10-, 25-, 50-, and 100-year. In addition, the standard deviation ranges from 7 to 28 mm h^{-1} between five climate models. The spatial variation of future projected extreme rainfall depths showed that the Gulf-Atlantic coast and the Appalachian Mountains are projected to receive more extreme rainfalls. This finding confirms the need to update future IDF curves which can better inform the design of water resource infrastructures.

CHAPTER 5

Quantifying Uncertainty in Projected Rainfall Intensity Duration Frequency Curves Using Artificial Neural Network and Bootstrapping Resampling Technique

5.1 Introduction

Climate change has increased extreme rainfall events in both magnitude and frequency in many parts of the United States and climate models project similar trends to continue into the 21st century (Lopez-Cantu et al., 2020; Prein et al., 2017). The observed extreme events of daily rainfall with 76.2 mm or more had an estimated average of 0.95 days per year in the 1900s and escalated during the 1990s, 2000s, and 2010s by 23%, 16%, and 20%, respectively (Takhellambam et al., 2023). IPCC (2018) reported that temperature is further expected to increase by 1.5℃ with the current rate of emission of greenhouse gases from 2030 to 2052. As temperature increases, so does the rate of evaporation and amount of moisture in the atmosphere (Wang et al., 2016). Greve et al. (2014) reported 10.8% of the global land area has found a robust pattern of 'dry gets drier, wet gets wetter'. Moreover, rainfall intensity is likely to increase up to 7% per unit degree Celsius increase in temperature (Easterling et al., 2017).

One of the consequences of extreme rainfall events is flooding which adversely impacts the socio-economy of a region. The magnitude of flood could be further augmented as a result of urbanization, i.e., the increase in pavements and impermeable surface area, ultimately leading to an increase in flash floods by reducing runoff time (Zhao et al., 2023). Therefore, developing accurate rainfall IDF curves for designs of hydrological and hydraulic infrastructure, for instance, dams, sediment control structures, and stormwater drainage systems would help to lessen the impact of extreme rainfall events (Almazroui et al., 2019; Ng et al., 2019). The existing structures in the United States are based on historical extreme rainfall events, and new infrastructures should

be designed with consideration of projected future extreme rainfall events (Lopez-Cantu et al., 2020). Many studies have suggested that the non-stationarity of climatic patterns is increasing and IDF curves based on stationary assumptions underestimated the extreme rainfall events (Mirhosseini et al., 2014; Sarhadi and Soulis, 2017; Vu and Mishra, 2019; Zhu, 2013; Zhu et al., 2012).

Estimation of projected rainfall IDF curves is particularly needed for the Southeast United States as the region is expected to undergo significant changes in rainfall characteristics (McGehee and Srivastava, 2018). Previous studies (Cheng and AghaKouchak, 2014; Ganguli and Coulibaly, 2019; Ghasemi Tousi et al., 2021; Mirhosseini et al., 2014, 2013; Sarhadi and Soulis, 2017; Zhu, 2013; Zhu et al., 2012) used aggregated rainfall (hourly or daily) for developing IDF curves considering the non-stationary under changing climatic patterns. However, aggregated rainfall is underpredicted as compared to a breakpoint or sub-hourly rainfall due to smoothing (McGehee and Srivastava, 2018; Takhellambam et al., 2023). Therefore, Mirhosseini et al. (2015, 2014, 2013) and Chapter-4 developed IDF curves using sub-hourly rainfalls for the southeastern United States considering the non-stationarity of future projected rainfall events.

The climate models are associated with various uncertainties such as epistemic uncertainties (Al Kajbaf et al., 2023; Emmanouil et al., 2022), due to a lack of understanding of physical processes, insufficient information, or analytical resources (Mirhosseini et al., 2015; Solaiman, 2011). Furthermore, future climate models are based on greenhouse gas concentrations in the atmosphere and the carbon cycle, both of which are subjected to uncertainties (Solaiman, 2011). These uncertainties associated with the IDF curves are further augmented with choices of statistical modeling such as distribution and parameter estimation (Al Kajbaf et al., 2023; Takhellambam et al., 2022c).

Therefore, uncertainty quantification, particularly for extreme rainfall events is useful for stakeholders, e.g., policymakers, researchers, and farmers, that are engaged in adaptation and mitigation to climate change. Uncertainty quantification can help to account for the variability in climate models output and account for it during the management practices development process (Ng et al., 2019). Therefore, better decision-making for climate adaptation and mitigation by stakeholders requires accurate uncertainty estimates (Katz et al., 2013; Guttorp, 2012).

Mirhosseini et al. (2013) developed future IDF curves using six global and regional climate models over Alabama, USA using a stochastic rainfall disaggregation method and generalized extreme value distribution. The findings suggested accounting for uncertainty analysis is extremely important in the datasets generated from the climatic models. Mirhosseini et al. (2014) further improved rainfall disaggregation generated by a stochastic method through a feed-forward back propagation artificial neural network model while generating sub-hourly rainfalls. Using these rainfall datasets, IDF curves were developed using the generalized extreme value (GEV) distribution over Alabama. Additionally, IDF curves were created (Chapter-4) for the Southeast United States using the Gumbel distribution and a modified ANN approach for generating disaggregated sub-hourly monthly maximum using hourly rainfall. However, no hyperparameter adjustment for disaggregation was performed in any of the rainfall disaggregation algorithms in earlier investigations. Considering these limitations, our study aims to quantify the uncertainty associated with future projected rainfall IDF curves for selected 11 largest cities of the Southeast United States under the RCP8.5 scenario using rainfall datasets of 2030 to 2059. Therefore, the objectives of this study were to:

i. Evaluate the effect of Hyperparameter tuning on Neural network's performance for rainfall disaggregation;

ii. Quantify the impact of bias correction on IDF curves; and

iii. Quantify uncertainty in IDF curves using Bootstrapping resampling technique.

5.2 Data and Study Area

We selected the 11 largest cities (one city per state) from the states of Alabama, Arkansas, Florida, Georgia, Kentucky, Louisiana, Mississippi, North Carolina, South Carolina, Tennessee, and Virginia of the southeastern United States. Rainfall in the study region ranges from 1000 to 1250 mm per year, which is significantly higher than the national average of 856 mm (Ingram et al., 2013; Takhellambam et al., 2022a).

The National Oceanic and Atmospheric Administration National Climatic Data Center (NOAA NCEI, 2014) provides measured 15-minute rainfall data from 1971 to 2013. We filtered rainfall stations using 20.11 screening method to remove stations having rainfall datasets of fewer than 20 years and complete measured rainfall of fewer than 11 months each year (Takhellambam et al., 2022a). We selected 11 rainfall stations nearest each state's largest city (Fig 5.1 and Table 5.1).

Historical (1970-1999) and future (2030-2059) projected rainfall were obtained for 5 climate models from the North American-Coordinated Downscaling Experiment (NA-CORDEX) having a temporal and spatial resolution of 1-hr and ~50 km respectively. The models are represented with CANESM (Canadian Earth System Model- Canadian Regional Climate Model version 4), HADGEM (Hadley Centre Global Environment Model version 2 Earth system model- Weather Research and Forecasting), GFDL (Earth System Model – Geophysical Fluid Dynamics Laboratory), MPIREG (Regional Climate Model version 4, Max Planck Institute for Meteorology Earth System Model LR), and MPIWRF (Weather Research and Forecasting, Max Planck Institute for Meteorology Earth System Model LR) (Giorgi and Anyah, 2012; Scinocca et al., 2016; Skamarock et al., 2005). These models were forced with RCP8.5 scenario.

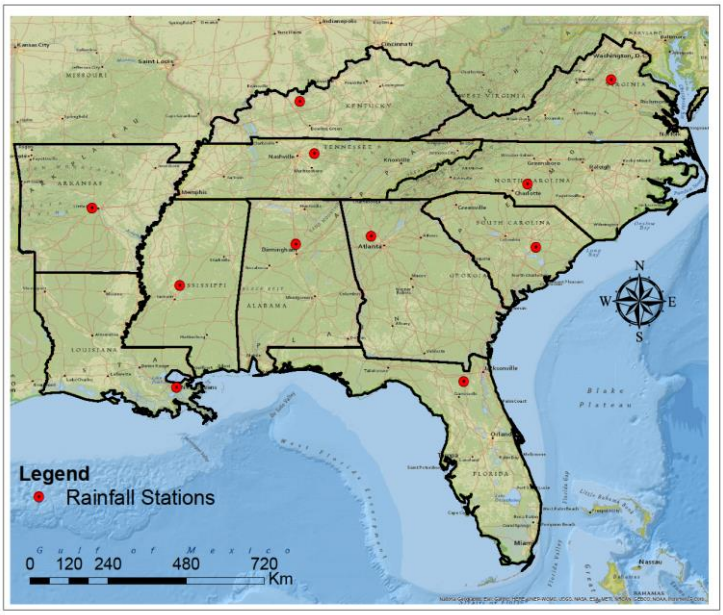

Fig. 5.1 Map showing the locations of 11 rainfall stations.

Table 5.1 Descriptions of 11 rainfall station locations.

No.	Name of Sites	State	Longitude (°W)	Latitude (°N)
1	Warrior	Arkansas	92.33	34.74
2	Ferndale 6 E	Louisiana	90.07	29.95
3	Raiford State Prison	Mississippi	90.18	32.30
4	Dallas 7 Ne	Alabama	86.81	33.52
5	Fordsville	Tennessee	86.78	36.17
6	New Orleans Audubon	Kentucky	85.77	38.25
7	Canton 4n	Georgia	84.39	33.75
8	Mount Pleasant	Florida	81.66	30.34
9	Manning	Virginia	75.98	36.85
10	Lebanon	North Carolina	80.84	35.22
11	Piedmont Research Sta	South Carolina	79.93	32.77

5.3 Methodology

5.3.1 Bias correction

The climate models should be bias-corrected due to errors associated with a greater number of rainy days that result in smaller rainfall intensities as compared to the observed rainfall, particularly for the NA-CORDEX rainfall datasets (Takhellambam et al., 2022a). The Quantile delta mapping method was used as given below (equation 5.1) for bias correction.

$$\hat{x}_{m,p.adjst.} = x_{m,p} \frac{F_o^{-1}\left(F_{m,p}\left(x_{m,p}\right)\right)}{F_{m,h}^{-1}\left(F_{m,p}\left(x_{m,p}\right)\right)} \quad 5.1$$

where, *o*, *h*, and *p* are observed, historical, and projected scenarios respectively. *m* indicates the climate model. In addition, *F* is the cumulative probability distribution function (CDF).

5.3.2 Hyperparameter tuning of rainfall disaggregation

The architecture of the multi-layered perceptron is provided in Fig 5.2 for disaggregation of hourly to sub-hourly monthly maximum rainfall. A detailed methodology has been described in the 4.2.3 section. Chapter-4 advocated this method for rainfall disaggregation from hourly to sub-hourly rainfall using an artificial neural network model. This model is associated with various hyperparameters, i.e., number of neurons per layer, learning rate, dropping rate, and activation function which cannot be streamlined during the training. Hyperparameter tuning selects an optimal value for hyperparameters, otherwise, the model will have lesser accuracy (Amini et al., 2023). This study used a commonly used random search method for tuning the hyperparameters due to better efficiency than other methods such as grid search and manual search (Bergstra and Bengio, 2012).

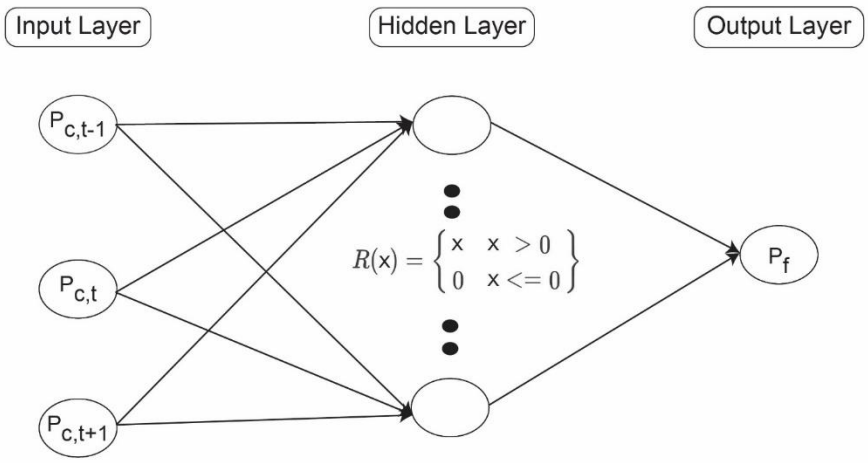

Fig. 5.2 Rainfall disaggregation using artificial neural network. Here, c and f represent hourly and finer (sub-hourly) monthly maximum rainfall (P) at the time (t). In addition, t-1 and t+1 indicate previous and subsequent hour rainfall datasets, respectively.

Random search tuning of hyperparameters searches the possible values through randomization from a given range of hyperparameters' values. This algorithm has an advantage over the grid search with fewer iterations in selecting the optimal hyperparameter values (Amini et al., 2023). The following hyperparameters' ranges were used considering the results from Chapter-4.

Table 5.2 Range or set of hyperparameter values used for tuning ANN for disaggregating hourly to sub-hourly rainfall using Random Search.

No.	Hyper Parameters	Range/Sets of Values
1	Activation function	ReLU, tanh, and sigmoid
2	Batch Size	[16, 32, 64, 128]
3	Dropout rate	[0.2, 0.3, 0.4, 0.5]
4	Optimizer ADAM	[0.0008, 0.001, 0.01]
5	epochs	[10, 100, 1000, 5000]
6	Learning rate	[0.0001, 0.001, 0.01]
7	# Neuron	16-32

5.3.3 Development of IDF curves using Bootstrapping resampling approach

The study used the bootstrap resampling method, considering both simplicity and a computationally efficient approach for quantifying the uncertainty associated with IDF curves. The method allows a generation of large samples of datasets with replacement and resampling of original datasets assuming independent and identically distributed samples (Ng et al., 2019). The sampling used in this bootstrapping technique involved the following steps:

1. Assume the monthly maximum rainfall for sub-hourly durations of 15-, 30-, and 45-min are $X = X_1, X_2, \dots, X_n$, where n is the total number of rainfall records.
2. Random selection of monthly maximum rainfalls with replacement from the original rainfall sample. The resampling was repeated 10,000 times to ensure reliable and accurate estimation of parameters, $X' = X_1'^{(i)}, X_2'^{(i)}, \dots, X_n'^{(i)}$, where $i = 1, 2, \dots, 10000$ (Ng et al., 2019).

The generated rainfall samples were further used to develop IDF curves using Gumbel distribution with suggestions from previous studies of Mirhosseini et al. (2014) and Chapter-4. The probability distribution is given as (equation 5.2)

$$G(\mathrm{x}) = exp\left[-exp\left\{-\left(\frac{\mathrm{x}-\mu}{\sigma}\right)\right\}\right] \text{ for } \quad x: 1 + \xi\left(\frac{\mathrm{x}-\mu}{\sigma}\right) > 0 \qquad 5.2$$

where x is the monthly maximum rainfall. μ, σ, and ξ are location, scale, and shape parameters, respectively.

Maximum likelihood estimation is used to estimate the parameters, provided the model is adequately stated. It has the best statistical qualities when compared to other techniques like the method of moments (Mahdi and Cenac, 2005). We followed the procedure described in Chapter-4 for developing the IDF curves stated below:

1. Extract annual maximum rainfall for each duration of 15-, 30-, and 45-min.
2. Calculate rainfall depth, X_T for return periods of 2-, 5-, 25-, 50-, and 100-year) using Gumbel distribution as given below (equation 5.3)

$$X_T = \bar{x} + K_T S \quad 5.3$$

where, $\bar{x}$ and S are mean, and standard deviation, respectively. Frequency factor, K_T is given by (equation 5.4)

$$K_T = -\frac{\sqrt{6}}{\pi}\left[0.5772 + ln\left(ln\left(\frac{T}{T-1}\right)\right)\right] \quad 5.4$$

5.4 Results and Discussion

This study assessed and quantified factors responsible for the uncertainty associated with the development of rainfall IDF curves. These include hyperparameter tuning, bias correction, and bootstrapping techniques.

5.4.1 Performance of rainfall disaggregation with hyperparameter optimization

Results showed that each station had a distinct combination of hyperparameters of the multi-perceptron network (Table 5.3). We found ReLU activation function was most commonly used followed by tanh and sigmoid. The batch sizes ranged from 16 to 128, with the highest number of epochs being 5000. The dropout rate varied from 0.2 to 0.5, indicating a relatively high regularization level to prevent overfitting. The learning rate ranged from 0.0001 to 0.01, with a higher learning rate being used in some cases. The optimizer used ranged from 0.0008 to 0.01. The number of neurons varied from 18 to 30. It is important to highlight that these results implied that the selection of hyperparameters depends on the particular dataset and problem being addressed.

Table 5.3 Optimal hyperparameters of ANN for rainfall disaggregation of hourly to sub-hourly scale for 11 locations using Random Search.

List	activation	batch	Dropout	epochs	Learning rate	Optimizer	# Neuron
1	ReLU	32	0.4	1000	0.001	0.01	26
2	ReLU	128	0.3	5000	0.001	0.01	19
3	tanh	16	0.5	5000	0.0001	0.0008	28
4	sigmoid	16	0.2	1000	0.001	0.0008	27
5	ReLU	128	0.3	100	0.001	0.01	30
6	tanh	16	0.5	5000	0.0001	0.0008	28
7	ReLU	64	0.4	5000	0.01	0.001	23
8	sigmoid	16	0.2	1000	0.001	0.0008	27
9	ReLU	128	0.4	1000	0.01	0.001	27
10	sigmoid	128	0.4	5000	0.0001	0.01	18
11	tanh	16	0.5	5000	0.0001	0.0008	28

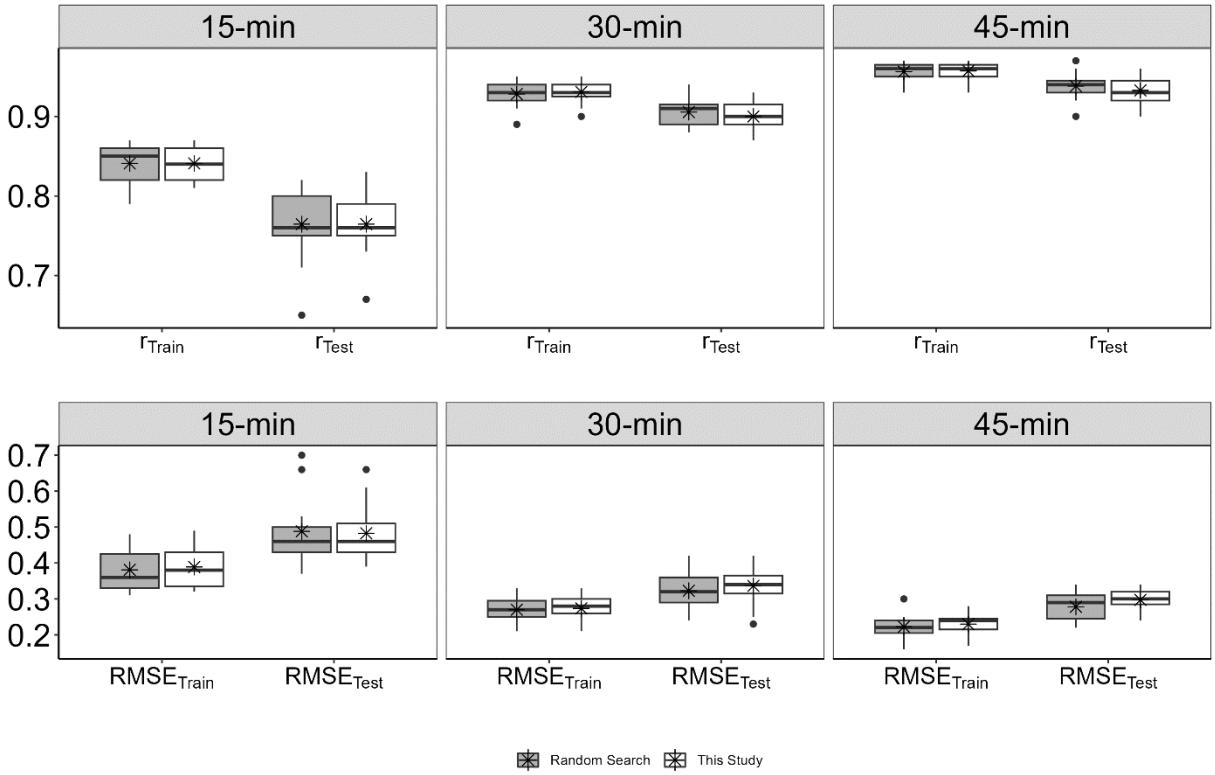

Fig. 5.3 Performance comparison of rainfall disaggregation using ANN with and without random search hyperparameter tuning method.

We also compared the performance for rainfall disaggregation of hourly to monthly maximum rainfall with and without (Takhellambam et al. 2023) hyperparameter tuning (Fig 5.3). The results from the training dataset showed an average coefficient of correlation (r) for all durations did not improve as compared to what is reported in Chapter-4. Whereas, the average coefficient of correlation (r) for all duration except 15-min in the testing dataset was greater than the r value reported in Chapter-4. We found that r values of disaggregated rainfall for each duration of 15-, 30-, and 45-min have values of 0.77, 0.91, and 0.94, respectively. The null hypothesis of no significant difference in rainfall disaggregation performance with and without hyperparameter tuning using paired t-test is accepted with p-values of 0.38 and 0.12, respectively, at a significance level of 5%.

5.4.2 Impact of Bias Correction on IDF Curves

There is an improvement in the developed rainfall IDF curves with bias correction compared to the non-bias-corrected rainfall datasets for each climate model (Fig 5.4). The range of historical extreme rainfall intensities for five climates models of CANESM, HADGEM, GFDL, MPIREG, and MPIWRF is 7 to 10, 8 to 13, 9 to 16, 10 to 20, 11 to 24, and 12 to 27 mm h^{-1} having a return period of 2-, 5-, 10-, 25-, 50-, and 100-yr, respectively. Bias correction significantly improved extreme rainfall events in all climate models at each recurrence period. The rate of increase in the IDF curves for all climate models ranges from 120 to 271%, 138 to 300%, 119 to 311%, 100 to 330%, 83 to 336%, and 78 to 342% at a return period of 2-, 5-, 10-, 25-, 50-, and 100-yr, respectively.

Rainfall intensity tends to increase with the return period. Higher return periods suggest a rarer, more extreme weather event, which would typically result in higher precipitation volumes. The results show that the effect of bias correction on rainfall amount is more pronounced for extreme

weather events and less pronounced for mild rainfall events. The Welch Two Sample t-test results confirmed that there is a statistically significant difference between bias-corrected and historical rainfall extremes, rejecting the null hypothesis of no significant change after bias correction with a p-value <0.05 at a significance level of 5%. This confirms the necessity for bias correction of rainfall datasets. Consistent results with improvement in rainfall after bias correction were also reported in Takhellambam et al., (2022b, 2022a) and Zhao et al. (2022). The low-intensity rainfalls with more wet days are associated with NA-CORDEX rainstorm datasets. Although the amount of annual rainfall remained the same, this had a significant impact on the number of wet days (Takhellambam et al., 2022a). One of the reasons why there is a low extreme rainfall value in historical climate models. In addition, each climate model has different mechanisms of initial and boundary conditions for generating rainfalls. Furthermore, for a given climate model value, there is a consistent difference in rainfall intensities between bias-corrected and historical datasets (Fig 5.4).

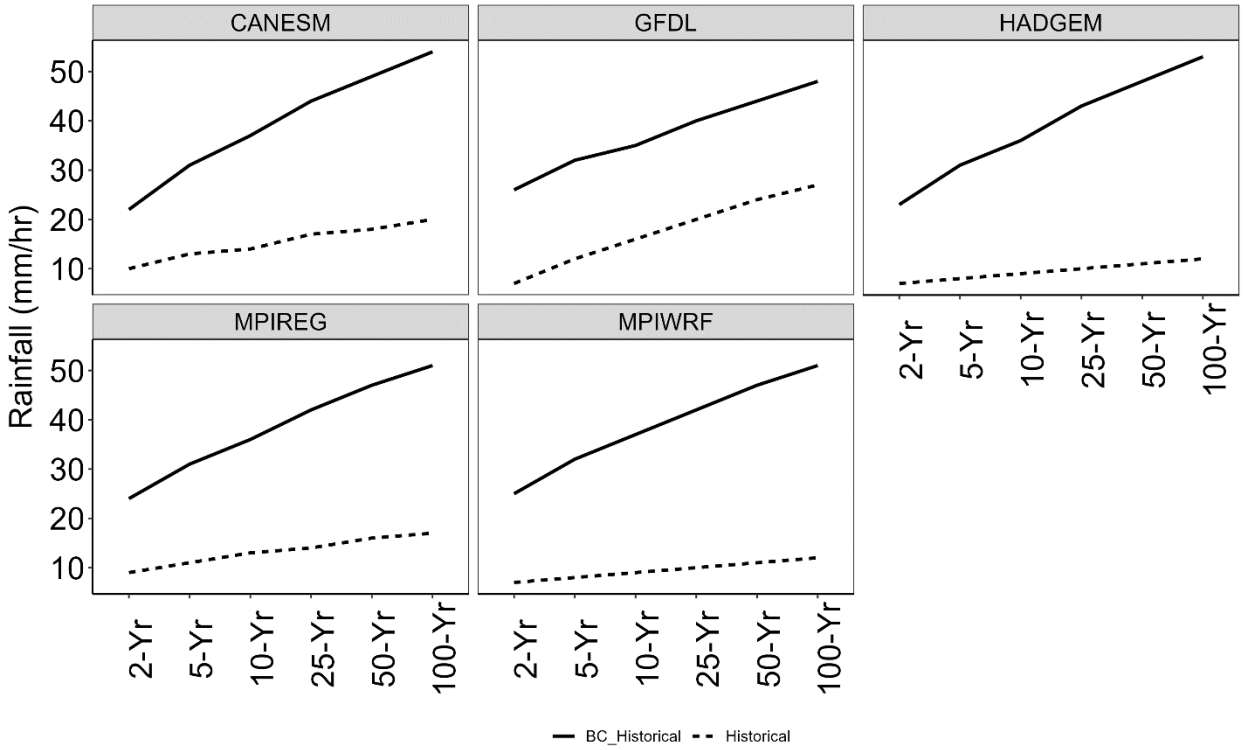

Fig. 5.4 Comparison between historical and bias-corrected historical IDF curves for Manning, Virginia.

5.4.3 Uncertainty quantification of IDF curves using bootstrapping

The relationship between the rainfall intensity, duration, and frequency is provided with the IDF curves for each duration and return period. Here, we reported the IDF curves obtained using the bootstrapping technique with resampling of 10,000 times for a randomly selected location in Manning, Virginia, with the CANESM model (Fig 5.5). This provides the confidence intervals of extreme rainfall intensities for durations of 15-, 30-, and 45-min having return period of 2-, 5-, 10-, 25-, 50-, and 100-year. Compared to the developed confidence interval at a 5% significance interval, these confidence intervals offer a superior depiction. One of the main reasons is the averaging of 10,000 samples of annual maximum rainfalls underestimated the extreme values. For instance, extreme rainfall intensities for 15-min, 2-yr return period using bootstrapping approach and confidence interval at the 5% significance level are found in the range of 56.6 to 56.7 mm h^{-1}

and 45 to 75 mm h^{-1}, respectively. Likewise, appendix D1.1-1.4 show the remaining IDF curves for the HADGEM, GFDL, MPIREG, and MPIWRF climate models. These large sample sizes of IDF curves ensure better and more reliable extreme rainfall values (Ng et al., 2019).

We found the rainfall intensities get reduced with increasing duration for all climate models and return periods (Fig 5.5). Because of averaging or smoothening, aggregated (30- and 45-min), rainfalls are underpredicted compared to 15-minute rainfalls (Op de Hipt et al., 2018; Takhellambam et al., 2023).

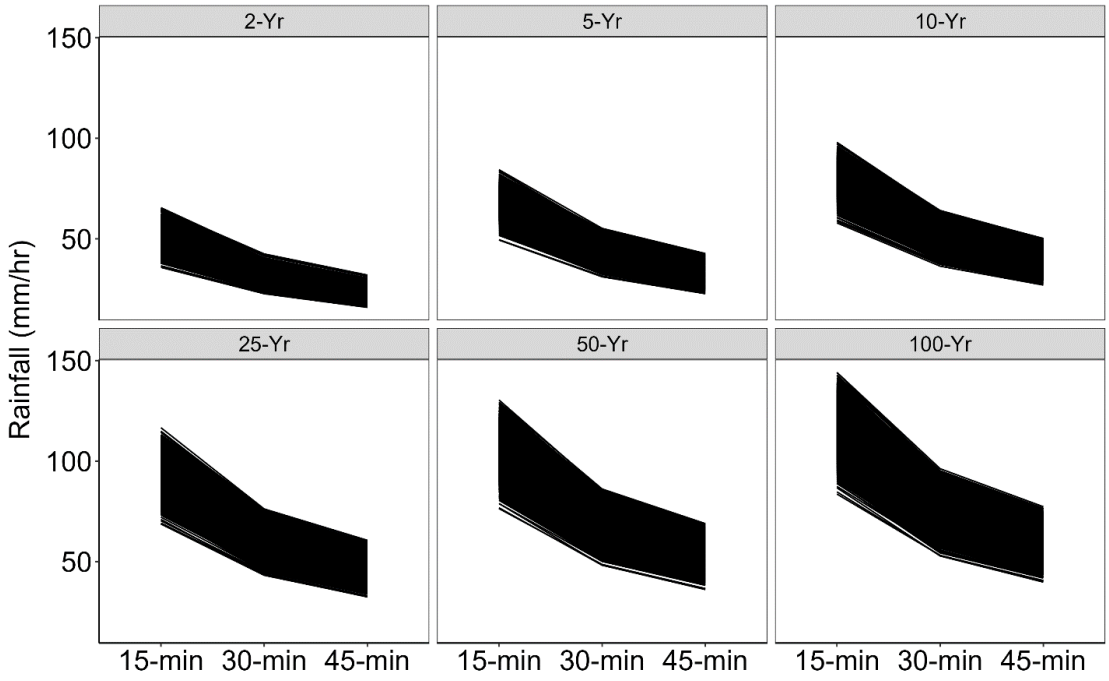

Fig. 5.5 Plot showing the rainfall Intensity-Duration-Frequency curves using the bootstrapping resampling technique of 10,000 times for the CANESM model located at Manning, Virginia.

Furthermore, we reported the ranges of annual extreme rainfall values of each duration of 15-, 30-, and 45-min for all return periods of 2-, 5-, 10-, 25-, 50-, and 100-yr under five climate models for the randomly selected station of Manning, Virginia (Fig 5.6). Appendix D2.1-2.10 show the remaining boxplots of 10 rainfall stations provided in Table 5.1. For brevity, we are discussing the IDF values for the station located in Manning, Virginia. Across all five climate models, the extreme

yearly rainfall intensities increase with longer return times and durations. For example, the yearly maximum rainfall intensity for the five models ranged from 69 to 94 mm h^{-1} for the 15-minute duration and 2-year return period and from 93 to 130 mm h^{-1} for the 45-minute duration and 100-year return period (Fig. 5.6).

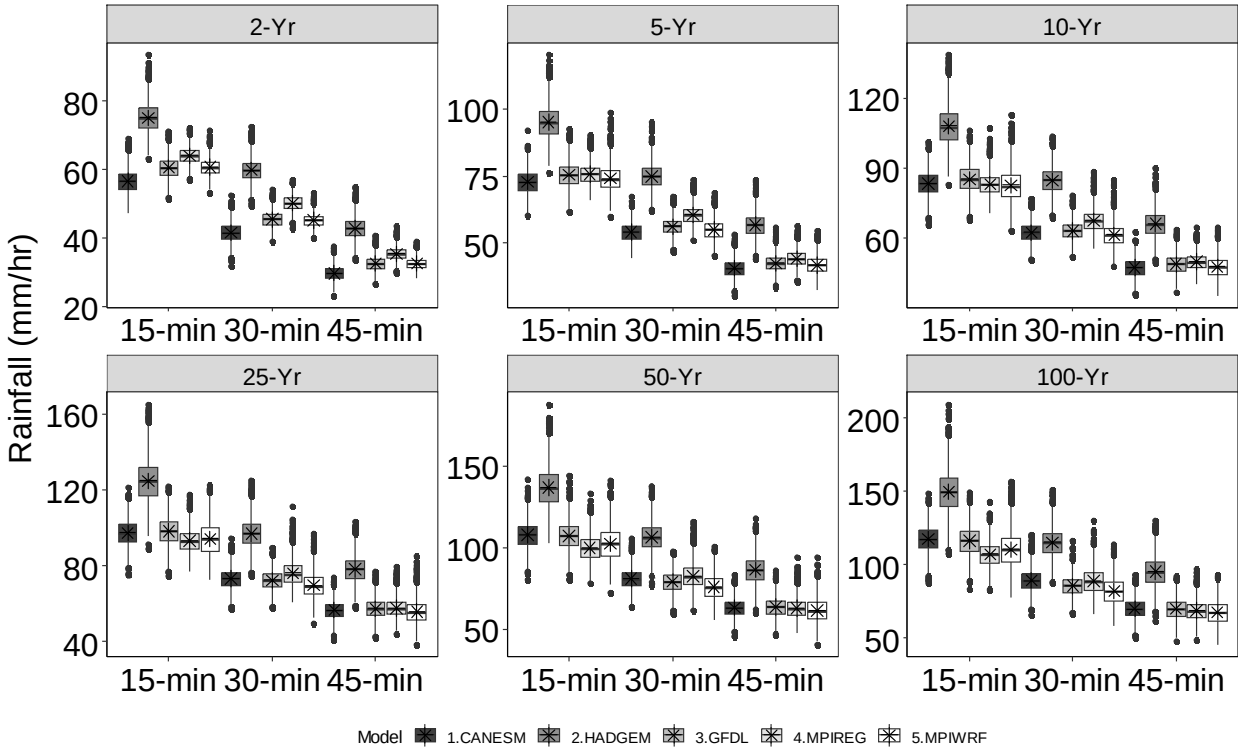

Fig. 5.6 Boxplots depicting the range of rainfall intensities for periods of 15-, 30-, and 45-min at return periods of 2-, 5-, 10-, 25-, 50-, and 100-Yr for all climate models at Manning, Virginia station. Asterisk denotes the average rainfall intensity.

In addition, we also found that each climate model recorded varied rainfall intensities for the same return period and duration. For example, five models' median precipitation values for the 15-minute duration and 2-year return period ranged from 57 to 75 mm h^{-1}. Similarly, the median precipitation values for the 30-minute duration and 50-year return period ranged from 76 to 106 mm. This demonstrates that each climate model has distinct mechanisms of rainfall generation, namely initial and boundary conditions (Mirhosseini et al., 2014). As a result, we employed

various climate models to quantify the uncertainty or ranges of extreme annual rainfall values to provide a more accurate picture of future projected extreme rainfall projections. Moreover, the HADGEM and MPIWRF models had the highest average and median rainfall intensities over all return periods and durations, indicating that these models may produce more conservative projections of extreme rainfall. Overall, the minimum and maximum annual maximum rainfall intensities were found in the range of 38 to 55 mm h^{-1} and 143 to 210 mm h^{-1}, respectively. The ensemble mean of all climate models of the annual maximum rainfall intensity at Manning, Virginia was found to range from 28 to 161 mm h^{-1} for each duration of all return periods (Table 5.4). Similarly, the ensemble mean of all climate models of the annual maximum rainfall intensity at the remaining stations is provided in Appendix D3. This ensemble result summarizes the inherent uncertainty associated with various climate models.

Table 5.4 Summary of annual maximum rainfall intensities (mm h^{-1}) with ensemble mean of five climate models at Manning, Virginia.

Duration	Return Period	Min	Median	Mean	Max
15-min	2-Yr	54	63	63	75
15-min	5-Yr	65	78	79	99
15-min	10-Yr	70	88	89	113
15-min	25-Yr	78	101	101	130
15-min	50-Yr	83	110	111	149
15-min	100-Yr	88	120	120	161
30-min	2-Yr	41	48	48	58
30-min	5-Yr	50	60	60	75
30-min	10-Yr	55	68	68	87
30-min	25-Yr	60	77	78	103
30-min	50-Yr	63	85	85	112
30-min	100-Yr	69	92	92	126
45-min	2-Yr	28	34	35	43
45-min	5-Yr	35	45	45	59
45-min	10-Yr	40	52	52	69
45-min	25-Yr	45	61	61	84
45-min	50-Yr	48	67	68	95
45-min	100-Yr	51	74	74	101

5.5 Conclusions

Climate impact studies are associated with various uncertainties that arise from the climate models, limited information, and a lack of understanding of physical processes. The quantification of uncertainties, particularly extreme rainfalls, helps decision-makers with climate change adaptation and mitigation strategies. Therefore, our study attempted to quantify the uncertainties associated with the updated rainfall IDF curves for the selected largest cities of each state of the southeast United States. Our findings showed that there are no significant differences while disaggregating hourly to sub-hourly monthly maximum rainfall with or without hyperparameter tuning of random search. This concludes that the hyperparameter tuning using random search does not have much substantial impact on the rainfall disaggregation performance. Furthermore, bias correction significantly improved the rainfall IDF curves by rejecting the null hypothesis of no difference with the Welch two sample t-test having a p-value <0.05 at a significance level of 5% and found the rate of change ranging from 78 to 342% in all return periods of 2-, 5-, 10-, 25-, 50-, and 100-yr. In addition, greater differences between bias and non-bias corrected rainfall datasets were observed with increased return periods. This advocated for bias correction for studies sensitive to rainfall intensity.

Bootstrapping resampling technique along with Gumbel distribution provided the future projected rainfall IDF curves for the sub-hourly (15-, 30-, and 45-min) duration with a return period of 2-, 5-, 10-, 25-, 50-, and 100-yr. We found that there is an increase in annual maximum rainfall intensities with longer return times and durations in all five climate models of CANESM, HADGEM, GFDL, MPIREG, and MPIWRF. Overall, the minimum and maximum annual maximum rainfall intensities were found in the range of 38 to 55 mm h^{-1} and 143 to 210 mm h^{-1}, respectively.

In conclusion, this study developed future projected rainfall IDF curves for large cities in the Southeast United States using the bootstrapping technique. This approach can be applied in other similar studies. However, further studies could improve quantifying the uncertainty associated with the generated IDF curves, such as human error in climate modeling which is often neglected, and uncertainty related to the randomness of natural processes.

CHAPTER 6

Summary and Future Work

6.1 Summary of this dissertation

Climate change is occurring mainly due to anthropogenic activities that are increasing the greenhouse gases in the atmosphere. This has resulted and is resulting in increasing temperature that has a major effect on water resources and the agriculture sector, particularly, due to changes in extreme rainfall characteristics. To tackle the effect of climate change, proper mitigation and adaptation measures are required using reliable datasets, particularly in the southeast United States, the region with the greatest projected change in rainfall characteristics. Therefore, this dissertation focused on quantifying the effects of climate change on rainfall characteristics over the southeastern United States. The key findings of the main four objectives are summarized as follows.

6.1.1 Temporal Disaggregation of Hourly Precipitation Under Changing Climate Over the Southeast United States

The modified stochastic method performed satisfactorily in disaggregating hourly rainfall to 15-min intervals. Disaggregated 15-min rainfall dataset provides an improvement over hourly observed dataset. One of the major limitations is that the generated precipitation characteristics might not sufficiently represent the observed precipitation characteristics.

6.1.2 Projected Mid-Century Rainfall Erosivity Under Climate Change Over the Southeastern United States

This study developed rainfall erosivity for the period 2030-2059 under RCP8.5 over the southeast United States using 15-min rainfall. The most significant findings are:

1. Under the RCP8.5 scenario, annual average precipitation, erosivity, and erosivity density in the Southeast are projected to increase by 14%, 47%, and 29%, respectively, for the period 2030-2059 over the historical baseline (1970-1999).
2. The historical and future ensemble model showed an average annual R-factor of 11237MJ mm $ha^{-1}h^{-1}yr^{-1}$ and 7665 MJ mm $ha^{-1}h^{-1}yr^{-1}$, respectively.
3. The southern part of Florida, the Appalachian region, and the coastal region of the Gulf of Mexico areas were predicted to experience the greatest absolute increase in erosivity while areas with lower baseline erosivities were generally predicted to see the largest relative changes.

6.1.3 Artificial Neural Network-Empowered Projected Future Rainfall Intensity-Duration-Frequency Curves under Changing Climate

This study improved the performance of a feed-forward and backpropagation ANN model for disaggregating hourly to sub-hourly (15-, 30-, and 45-min) monthly maximum rainfall datasets. ANN model showed better performance than the stochastic model for generating sub-hour monthly maximum rainfall with an average NSE ranging from 0.67 to 0.84. In addition, IDF curves were updated for various return periods using disaggregated datasets and found future extreme events are increasing at a rate of 7% to 36% as compared to the historical period. The mean extreme rainfall intensities range from 34 to 135 mm h^{-1} for a duration of 15-, 30-, and 45-min with a return period of 2-, 5-, 10-, 25-, 50-, and 100-year.

6.1.4 Quantifying Uncertainty in Projected Rainfall Intensity Duration Frequency Curves Using Artificial Neural Network and Bootstrapping Resampling Technique

This study quantified uncertainties associated with the projected IDF curves based on the non-stationarity of sub-hourly rainfall datasets. There were no significant differences while disaggregating hourly to sub-hourly rainfall monthly maximum rainfall with or without hyperparameter tuning of random search. Moreover, bias correction of rainfall significantly improved the rainfall IDF curves more than the non-bias corrected datasets. In addition, developed IDF curves (15-, 30-, and 45-min duration with a return period of 2-, 5-, 10-, 25-, 50-, and 100-yr) using the bootstrapping resampling technique found minimum and maximum values of annual maximum rainfall intensities in the range of 38 to 55 $\mathrm{mm\,h^{-1}}$ and 143 to 210 $\mathrm{mm\,h^{-1}}$, respectively.

6.2 Future Work

1. Bias correction and temporal disaggregation of hourly rainfall could be improved using data-driven approaches. Accuracy in existing approaches of both bias correction and temporal disaggregation, can be improved using state-of-the-art methods such as deep learning.
2. A robust methodology for estimating erosivity using aggregated rainfall datasets is needed. This is because limited rainfall data is available at higher temporal resolution.
3. Rainfall characteristics are significantly influenced by climate variability indices like the El Niño-Southern Oscillation (ENSO) and Pacific Decadal Oscillation (PDO). Therefore, it is necessary to quantify how these indices relate to rainfall erosivity.
4. The Sixth Phase of the Coupled Model Intercomparison Project (CMIP6) could provide different scenarios for rainfall erosivity and IDF curves.

References

Abbaspour, K.C., 2013. SWAT-CUP 2012. SWAT Calibration and uncertainty program—a user manual.

Abbaspour, K.C., Yang, J., Maximov, I., Siber, R., Bogner, K., Mieleitner, J., Zobrist, J., Srinivasan, R., 2007. Modelling hydrology and water quality in the pre-alpine/alpine Thur watershed using SWAT. Journal of Hydrology 333, 413–430. https://doi.org/10.1016/j.jhydrol.2006.09.014

Adams, R.M., Peck, D.E., 2008. Effects of Climate Change on Water Resources. Choices 23, 12–14.

Al Kajbaf, A., Bensi, M., Brubaker, K.L., 2023. Drivers of uncertainty in precipitation frequency under current and future climate – application to Maryland, USA. Journal of Hydrology 617, 128775. https://doi.org/10.1016/j.jhydrol.2022.128775

Allan, R.P., Soden, B.J., 2008. Atmospheric Warming and the Amplification of Precipitation Extremes. Science 321, 1481–1484. https://doi.org/10.1126/science.1160787

Almagro, A., Oliveira, P.T.S., Nearing, M.A., Hagemann, S., 2017. Projected climate change impacts in rainfall erosivity over Brazil. Scientific Reports 7, 8130. https://doi.org/10.1038/s41598-017-08298-y

Almazroui, M., Şen, Z., Mohorji, A.M., Islam, M.N., 2019. Impacts of Climate Change on Water Engineering Structures in Arid Regions: Case Studies in Turkey and Saudi Arabia. Earth Syst Environ 3, 43–57. https://doi.org/10.1007/s41748-018-0082-6

Amatya, D.M., Tian, S., Marion, D.A., Caldwell, P., Laseter, S., Youssef, M.A., Grace, J.M., Chescheir, G.M., Panda, S., Ouyang, Y., Sun, G., Vose, J.M., 2021. Estimates of Precipitation IDF Curves and Design Discharges for Road-Crossing Drainage Structures: Case Study in Four Small Forested Watersheds in the Southeastern US. Journal of Hydrologic Engineering 26, 05021004. https://doi.org/10.1061/(ASCE)HE.1943-5584.0002052

Amini, A., Dolatshahi, M., Kerachian, R., 2023. Effects of Automatic Hyperparameter Tuning on the Performance of Multi-Variate Deep Learning-Based Rainfall Nowcasting. Water Resources Research 59, e2022WR032789. https://doi.org/10.1029/2022WR032789

Ballabio, C., Borrelli, P., Spinoni, J., Meusburger, K., Michaelides, S., Beguería, S., Klik, A., Petan, S., Janeček, M., Olsen, P., Aalto, J., Lakatos, M., Rymszewicz, A., Dumitrescu, A., Tadić, M.P., Diodato, N., Kostalova, J., Rousseva, S., Banasik, K., Alewell, C., Panagos, P., 2017. Mapping monthly rainfall erosivity in Europe. Science of The Total Environment 579, 1298–1315. https://doi.org/10.1016/j.scitotenv.2016.11.123

Beguería, S., Serrano-Notivoli, R., Tomas-Burguera, M., 2018. Computation of rainfall erosivity from daily precipitation amounts. Science of The Total Environment 637–638, 359–373. https://doi.org/10.1016/j.scitotenv.2018.04.400

Bergstra, J., Bengio, Y., 2012. Random Search for Hyper-Parameter Optimization.

Biasutti, M., Seager, R., 2015. Projected changes in US rainfall erosivity. Hydrology and Earth System Sciences 19, 2945–2961. https://doi.org/10.5194/hess-19-2945-2015

Bonilla, C.A., Vidal, K.L., 2011. Rainfall erosivity in Central Chile. Journal of Hydrology 410, 126–133. https://doi.org/10.1016/j.jhydrol.2011.09.022

Borrelli, P., Alewell, C., Alvarez, P., Anache, J.A.A., Baartman, J., Ballabio, C., Bezak, N., Biddoccu, M., Cerdà, A., Chalise, D., Chen, S., Chen, W., De Girolamo, A.M., Gessesse, G.D., Deumlich, D., Diodato, N., Efthimiou, N., Erpul, G., Fiener, P., Freppaz, M., Gentile,

F., Gericke, A., Haregeweyn, N., Hu, B., Jeanneau, A., Kaffas, K., Kiani-Harchegani, M., Villuendas, I.L., Li, C., Lombardo, L., López-Vicente, M., Lucas-Borja, M.E., Märker, M., Matthews, F., Miao, C., Mikoš, M., Modugno, S., Möller, M., Naipal, V., Nearing, M., Owusu, S., Panday, D., Patault, E., Patriche, C.V., Poggio, L., Portes, R., Quijano, L., Rahdari, M.R., Renima, M., Ricci, G.F., Rodrigo-Comino, J., Saia, S., Samani, A.N., Schillaci, C., Syrris, V., Kim, H.S., Spinola, D.N., Oliveira, P.T., Teng, H., Thapa, R., Vantas, K., Vieira, D., Yang, J.E., Yin, S., Zema, D.A., Zhao, G., Panagos, P., 2021. Soil erosion modelling: A global review and statistical analysis. Science of The Total Environment 780, 146494. https://doi.org/10.1016/j.scitotenv.2021.146494

Borrelli, P., Robinson, D.A., Fleischer, L.R., Lugato, E., Ballabio, C., Alewell, C., Meusburger, K., Modugno, S., Schütt, B., Ferro, V., Bagarello, V., Oost, K.V., Montanarella, L., Panagos, P., 2017. An assessment of the global impact of 21st century land use change on soil erosion. Nature Communications 8, 2013. https://doi.org/10.1038/s41467-017-02142-7

Borrelli, P., Robinson, D.A., Panagos, P., Lugato, E., Yang, J.E., Alewell, C., Wuepper, D., Montanarella, L., Ballabio, C., 2020. Land use and climate change impacts on global soil erosion by water (2015-2070). Proceedings of the National Academy of Sciences 117, 21994–22001. https://doi.org/10.1073/pnas.2001403117

Brown, L., Foster, G., 1987. Storm erosivity using idealized intensity distributions, T. ASAE, 30, 379–386.

Burian, S.J., Durrans, S.R., 2002. Evaluation of an artificial neural network rainfall disaggregation model. Water Science and Technology 45, 99–104. https://doi.org/10.2166/wst.2002.0033

Burian, S.J., Durrans, S.R., Nix, S.J., Pitt, R.E., 2001. Training Artificial Neural Networks to Perform Rainfall Disaggregation. Journal of Hydrologic Engineering 6, 43–51. https://doi.org/10.1061/(ASCE)1084-0699(2001)6:1(43)

Cannon, A.J., Sobie, S.R., Murdock, T.Q., 2015. Bias Correction of GCM Precipitation by Quantile Mapping: How Well Do Methods Preserve Changes in Quantiles and Extremes? Journal of Climate 28, 6938–6959. https://doi.org/10.1175/JCLI-D-14-00754.1

Carter, L.M., Terando, A., Dow, K., Hiers, K., Kunkel, K.E., Lascurain, A., Marcy, D.C., Osland, M.J., Schramm, P.J., 2018. Chapter 19 : Southeast. Impacts, Risks, and Adaptation in the United States: The Fourth National Climate Assessment, Volume II. U.S. Global Change Research Program. https://doi.org/10.7930/NCA4.2018.CH19

Cerdà, A., Flanagan, D.C., le Bissonnais, Y., Boardman, J., 2009. Soil erosion and agriculture. Soil and Tillage Research 106, 107–108. https://doi.org/10.1016/j.still.2009.10.006

Chen, H., Sun, J., Lin, W., Xu, H., 2020. Comparison of CMIP6 and CMIP5 models in simulating climate extremes. Sci. Bull. 65, 1415–1418. https://doi.org/10.1016/j.scib.2020.05.015

Chen, Y., Duan, X., Zhang, G., Ding, M., Lu, S., 2022. Rainfall erosivity estimation over the Tibetan plateau based on high spatial-temporal resolution rainfall records. International Soil and Water Conservation Research. https://doi.org/10.1016/j.iswcr.2022.01.004

Cheng, L., AghaKouchak, A., 2014. Nonstationary Precipitation Intensity-Duration-Frequency Curves for Infrastructure Design in a Changing Climate. Sci Rep 4, 7093. https://doi.org/10.1038/srep07093

Choi, J., Socolofsky, S.A., Olivera, F., 2008. Hourly disaggregation of daily rainfall in Texas using measured hourly precipitation at other locations. Journal of Hydrologic Engineering 13, 476–487. https://doi.org/10.1061/(ASCE)1084-0699(2008)13:6(476)

Coles, S., 2001. An introduction to statistical modeling of extreme values, 1st ed. Springer London.

Cook, J., Oreskes, N., Doran, P.T., Anderegg, W.R.L., Verheggen, B., Maibach, E.W., Carlton, J.S., Lewandowsky, S., Skuce, A.G., Green, S.A., Nuccitelli, D., Jacobs, P., Richardson, M., Winkler, B., Painting, R., Rice, K., 2016. Consensus on consensus: a synthesis of consensus estimates on human-caused global warming. Environ. Res. Lett. 11, 048002. https://doi.org/10.1088/1748-9326/11/4/048002

Crévolin, V., Hassanzadeh, E., Bourdeau-Goulet, S.-C., 2023. Updating the intensity-duration-frequency curves in major Canadian cities under changing climate using CMIP5 and CMIP6 model projections. Sustainable Cities and Society 92, 104473. https://doi.org/10.1016/j.scs.2023.104473

Delignette-Muller, M.L., Dutang, C., 2015. fitdistrplus: An R Package for Fitting Distributions. Journal of Statistical Software 64, 1–34. https://doi.org/10.18637/jss.v064.i04

Dibike, Y.B., Coulibaly, P., 2006. Temporal neural networks for downscaling climate variability and extremes. Neural Networks, Earth Sciences and Environmental Applications of Computational Intelligence 19, 135–144. https://doi.org/10.1016/j.neunet.2006.01.003

Easterling, D.R., Arnold, J.R., Knutson, T., Kunkel, K.E., LeGrande, A.N., Leung, L.R., Vose, R.S., Waliser, D.E., Wehner, M.F., 2017. Ch. 7: Precipitation Change in the United States. Climate Science Special Report: Fourth National Climate Assessment, Volume I. U.S. Global Change Research Program. https://doi.org/10.7930/J0H993CC

Einfalt, T., Michaelides, S., 2008. Quality control of precipitation data, in: Michaelides, S. (Ed.), Precipitation: Advances in Measurement, Estimation and Prediction. Springer Berlin Heidelberg, Berlin, Heidelberg, pp. 101–126. https://doi.org/10.1007/978-3-540-77655-0_5

Emmanouil, S., Langousis, A., Nikolopoulos, E.I., Anagnostou, E.N., 2022. The Spatiotemporal Evolution of Rainfall Extremes in a Changing Climate: A CONUS-Wide Assessment Based on Multifractal Scaling Arguments. Earth's Future 10, e2021EF002539. https://doi.org/10.1029/2021EF002539

FAO, Clara, Ronald, 2019. Soil erosion: the greatest challenge for sustainable soil management. Rome.

Feng, G., Cobb, S., Abdo, Z., Fisher, D.K., Ouyang, Y., Adeli, A., Jenkins, J.N., 2016. Trend Analysis and Forecast of Precipitation, Reference Evapotranspiration, and Rainfall Deficit in the Blackland Prairie of Eastern Mississippi. Journal of Applied Meteorology and Climatology 55, 1425–1439. https://doi.org/10.1175/JAMC-D-15-0265.1

Fick, S.E., Hijmans, R.J., 2017. WorldClim 2: new 1-km spatial resolution climate surfaces for global land areas. International Journal of Climatology 37, 4302–4315. https://doi.org/10.1002/joc.5086

Fischer, F.K., Winterrath, T., Auerswald, K., 2018. Temporal- and spatial-scale and positional effects on rain erosivity derived from point-scale and contiguous rain data. Hydrology and Earth System Sciences 22, 6505–6518. https://doi.org/10.5194/hess-22-6505-2018

Flanagan, D.C., McGehee, R.P., Srivastava, A., 2020. Evaluation of Different Precipitation Inputs to WEPP, in: 2020 ASABE Annual International Virtual Meeting, July 13-15, 2020. Presented at the 2020 ASABE Annual International Virtual Meeting, July 13-15, 2020, American Society of Agricultural and Biological Engineers. https://doi.org/10.13031/aim.202000740

Fullhart, A.T., Nearing, M.A., McGehee, R.P., Weltz, M.A., 2020. Temporally downscaling a precipitation intensity factor for soil erosion modeling using the NOAA-ASOS weather station network. CATENA 194, 104709. https://doi.org/10.1016/j.catena.2020.104709

Ganguli, P., Coulibaly, P., 2019. Assessment of future changes in intensity-duration-frequency curves for Southern Ontario using North American (NA)-CORDEX models with nonstationary methods. Journal of Hydrology: Regional Studies 22, 100587. https://doi.org/10.1016/j.ejrh.2018.12.007

Gassman, P.W., Sadeghi, A.M., Srinivasan, R., 2014. Applications of the SWAT model special section: Overview and Insights. J Environ Qual 43, 1–8. https://doi.org/10.2134/jeq2013.11.0466

Ghasemi Tousi, E., O'Brien, W., Doulabian, S., Shadmehri Toosi, A., 2021. Climate changes impact on stormwater infrastructure design in Tucson Arizona. Sustainable Cities and Society 72, 103014. https://doi.org/10.1016/j.scs.2021.103014

Giorgi, F., Anyah, R.O., 2012. The road towards RegCM4. Climate Research 52, 3–6. https://doi.org/10.3354/cr01089

Giorgi, F., Elguindi, N., Cozzini, S., Giuliani, G., 2013. Regional climatic model RegCM user's guide version 4.4.

Greve, P., Orlowsky, B., Mueller, B., Sheffield, J., Reichstein, M., Seneviratne, S.I., 2014. Global assessment of trends in wetting and drying over land. Nature Geosci 7, 716–721. https://doi.org/10.1038/ngeo2247

Grillakis, M.G., Polykretis, C., Alexakis, D.D., 2020. Past and projected climate change impacts on rainfall erosivity: Advancing our knowledge for the eastern Mediterranean island of Crete. CATENA 193, 104625. https://doi.org/10.1016/j.catena.2020.104625

Gudmundsson, L., Bremnes, J.B., Haugen, J.E., Engen-Skaugen, T., 2012. Technical Note: Downscaling RCM precipitation to the station scale using statistical transformations- a comparison of methods. Hydrology and Earth System Sciences 16, 3383–3390. https://doi.org/10.5194/hess-16-3383-2012

Gutierrez-Magness, A.L., McCuen, R.H., 2004. Accuracy Evaluation of Rainfall Disaggregation Methods. Journal of Hydrologic Engineering 9, 71–78. https://doi.org/10.1061/(ASCE)1084-0699(2004)9:2(71)

Guttorp, P., 2012. Climate Statistics and Public Policy. Statistics, Politics, and Policy 3. https://doi.org/10.1515/2151-7509.1055

Hansen, J., Sato, M., Ruedy, R., Lo, K., Lea, D.W., Medina-Elizade, M., 2006. Global temperature change. Proceedings of the National Academy of Sciences 103, 14288–14293. https://doi.org/10.1073/pnas.0606291103

Hempel, S., Frieler, K., Warszawski, L., Schewe, J., Piontek, F., 2013. A trend-preserving bias correction – the ISI-MIP approach. Earth System Dynamics 4, 219–236. https://doi.org/10.5194/esd-4-219-2013

Herold, N., Alexander, L.V., Donat, M.G., Contractor, S., Becker, A., 2016. How much does it rain over land? Geophysical Research Letters 43, 341–348. https://doi.org/10.1002/2015GL066615

Hoegh-Guldberg, O., Jacob, D., Taylor, M., Bindi, M., Brown, S., Camilloni, I., Diedhiou, A., Djalante, R., Ebi, K.L., Engelbrecht, F., Hijioka, Y., Mehrotra, S., Payne, A., Seneviratne, S.I., Thomas, A., Warren, R., Zhou, G., Halim, S.A., Achlatis, M., Allen, R., Berry, P., Boyer, C., Brilli, L., Byers, E., Cheung, W., Craig, M., Ellis, N., Evans, J., Fischer, H., Fraedrich, K., Fuss, S., Ganase, A., Gattuso, J.-P., Bolaños, T.G., Hanasaki, N., Hayes, K., Hirsch, A., Jones, C., Jung, T., Kanninen, M., Krinner, G., Lawrence, D., Ley, D., Liverman, D., Mahowald, N., Meissner, K.J., Millar, R., Mintenbeck, K., Mix, A.C., Notz, D., Nurse, L., Okem, A., Olsson, L., Oppenheimer, M., Paz, S., Petersen, J., Petzold, J.,

Preuschmann, S., Rahman, M.F., Scheuffele, H., Schleussner, C.-F., Séférian, R., Sillmann, J., Singh, C., Slade, R., Stephenson, K., Stephenson, T., Tebboth, M., Tschakert, P., Vautard, R., Wehner, M., Weyer, N.M., Whyte, F., Yohe, G., Zhang, X., Zougmoré, R.B., Marengo, J.A., Pereira, J., Sherstyukov, B., 2018. Impacts of 1.5°C of Global Warming on Natural and Human Systems 138.

Hollinger, S.E., Angel, J.R., Palecki, M.A., 2002. Spatial Distribution, Variation, and Trends in Storm Precipitation Characteristics Associated with Soil Erosion in the United States (No. ISWS Contract Report CR-2002-08). Illinois State Water Survey Circular.

Hoomehr, S., Schwartz, J.S., Yoder, D.C., 2016. Potential changes in rainfall erosivity under GCM climate change scenarios for the southern Appalachian region, USA. CATENA, Section 1 : Special issue on Reclamation of mining site soils, Part I; Edited by: Jaume Bech. and Section 2 : Special Issue on Understanding hydrological and erosion processes under changing environment; Edited by: Lei, T W, Yu, X X, Zhuang, J. 136, 141–151. https://doi.org/10.1016/j.catena.2015.01.012

Ingram, K., Dow, K., Carter, L., Anderson, J., 2013. Climate of the southeast united states: Variability, change, impacts, and vulnerability. Island Press, Washington DC.

IPCC, 2018. Global Warming of 1.5°C: An IPCC Special Report on the impacts of global warming of 1.5°C above pre-industrial levels and related global greenhouse gas emission pathways, in the context of strengthening the global response to the threat of climate change, sustainable development, and efforts to eradicate poverty. Cambridge University Press, Cambridge, UK and New York, NY, USA. https://doi.org/10.1017/9781009157940

IPCC, 2007. Climate Change 2007: The Physical Science Basis. Contribution of Working Group I to the Fourth Assessment Report of the Intergovernmental Panel on Climate Change. Cambridge University Press, Cambridge, United Kingdom and New York, NY, USA.

Islam, S., Entekhabi, D., Bras, R.L., Rodriguez-Iturbe, I., 1990. Parameter estimation and sensitivity analysis for the modified Bartlett-Lewis rectangular pulses model of rainfall. Journal of Geophysical Research: Atmospheres 95, 2093–2100. https://doi.org/10.1029/JD095iD03p02093

Jeong, J., Kannan, N., Arnold, J., Glick, R., Gosselink, L., Srinivasan, R., 2010. Development and integration of sub-hourly rainfall–runoff modeling capability within a watershed model. Water Resour Manage 24, 4505–4527. https://doi.org/10.1007/s11269-010-9670-4

Kamruzzaman, M., Shahid, S., Islam, A.T., Hwang, S., Cho, J., Zaman, Md.A.U., Ahmed, M., Rahman, Md.M., Hossain, Md.B., 2021. Comparison of CMIP6 and CMIP5 model performance in simulating historical precipitation and temperature in Bangladesh: a preliminary study. Theor Appl Climatol 145, 1385–1406. https://doi.org/10.1007/s00704-021-03691-0

Karl, T.R., Knight, R.W., Easterling, D.R., Quayle, R.G., 1996. Indices of Climate Change for the United States. Bull. Amer. Meteor. Soc. 77, 279–292. https://doi.org/10.1175/1520-0477(1996)077<0279:IOCCFT>2.0.CO;2

Katz, R.W., Craigmile, P.F., Guttorp, P., Haran, M., Sansó, B., Stein, M.L., 2013. Uncertainty analysis in climate change assessments. Nature Clim Change 3, 769–771. https://doi.org/10.1038/nclimate1980

Keim, B.D., Fontenot, R., Tebaldi, C., Shankman, D., 2011. Hydroclimatology of the U.S. Gulf Coast Under Global Climate Change Scenarios. Physical Geography 32, 561–582. https://doi.org/10.2747/0272-3646.32.6.561

Kim, J., Han, H., Kim, B., Chen, H., Lee, J.-H., 2020. Use of a high-resolution-satellite-based precipitation product in mapping continental-scale rainfall erosivity: A case study of the United States. CATENA 193, 104602. https://doi.org/10.1016/j.catena.2020.104602

Kinnell, P.I.A., 2010. Event soil loss, runoff and the Universal Soil Loss Equation family of models: A review. Journal of Hydrology 385, 384–397. https://doi.org/10.1016/j.jhydrol.2010.01.024

Kitoh, A., Endo, H., 2016. Future Changes in Rainfall Extremes Associated with El Niño Projected by a Global 20-km Mesh Atmospheric Model. Sola 12A, 1–6. https://doi.org/10.2151/sola.12A-001

Knight, D.B., Davis, R.E., 2007. Climatology of Tropical Cyclone Rainfall in the Southeastern United States. Physical Geography 28, 126–147. https://doi.org/10.2747/0272-3646.28.2.126

Konapala, G., Mishra, A.K., Wada, Y., Mann, M.E., 2020. Climate change will affect global water availability through compounding changes in seasonal precipitation and evaporation. Nat Commun 11, 3044. https://doi.org/10.1038/s41467-020-16757-w

Kossieris, P., Makropoulos, C., Onof, C., Koutsoyiannis, D., 2018. A rainfall disaggregation scheme for sub-hourly time scales: Coupling a Bartlett-Lewis based model with adjusting procedures. Journal of Hydrology 556, 980–992. https://doi.org/10.1016/j.jhydrol.2016.07.015

Kumar, H., Srivastava, P., Lamba, J., Diamantopoulos, E., Ortiz, B., Morata, G., Takhellambam, B., Bondesan, L., 2022a. Site-specific irrigation scheduling using one-layer soil hydraulic properties and inverse modeling. Agricultural Water Management 273, 107877. https://doi.org/10.1016/j.agwat.2022.107877

Kumar, H., Srivastava, P., Lamba, J., Lena, B., Diamantopoulos, E., Ortiz, B., Takhellambam, B., Morata, G., Bondesan, L., 2023. A methodology to optimize site-specific field capacity and irrigation thresholds. Agricultural Water Management 286, 108385. https://doi.org/10.1016/j.agwat.2023.108385

Kumar, H., Srivastava, P., Lamba, J., Ortiz, B.V., Way, T.R., Sangha, L., Takhellambam, B.S., Morata, G., Molinari, R., 2022b. Within-Field Variability in Nutrients for Site-Specific Agricultural Management in Irrigated Cornfield. Journal of the ASABE 65, 865–880. https://doi.org/10.13031/ja.15042

Kumar, H., Srivastava, P., Ortiz, B.V., Morata, G., Takhellambam, B.S., Lamba, J., Bondesan, L., 2021. Field-Scale spatial and temporal Soil water variability in irrigated Croplands. Transactions of the ASABE 64, 1277–1294. https://doi.org/10.13031/trans.14335

Kunkel, K.E., Stevens, L.E., Stevens, S.E., Sun, L., Janssen, E., Wuebbles, D., Ii, C.E.K., Fuhrman, C.M., Keim, B.D., Kruk, M.C., Billet, A., Needham, H., Schafer, M., Dobson, J.G., 2013. Regional Climate Trends and Scenarios for the U.S. National Climate Assessment (No. NESDIS 142-2). National Oceanic and Atmospheric Administration, National Oceanic and Atmospheric Administration.

Lewis, E., Pritchard, D., Villalobos-Herrera, R., Blenkinsop, S., McClean, F., Guerreiro, S., Schneider, U., Becker, A., Finger, P., Meyer-Christoffer, A., Rustemeier, E., Fowler, H.J., 2021. Quality control of a global hourly rainfall dataset. Environmental Modelling & Software 144, 105169. https://doi.org/10.1016/j.envsoft.2021.105169

Li, H., Sheffield, J., Wood, E.F., 2010. Bias correction of monthly precipitation and temperature fields from Intergovernmental Panel on Climate Change AR4 models using equidistant

quantile matching. Journal of Geophysical Research: Atmospheres 115. https://doi.org/10.1029/2009JD012882

Li, J., Huo, R., Chen, H., Zhao, Y., Zhao, T., 2021. Comparative Assessment and Future Prediction Using CMIP6 and CMIP5 for Annual Precipitation and Extreme Precipitation Simulation. Frontiers in Earth Science 9.

Li, X., Meshgi, A., Wang, X., Zhang, J., Tay, S.H.X., Pijcke, G., Manocha, N., Ong, M., Nguyen, M.T., Babovic, V., 2018. Three resampling approaches based on method of fragments for daily-to-subdaily precipitation disaggregation. International Journal of Climatology 38, e1119–e1138. https://doi.org/10.1002/joc.5438

Lilliefors, H.W., 1967. On the Kolmogorov-Smirnov Test for Normality with Mean and Variance Unknown. Journal of the American Statistical Association 62, 399–402. https://doi.org/10.2307/2283970

Lopez-Cantu, T., Prein, A.F., Samaras, C., 2020. Uncertainties in Future U.S. Extreme Precipitation From Downscaled Climate Projections. Geophysical Research Letters 47, e2019GL086797. https://doi.org/10.1029/2019GL086797

Mahdi, S., Cenac, M., 2005. Estimating parameters of Gumbel Distribution using the Methods of Moments, probability weighted moments and maximum likelihood. Revista de Matemática: Teoría y Aplicaciones 12, 151–156. https://doi.org/10.15517/rmta.v12i1-2.259

Martel, J.-L., Brissette, F., Troin, M., Arsenault, R., Chen, J., Su, T., Lucas-Picher, P., 2022. CMIP5 and CMIP6 Model Projection Comparison for Hydrological Impacts Over North America. Geophysical Research Letters 49, e2022GL098364. https://doi.org/10.1029/2022GL098364

McGehee, R., 2016. Development of Reliable Erosion Indices for Climate-Informed Soil Conservation in the Southeastern United States. Auburn University.

McGehee, R., Srivastava, P., 2018. Benchmarking reliable erosion indices from quarter-hour station data for climate studies in the southeastern United States. Journal of Soil and Water Conservation 73, 363–376. https://doi.org/10.2489/jswc.73.4.363

McGehee, R.P., Flanagan, D.C., Srivastava, P., 2020. WEPPCLIFF: A command-line tool to process climate inputs for soil loss models. Journal of Open Source Software 5, 2029.

McGehee, R.P., Flanagan, D.C., Srivastava, P., Engel, B.A., Huang, C.-H., Nearing, M.A., 2022. An updated isoerodent map of the conterminous United States. International Soil and Water Conservation Research 10, 1–16. https://doi.org/10.1016/j.iswcr.2021.06.004

McGehee, R.P., Flanagan, D.C., Srivastava, P., Nearing, M.A., 2021. Chapter 16 - Rainfall erosivity: essential historical, conceptual, and practical perspectives for continued application, in: Rodrigo-Comino, J. (Ed.), Precipitation. Elsevier, pp. 373–394. https://doi.org/10.1016/B978-0-12-822699-5.00014-8

McGregor, K., Mutchler, C., 1976. Status of the R factor in northern Mississippi. Soil erosion: prediction and control 135–142.

McGregor, K.C., Bingner, R.L., Bowie, A.J., Foster, G.R., 1995. Erosivity index values for Northern Mississippi. Transactions of the ASAE 38, 1039–1047. https://doi.org/10.13031/2013.27921

McGregor, K.C., Mutchler, C.K., Browie, A.J., 1980. Annual R values in north Mississippi. Journal of Soil and Water Conservation 35(2):81-84.

Mearns, L., McGinnis, S., Korytina, D., Arritt, R., Biner, S., Bukovsky, M., Chang, H.-I., Christensen, O., Herzmann, D., Jiao, Y., Kharin, S., Lazare, M., Nikulin, G., Qian, M.,

Scinocca, J., Winger, K., Castro, C., Frigon, A., Gutowski, W., 2017. The NA-CORDEX dataset. https://doi.org/10.5065/D6SJ1JCH

Mearns, L.O., Gutowski, W., Jones, R., Leung, R., McGinnis, S., Nunes, A., Qian, Y., 2009. A Regional Climate Change Assessment Program for North America. Eos, Transactions American Geophysical Union 90, 311–311. https://doi.org/10.1029/2009EO360002

Mendes, J., Maia, R., 2020. Spatial downscaling of 3-hourly precipitation forecast data at river basin scale. Meteorol Atmos Phys 132, 143–158. https://doi.org/10.1007/s00703-019-00678-5

Meusburger, K., Steel, A., Panagos, P., Montanarella, L., Alewell, C., 2012. Spatial and temporal variability of rainfall erosivity factor for Switzerland. Hydrology and Earth System Sciences 16, 167–177. https://doi.org/10.5194/hess-16-167-2012

Meyer, J.D.D., Wang, S.-Y.S., Gillies, R.R., Yoon, J.-H., 2021. Evaluating NA-CORDEX historical performance and future change of western U.S. precipitation patterns and modes of variability. International Journal of Climatology 41, 4509–4532. https://doi.org/10.1002/joc.7083

Mirhosseini, G., Srivastava, P., Fang, X., 2014. Developing Rainfall Intensity-Duration-Frequency Curves for Alabama under Future Climate Scenarios Using Artificial Neural Networks. Journal of Hydrologic Engineering 19, 04014022. https://doi.org/10.1061/(ASCE)HE.1943-5584.0000962

Mirhosseini, G., Srivastava, P., Sharifi, A., 2015. Developing Probability-Based IDF Curves Using Kernel Density Estimator. Journal of Hydrologic Engineering 20, 04015002. https://doi.org/10.1061/(ASCE)HE.1943-5584.0001160

Mirhosseini, G., Srivastava, P., Stefanova, L., 2013. The impact of climate change on rainfall Intensity–Duration–Frequency (IDF) curves in Alabama. Reg Environ Change 13, 25–33. https://doi.org/10.1007/s10113-012-0375-5

Mishra, V., Bhatia, U., Tiwari, A.D., 2020. Bias-corrected climate projections for South Asia from Coupled Model Intercomparison Project-6. Sci Data 7, 338. https://doi.org/10.1038/s41597-020-00681-1

Mondal, A., Khare, D., Kundu, S., 2016. Change in rainfall erosivity in the past and future due to climate change in the central part of India. International Soil and Water Conservation Research 4, 186–194. https://doi.org/10.1016/j.iswcr.2016.08.004

Moriasi, D.N., G. Arnold, J., W. Van Liew, M., L. Bingner, R., D. Harmel, R., L. Veith, T., 2007. Model Evaluation Guidelines for Systematic Quantification of Accuracy in Watershed Simulations. Transactions of the ASABE 50, 885–900. https://doi.org/10.13031/2013.23153

Naipal, V., Ciais, P., Wang, Y., Lauerwald, R., Guenet, B., Oost, K.V., 2018. Global soil organic carbon removal by water erosion under climate change and land use change during AD 1850–2005. Biogeosciences 15, 4459–4480. https://doi.org/10.5194/bg-15-4459-2018

Nearing, M.A., 2001. Potential changes in rainfall erosivity in the U.S. with climate change during the 21st century. Journal of Soil and Water Conservation 56, 229–232.

Nearing, M.A., Yin, S., Borrelli, P., Polyakov, V.O., 2017. Rainfall erosivity: An historical review. CATENA 157, 357–362. https://doi.org/10.1016/j.catena.2017.06.004

Nerantzaki, S.D., Papalexiou, S.M., 2022. Assessing extremes in hydroclimatology: A review on probabilistic methods. Journal of Hydrology 605, 127302. https://doi.org/10.1016/j.jhydrol.2021.127302

Ng, J.L., Abd Aziz, S., Huang, Y.F., Mirzaei, M., Wayayok, A., Rowshon, M.K., 2019. Uncertainty analysis of rainfall depth duration frequency curves using the bootstrap resampling technique. J Earth Syst Sci 128, 113. https://doi.org/10.1007/s12040-019-1154-1

NOAA NCEI (National Oceanic and Atmospheric Administration, National Centers for Environmental Information), 2014. US 15 Minute Precipitation Data, Version 1.0. 1970-2010.

Noor, M., Ismail, T., Shahid, S., Asaduzzaman, Md., Dewan, A., 2022. Projection of rainfall intensity-duration-frequency curves at ungauged location under climate change scenarios. Sustainable Cities and Society 83, 103951. https://doi.org/10.1016/j.scs.2022.103951

Nyssen, J., Vandenreyken, H., Poesen, J., Moeyersons, J., Deckers, J., Haile, M., Salles, C., Govers, G., 2005. Rainfall erosivity and variability in the Northern Ethiopian Highlands. Journal of Hydrology 311, 172–187. https://doi.org/10.1016/j.jhydrol.2004.12.016

Oliveira, P.T.S., Wendland, E., Nearing, M.A., 2013. Rainfall erosivity in Brazil: A review. CATENA 100, 139–147. https://doi.org/10.1016/j.catena.2012.08.006

O'Neal, M.R., Nearing, M.A., Vining, R.C., Southworth, J., Pfeifer, R.A., 2005. Climate change impacts on soil erosion in Midwest United States with changes in crop management. CATENA, Soil Erosion under Climate Change: Rates, Implications and Feedbacks 61, 165–184. https://doi.org/10.1016/j.catena.2005.03.003

Op de Hipt, F., Diekkrüger, B., Steup, G., Yira, Y., Hoffmann, T., Rode, M., 2018. Modeling the impact of climate change on water resources and soil erosion in a tropical catchment in Burkina Faso, West Africa. CATENA 163, 63–77. https://doi.org/10.1016/j.catena.2017.11.023

Oreskes, N., 2004. The Scientific Consensus on Climate Change. Science 306, 1686–1686. https://doi.org/10.1126/science.1103618

Pampaloni, M., Sordo-Ward, A., Bianucci, P., Gabriel-Martin, I., Caporali, E., Garrote, L., 2021. A Stochastic Procedure for Temporal Disaggregation of Daily Rainfall Data in SuDS Design. Water 13, 403. https://doi.org/10.3390/w13040403

Panagos, P., Ballabio, C., Borrelli, P., Meusburger, K., Klik, A., Rousseva, S., Tadić, M.P., Michaelides, S., Hrabalíková, M., Olsen, P., Aalto, J., Lakatos, M., Rymszewicz, A., Dumitrescu, A., Beguería, S., Alewell, C., 2015. Rainfall erosivity in Europe. Science of The Total Environment 511, 801–814. https://doi.org/10.1016/j.scitotenv.2015.01.008

Panagos, P., Borrelli, P., Matthews, F., Liakos, L., Bezak, N., Diodato, N., Ballabio, C., 2022. Global rainfall erosivity projections for 2050 and 2070. Journal of Hydrology 610, 127865. https://doi.org/10.1016/j.jhydrol.2022.127865

Panagos, P., Borrelli, P., Meusburger, K., Yu, B., Klik, A., Jae Lim, K., Yang, J.E., Ni, J., Miao, C., Chattopadhyay, N., Sadeghi, S.H., Hazbavi, Z., Zabihi, M., Larionov, G.A., Krasnov, S.F., Gorobets, A.V., Levi, Y., Erpul, G., Birkel, C., Hoyos, N., Naipal, V., Oliveira, P.T.S., Bonilla, C.A., Meddi, M., Nel, W., Al Dashti, H., Boni, M., Diodato, N., Van Oost, K., Nearing, M., Ballabio, C., 2017. Global rainfall erosivity assessment based on high-temporal resolution rainfall records. Scientific Reports 7, 4175. https://doi.org/10.1038/s41598-017-04282-8

Perica, S., Martin, D., Pavlovic, S., Roy, I., St Laurent, M., Trypaluk, C., Unruh, D., Yekta, M., Bonnin, G., 2013. Precipitation-Frequency Atlas of the United States (No. Volume 9 Version 2.0: Southeastern States (Alabama, Arkansas, Florida, Georgia, Louisiana, Mississippi)). NOAA, National Weather Service, Silver Spring, MD.

Phien, H.N., 1987. A review of methods of parameter estimation for the extreme value type-1 distribution. Journal of Hydrology 90, 251–268. https://doi.org/10.1016/0022-1694(87)90070-9

Pimentel, D., 2006. Soil Erosion: A Food and Environmental Threat. Environ Dev Sustain 8, 119–137. https://doi.org/10.1007/s10668-005-1262-8

Prein, A.F., Rasmussen, R.M., Ikeda, K., Liu, C., Clark, M.P., Holland, G.J., 2017. The future intensification of hourly precipitation extremes. Nature Clim Change 7, 48–52. https://doi.org/10.1038/nclimate3168

Pruski, F.F., Nearing, M.A., 2002. Climate-induced changes in erosion during the 21st century for eight U.S. locations. Water Resources Research 38, 34-1-34–11. https://doi.org/10.1029/2001WR000493

Ramirez-Villegas, J., Challinor, A.J., Thornton, P.K., Jarvis, A., 2013. Implications of regional improvement in global climate models for agricultural impact research. Environ. Res. Lett. 8, 024018. https://doi.org/10.1088/1748-9326/8/2/024018

Renard, K.G., 1997. Predicting soil erosion by water: a guide to conservation planning with the Revised Universal Soil Loss Equation (RUSLE). United States Government Printing.

Renard, K.G., Freimund, J.R., 1994. Using monthly precipitation data to estimate the R-factor in the revised USLE. Journal of Hydrology 157, 287–306. https://doi.org/10.1016/0022-1694(94)90110-4

Riquetti, N.B., Mello, C.R., Beskow, S., Viola, M.R., 2020. Rainfall erosivity in South America: Current patterns and future perspectives. Science of The Total Environment 724, 138315. https://doi.org/10.1016/j.scitotenv.2020.138315

Rodda, J.C., 1967. The rainfall measurement problem. IAHS Publication No 78, 215–231.

Rodda, J.C., Dixon, H., 2012. Rainfall measurement revisited. Weather 67, 131–136. https://doi.org/10.1002/wea.875

Rodriguez-Iturbe, I., Cox, D.R., Isham, V., 1988. A point process model for rainfall: further developments. Proceedings of the Royal Society of London. A. Mathematical and Physical Sciences 417, 283–298. https://doi.org/10.1098/rspa.1988.0061

Rodriguez-Iturbe, I., Cox, D.R., Isham, V., 1987. Some models for rainfall based on stochastic point processes. Proceedings of the Royal Society of London. A. Mathematical and Physical Sciences 410, 269–288. https://doi.org/10.1098/rspa.1987.0039

Sarhadi, A., Soulis, E.D., 2017. Time-varying extreme rainfall intensity-duration-frequency curves in a changing climate. Geophysical Research Letters 44, 2454–2463. https://doi.org/10.1002/2016GL072201

Savina, M., Schäppi, B., Molnar, P., Burlando, P., Sevruk, B., 2012. Comparison of a tipping-bucket and electronic weighing precipitation gage for snowfall. Atmospheric Research, Rainfall in the urban context: forecasting, risk and climate change 103, 45–51. https://doi.org/10.1016/j.atmosres.2011.06.010

Schuol, J., Abbaspour, K.C., 2006. Calibration and uncertainty issues of a hydrological model (SWAT) applied to West Africa. Advances in Geosciences 9, 137–143. https://doi.org/10.5194/adgeo-9-137-2006

Scinocca, J.F., Kharin, V.V., Jiao, Y., Qian, M.W., Lazare, M., Solheim, L., Flato, G.M., Biner, S., Desgagne, M., Dugas, B., 2016. Coordinated Global and Regional Climate Modeling. Journal of Climate 29, 17–35. https://doi.org/10.1175/JCLI-D-15-0161.1

Seager, R., Tzanova, A., Nakamura, J., 2009. Drought in the Southeastern United States: Causes, Variability over the Last Millennium, and the Potential for Future Hydroclimate Change. J. Climate 22, 5021–5045. https://doi.org/10.1175/2009JCLI2683.1

Segura, C., Sun, G., McNulty, S., Zhang, Y., 2014. Potential impacts of climate change on soil erosion vulnerability across the conterminous United States. Journal of Soil and Water Conservation 69, 171–181. https://doi.org/10.2489/jswc.69.2.171

Sharma, D., Das Gupta, A., Babel, M.S., 2007. Spatial disaggregation of bias-corrected GCM precipitation for improved hydrologic simulation: Ping River Basin, Thailand. Hydrology and Earth System Sciences Discussions 11, 1373–1390.

Shiono, T., Ogawa, S., Miyamoto, T., Kameyama, K., 2013. Expected impacts of climate change on rainfall erosivity of farmlands in Japan. Ecological Engineering, Soil Bio- and Eco-Engineering: The Use of Vegetation to Improve Slope Stability 61, 678–689. https://doi.org/10.1016/j.ecoleng.2013.03.002

Singh, J., Knapp, H.Vernon., Arnold, J. g., Demissie, M., 2005. Hydrological Modeling of the Iroquois River Watershed Using Hspf and Swat. JAWRA Journal of the American Water Resources Association 41, 343–360. https://doi.org/10.1111/j.1752-1688.2005.tb03740.x

Skamarock, W., Klemp, J., Dudhia, J., Gill, D., Barker, D., Wang, W., 2005. A Description of the Advanced Research WRF Version 2. UCAR/NCAR. https://doi.org/10.5065/D6DZ069T

Smitha, P.S., Narasimhan, B., Sudheer, K.P., Annamalai, H., 2018. An improved bias correction method of daily rainfall data using a sliding window technique for climate change impact assessment. Journal of Hydrology 556, 100–118. https://doi.org/10.1016/j.jhydrol.2017.11.010

Socolofsky, S., Adams, E.E., Entekhabi, D., 2001. Disaggregation of daily rainfall for continuous watershed modeling. Journal of Hydrologic Engineering 6, 300–309. https://doi.org/10.1061/(ASCE)1084-0699(2001)6:4(300)

Solaiman, T., 2011. Uncertainty Estimation of Extreme Precipitations Under Climate Change: A Non-Parametric Approach. Electronic Thesis and Dissertation Repository.

Soltani, S., Almasi, P., Helfi, R., Modarres, R., Mohit Esfahani, P., Ghadami Dehno, M., 2020. A new approach to explore climate change impact on rainfall intensity–duration–frequency curves. Theor Appl Climatol 142, 911–928. https://doi.org/10.1007/s00704-020-03309-x

Song, Y., Han, D., Rico-Ramirez, M.A., 2016. High temporal resolution rainfall information retrieval from tipping-bucket rain gauge measurements. Procedia Engineering, 12th International Conference on Hydroinformatics (HIC 2016) - Smart Water for the Future 154, 1193–1200. https://doi.org/10.1016/j.proeng.2016.07.525

Srivastav, R.K., Schardong, A., Simonovic, S.P., 2014. Equidistance Quantile Matching Method for Updating IDFCurves under Climate Change. Water Resour Manage 28, 2539–2562. https://doi.org/10.1007/s11269-014-0626-y

Sun, Y., Wendi, D., Kim, D.E., Liong, S.-Y., 2019. Deriving intensity–duration–frequency (IDF) curves using downscaled in situ rainfall assimilated with remote sensing data. Geosci. Lett. 6, 17. https://doi.org/10.1186/s40562-019-0147-x

Supari, Tangang, F., Juneng, L., Cruz, F., Chung, J.X., Ngai, S.T., Salimun, E., Mohd, M.S.F., Santisirisomboon, J., Singhruck, P., PhanVan, T., Ngo-Duc, T., Narisma, G., Aldrian, E., Gunawan, D., Sopaheluwakan, A., 2020. Multi-model projections of precipitation extremes in Southeast Asia based on CORDEX-Southeast Asia simulations. Environmental Research 184, 109350. https://doi.org/10.1016/j.envres.2020.109350

Swain, S., Hayhoe, K., 2015. CMIP5 projected changes in spring and summer drought and wet conditions over North America. Clim Dyn 44, 2737–2750. https://doi.org/10.1007/s00382-014-2255-9

Takhellambam, B.S., 2016. Flood discharge estimation only using at-site stage information. India Institute of Technology Roorkee, India.

Takhellambam, B.S., Srivastava, P., Lamba, J., McGehee, R.P., Kumar, H., Tian, D., 2023. Projected mid-century rainfall erosivity under climate change over the southeastern United States. Science of The Total Environment 865, 161119. https://doi.org/10.1016/j.scitotenv.2022.161119

Takhellambam, B.S., Srivastava, P., Lamba, J., McGehee, R.P., Kumar, H., Tian, D., 2022a. Temporal disaggregation of hourly precipitation under changing climate over the Southeast United States. Sci Data 9, 211. https://doi.org/10.1038/s41597-022-01304-7

Takhellambam, B.S., Srivastava, P., Lamba, J., McGehee, R.P., Kumar, H., Tian, D., 2022b. Projected Rainfall Erosivity Under Climate Change in the Southeastern United States, in: ASABE Paper No. 2200176. Presented at the 2022 ASABE Annual International Meeting, ASABE, St. Joseph, MI, p. 1. https://doi.org/10.13031/aim.202200176

Takhellambam, B.S., Srivastava, P., Lamba, J., Zhao, W., Kumar, H., Tian, D., 2022c. Assessment of projected change in Intensity-duration-frequency (IDF) curves for Southeastern, United States using Artificial Neural Networks., in: ASABE Paper No. 2200175. Presented at the 2022 ASABE Annual International Meeting, ASABE, St. Joseph, MI, p. 1. https://doi.org/10.13031/aim.202200175

Taylor, K.E., 2001. Summarizing multiple aspects of model performance in a single diagram. Journal of Geophysical Research: Atmospheres 106, 7183–7192. https://doi.org/10.1029/2000JD900719

Teutschbein, C., Seibert, J., 2012. Bias correction of regional climate model simulations for hydrological climate-change impact studies: Review and evaluation of different methods. Journal of Hydrology 456–457, 12–29. https://doi.org/10.1016/j.jhydrol.2012.05.052

Trenberth, K.E., 2011. Changes in precipitation with climate change. Climate Research 47, 123–138. https://doi.org/10.3354/cr00953

Trenberth, K.E., Dai, A., Rasmussen, R.M., Parsons, D.B., 2003. The Changing Character of Precipitation. Bull. Amer. Meteor. Soc. 84, 1205–1218. https://doi.org/10.1175/BAMS-84-9-1205

Trenberth, K.E., Zhang, Y., Gehne, M., 2017. Intermittency in Precipitation: Duration, Frequency, Intensity, and Amounts Using Hourly Data. Journal of Hydrometeorology 18, 1393–1412. https://doi.org/10.1175/JHM-D-16-0263.1

Tuo, Y., Duan, Z., Disse, M., Chiogna, G., 2016. Evaluation of precipitation input for SWAT modeling in Alpine catchment: A case study in the Adige river basin (Italy). Science of The Total Environment 573, 66–82. https://doi.org/10.1016/j.scitotenv.2016.08.034

USDA-ARS, 2013. Science Documentation Revised Universal Soil Loss Equation Version 2. US Department of Agriculture, Washington, DC.

USDA-ARS, 2008. User's Reference Guide: Revised Universal Soil Loss Equation (RUSLE2). US Department of Agriculture, Washington, DC.

USGCRP, 2018. Impacts, Risks, and Adaptation in the United States: Fourth National Climate Assessment [WWW Document]. URL https://nca2018.globalchange.gov/chapter/19 (accessed 2.23.21).

van Vuuren, D.P., Riahi, K., 2011. The relationship between short-term emissions and long-term concentration targets. Climatic Change 104, 793–801. https://doi.org/10.1007/s10584-010-0004-6

Velasquez, P., Messmer, M., Raible, C.C., 2020. A new bias-correction method for precipitation over complex terrain suitable for different climate states: a case study using WRF (version 3.8.1). Geoscientific Model Development 13, 5007–5027. https://doi.org/10.5194/gmd-13-5007-2020

Vizy, E.K., Cook, K.H., 2012. Mid-Twenty-First-Century Changes in Extreme Events over Northern and Tropical Africa. Journal of Climate 25, 5748–5767. https://doi.org/10.1175/JCLI-D-11-00693.1

Vu, T.M., Mishra, A.K., 2019. Nonstationary frequency analysis of the recent extreme precipitation events in the United States. Journal of Hydrology 575, 999–1010. https://doi.org/10.1016/j.jhydrol.2019.05.090

Wang, X., Zhang, J., Shahid, S., Guan, E., Wu, Y., Gao, J., He, R., 2016. Adaptation to climate change impacts on water demand. Mitig Adapt Strateg Glob Change 21, 81–99. https://doi.org/10.1007/s11027-014-9571-6

Webb, N.P., Van Zee, J.W., Karl, J.W., Herrick, J.E., Courtright, E.M., Billings, B.J., Boyd, R., Chappell, A., Duniway, M.C., Derner, J.D., Hand, J.L., Kachergis, E., McCord, S.E., Newingham, B.A., Pierson, F.B., Steiner, J.L., Tatarko, J., Tedela, N.H., Toledo, D., Scott Van Pelt, R., 2017. Enhancing Wind Erosion Monitoring and Assessment for U.S. Rangelands. Rangelands 39, 85–96. https://doi.org/10.1016/j.rala.2017.04.001

Willmott, C.J., 1982. Some Comments on the Evaluation of Model Performance. Bulletin American Meteorological Society 63, 5.

Wischmeier, W.H., Smith, D.D., 1978. Predicting Rainfall Erosion Losses: A Guide to Conservation Planning. Department of Agriculture, Science and Education Administration.

Wischmeier, W.H., Smith, D.D., 1965. Predicting rainfall-erosion losses from cropland east of the Rocky Mountains (No. USDA Agricultural Handbook No. 282). Washington, DC: USDA.

Wischmeier, W.H., Smith, D.D., 1958. Rainfall energy and its relationship to soil loss. Trans. AGU 39, 285. https://doi.org/10.1029/TR039i002p00285

Wood, A.W., Leung, L.R., Sridhar, V., Lettenmaier, D.P., 2004. Hydrologic Implications of Dynamical and Statistical Approaches to Downscaling Climate Model Outputs. Climatic Change 62, 189–216. https://doi.org/10.1023/B:CLIM.0000013685.99609.9e

Yan, H., Sun, N., Wigmosta, M., Skaggs, R., Hou, Z., Leung, R., 2018. Next-Generation Intensity-Duration-Frequency Curves for Hydrologic Design in Snow-Dominated Environments. Water Resources Research 54, 1093–1108. https://doi.org/10.1002/2017WR021290

Yang, X., Wood, E.F., Sheffield, J., Ren, L., Zhang, M., Wang, Y., 2018. Bias Correction of Historical and Future Simulations of Precipitation and Temperature for China from CMIP5 Models. Journal of Hydrometeorology 19, 609–623. https://doi.org/10.1175/JHM-D-17-0180.1

Zhang, Y.-G., Nearing, M.A., Zhang, X.C., Xie, Y., Wei, H., 2010. Projected rainfall erosivity changes under climate change from multimodel and multiscenario projections in Northeast China. Journal of Hydrology 384, 97–106. https://doi.org/10.1016/j.jhydrol.2010.01.013

Zhao, W., Abhishek, Kinouchi, T., 2022a. Uncertainty quantification in intensity-duration-frequency curves under climate change: Implications for flood-prone tropical cities. Atmospheric Research 270, 106070. https://doi.org/10.1016/j.atmosres.2022.106070

Zhao, W., Abhishek, Kinouchi, T., Ang, R., Zhuang, Q., 2022b. A framework for quantifying climate-informed heavy rainfall change: Implications for adaptation strategies. Science of The Total Environment 835, 155553. https://doi.org/10.1016/j.scitotenv.2022.155553

Zhao, W., Abhishek, Takhellambam, B.S., Zhang, J., Zhao, Y., Kinouchi, T., 2023. Spatiotemporal Variability of Current and Future Sub-Daily Rainfall in Japan Using State-Of-The-Art High-Quality Data Sets. Water Resources Research 59, e2022WR034305. https://doi.org/10.1029/2022WR034305

Zhao, W., Kinouchi, T., Nguyen, H.Q., 2021. A framework for projecting future intensity-duration-frequency (IDF) curves based on CORDEX Southeast Asia multi-model simulations: An application for two cities in Southern Vietnam. Journal of Hydrology 598, 126461. https://doi.org/10.1016/j.jhydrol.2021.126461

Zhu, D., Xiong, K., Xiao, H., 2021. Multi-time scale variability of rainfall erosivity and erosivity density in the karst region of southern China, 1960–2017. CATENA 197, 104977. https://doi.org/10.1016/j.catena.2020.104977

Zhu, J., 2013. Impact of Climate Change on Extreme Rainfall across the United States. Journal of Hydrologic Engineering 18, 1301–1309. https://doi.org/10.1061/(ASCE)HE.1943-5584.0000725

Zhu, J., Stone, M.C., Forsee, W., 2012. Analysis of potential impacts of climate change on intensity–duration–frequency (IDF) relationships for six regions in the United States. Journal of Water and Climate Change 3, 185–196. https://doi.org/10.2166/wcc.2012.045

Appendix A1

Annual wet-hour frequency and annual average precipitation for all stations under different climate models between H60 and bias-corrected precipitation

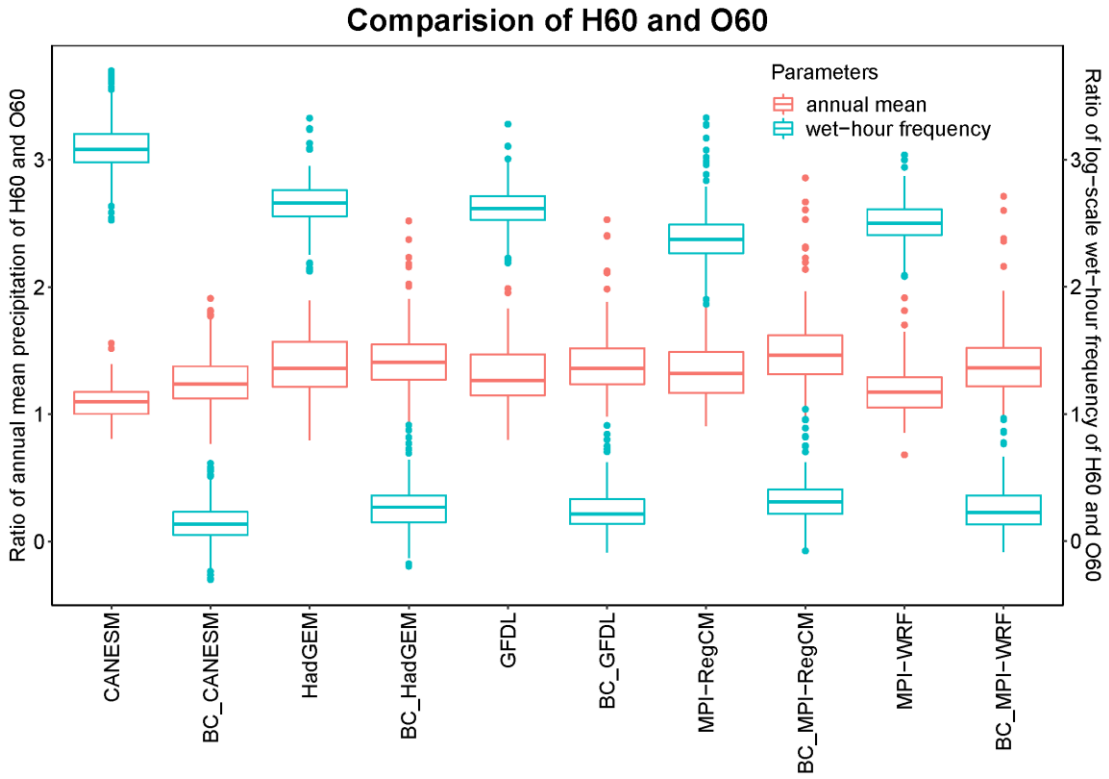

Note: BC before the names of climate models indicate "bias-corrected". In addition, Appendix A2-A4 omitted for 1988-01-10 01:00:00 under GFDL due to large value (outlier).

Appendix A2

Coefficient of determination between H60 and bias-corrected precipitation intensities for all station under different climate models

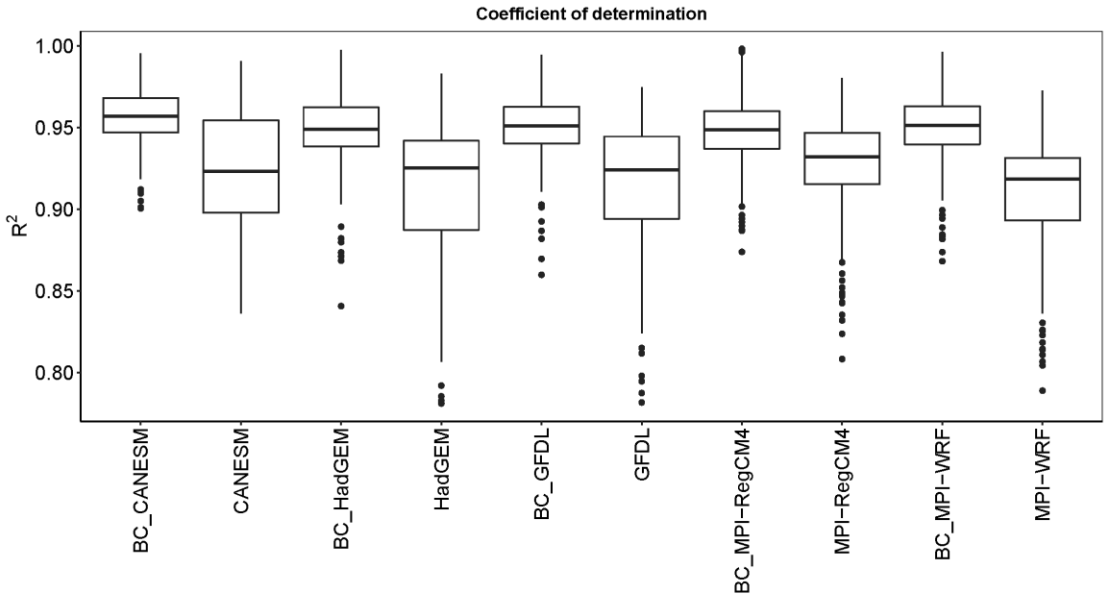

Appendix A3

RMSE of hourly precipitation intensity between H60 and bias-corrected precipitation for all stations under various climate models

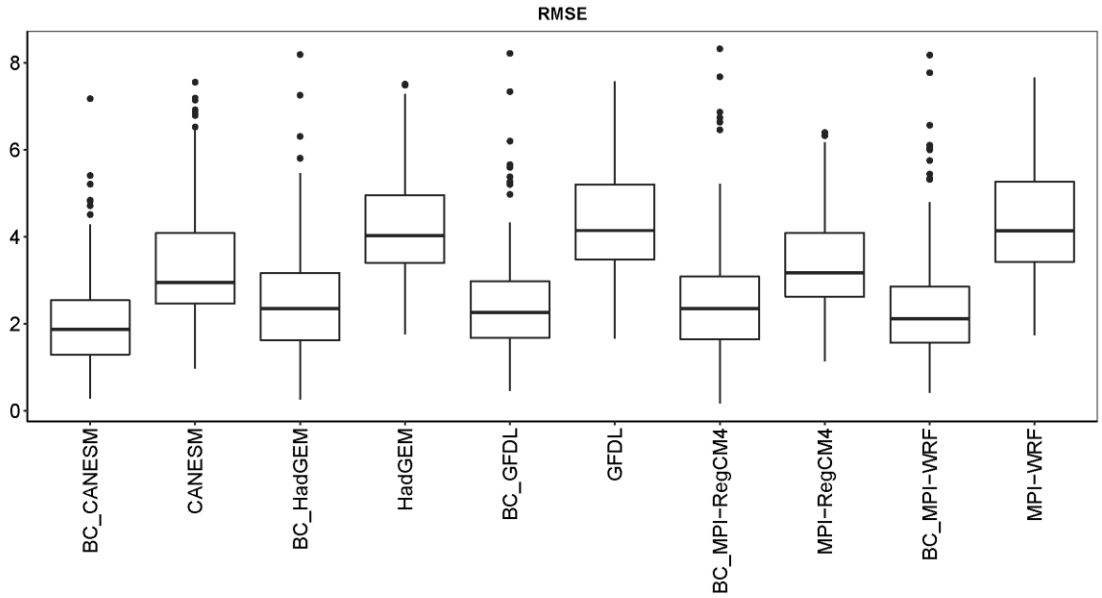

Appendix A4

Standard deviation of hourly precipitation intensity between H60 and bias-corrected precipitation for all stations under various climate models

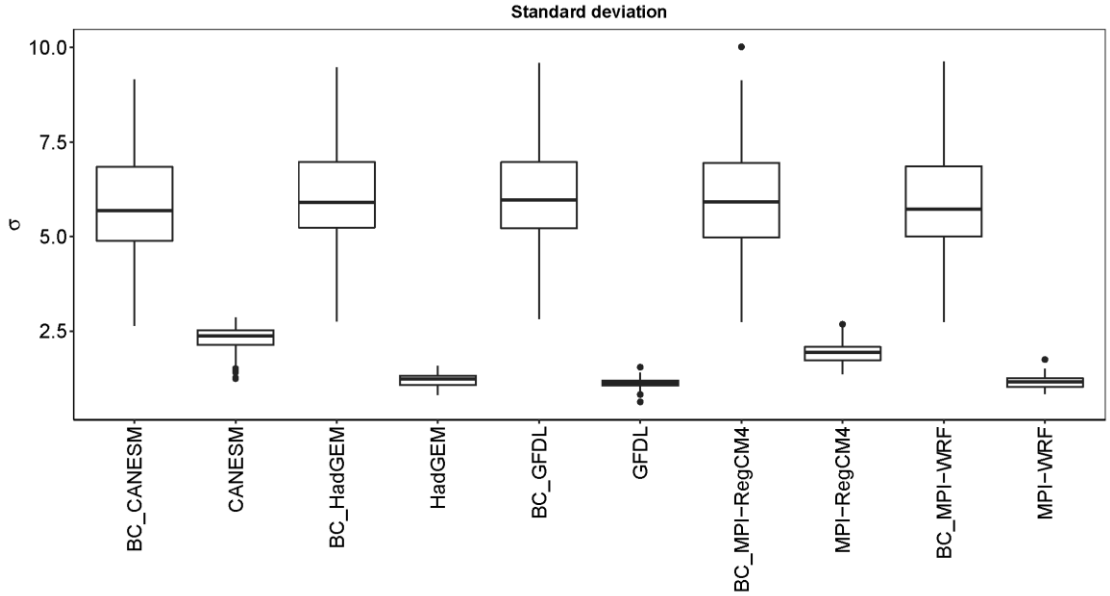

Appendix B1

Comparison of rainfall erosivity using high-temporal resolution and aggregated rainfall datasets

EI methods	Advantage	Disadvantage
a) EI using hourly/daily/monthly data	Aggregated (daily or hourly) rainfall data are widely available as compared to the high-temporal resolution data (15-min). Therefore, they are used in many countries, especially in developing countries.	Underestimation of EI due to smoothing of intensities.
b) EI using 15-min data	The intensities are comparably better than coarser data as peak intensities occurred in the first 15 minutes of a storm event. Therefore, it improves the erosivity estimation.	Availability of high temporal rainfall data is limited especially for future scenarios e.g., sub-hourly rainfall data. Moreover, the available rainfall characteristics may not be the same as the observed rainfall datasets.

Appendix C1

Maps showing the spatial variation of rainfall depth for 15-, 30-, and 45-min with a return period of 25-, 50-, and 100-year

C1.1. HADGEM

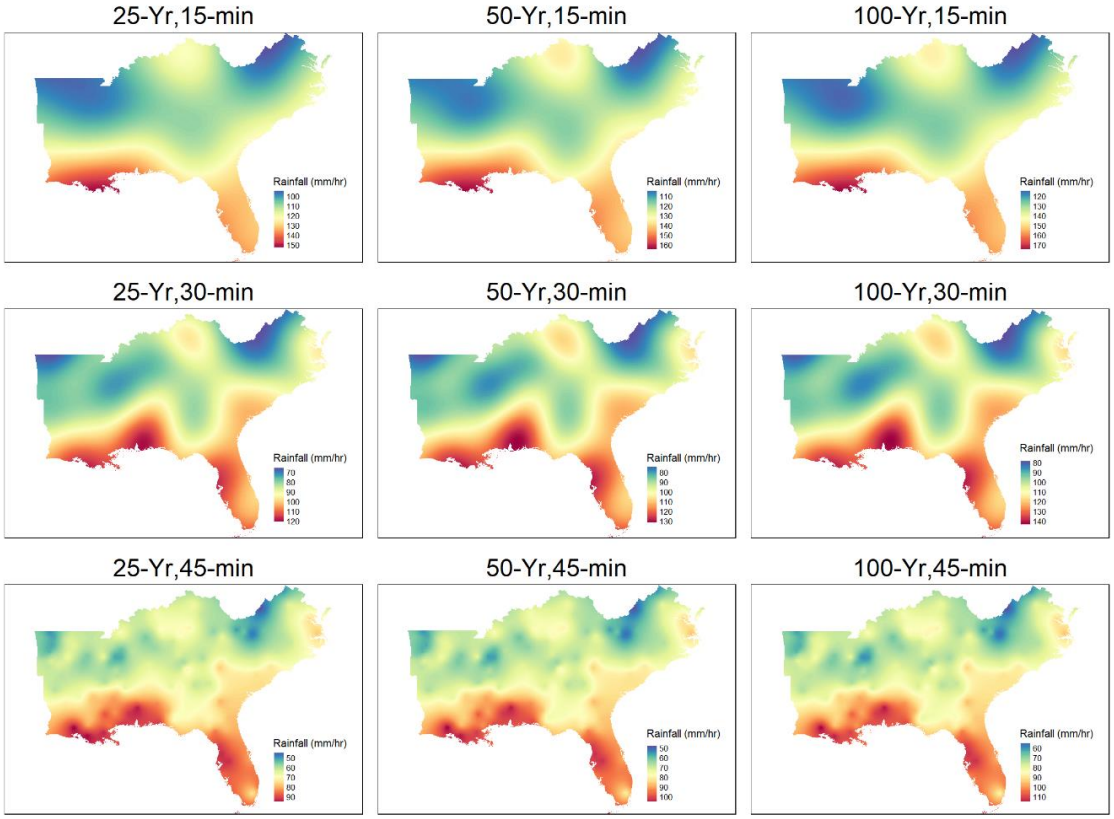

C1.2. GFDL

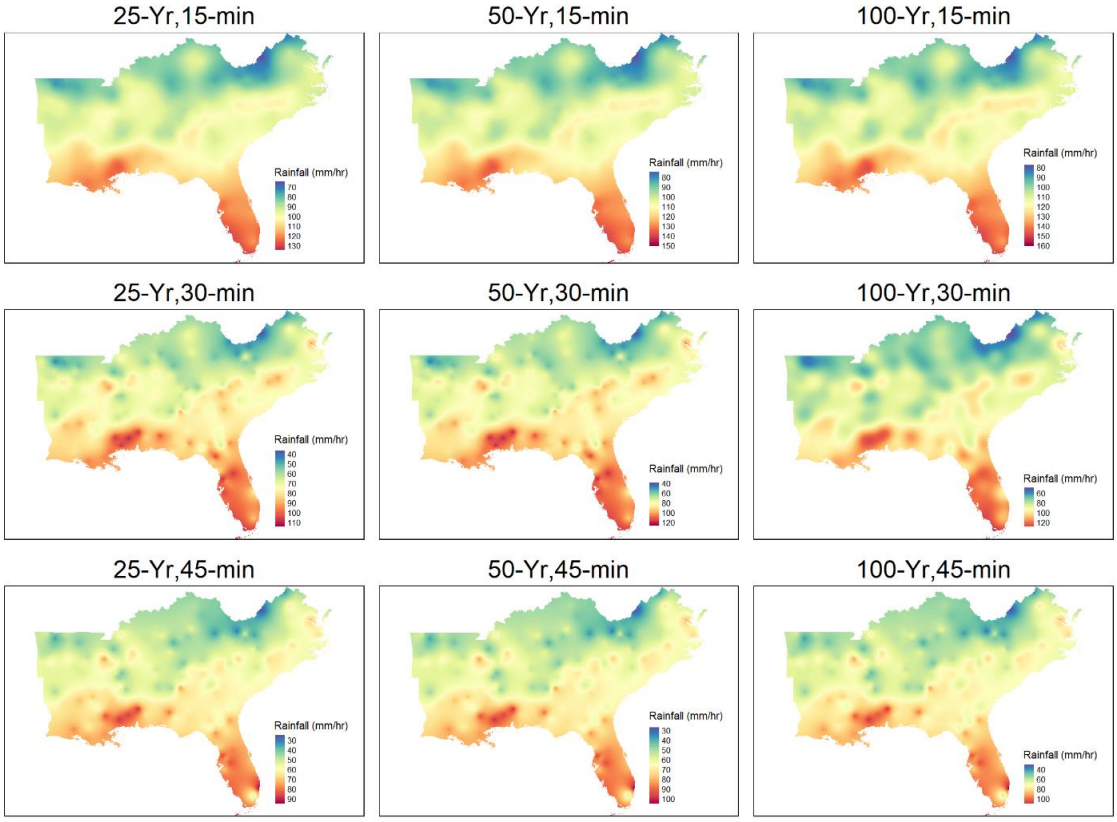
25-Yr,15-min
Rainfall (mm/hr)
70 80 90 100 110 120 130
50-Yr,15-min
Rainfall (mm/hr)
80 90 100 110 120 130 140 150
100-Yr,15-min
Rainfall (mm/hr)
80 90 100 110 120 130 140 150 160
25-Yr,30-min
Rainfall (mm/hr)
40 50 60 70 80 90 100 110
50-Yr,30-min
Rainfall (mm/hr)
40 60 80 100 120
100-Yr,30-min
Rainfall (mm/hr)
60 80 100 120
25-Yr,45-min
Rainfall (mm/hr)
30 40 50 60 70 80 90
50-Yr,45-min
Rainfall (mm/hr)
30 40 50 60 70 80 90 100
100-Yr,45-min
Rainfall (mm/hr)
40 60 80 100

C1.3. MPIREG

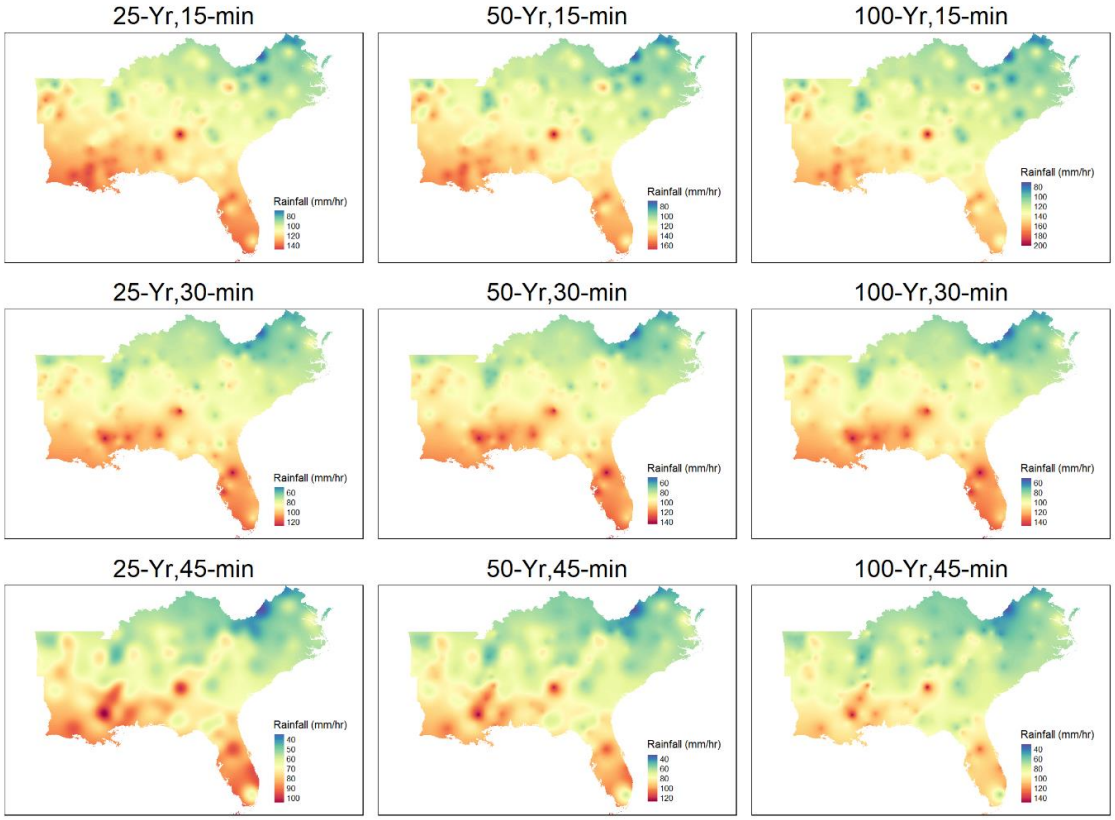
25-Yr,15-min
Rainfall (mm/hr)
80
100
120
140
50-Yr,15-min
Rainfall (mm/hr)
80
100
120
140
160
100-Yr,15-min
Rainfall (mm/hr)
80
100
120
140
160
180
200
25-Yr,30-min
Rainfall (mm/hr)
60
80
100
120
50-Yr,30-min
Rainfall (mm/hr)
60
80
100
120
140
100-Yr,30-min
Rainfall (mm/hr)
60
80
100
120
140
25-Yr,45-min
Rainfall (mm/hr)
40
50
60
70
80
90
100
50-Yr,45-min
Rainfall (mm/hr)
40
60
80
100
120
100-Yr,45-min
Rainfall (mm/hr)
40
60
80
100
120
140

C1.4. MPIWRF

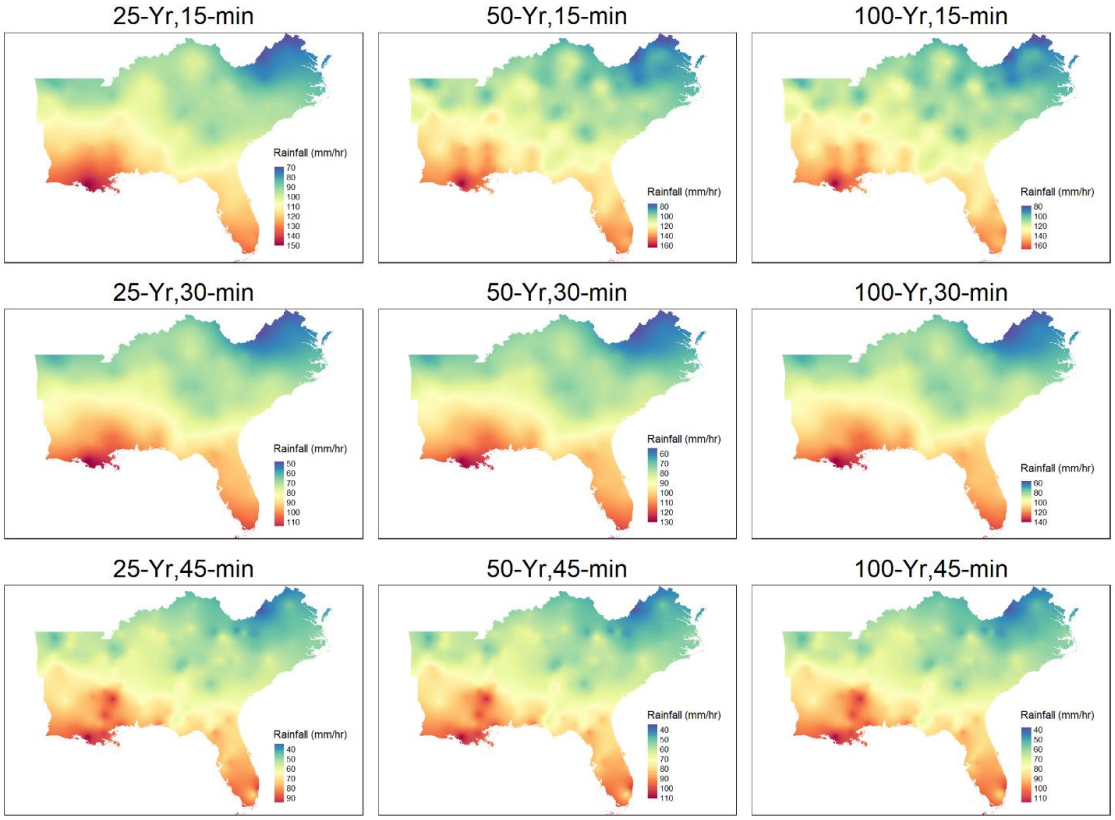
25-Yr,15-min
Rainfall (mm/hr)
70 80 90 100 110 120 130 140 150
50-Yr,15-min
Rainfall (mm/hr)
80 100 120 140 160
100-Yr,15-min
Rainfall (mm/hr)
80 100 120 140 160
25-Yr,30-min
Rainfall (mm/hr)
50 60 70 80 90 100 110
50-Yr,30-min
Rainfall (mm/hr)
60 70 80 90 100 110 120 130
100-Yr,30-min
Rainfall (mm/hr)
60 80 100 120 140
25-Yr,45-min
Rainfall (mm/hr)
40 50 60 70 80 90
50-Yr,45-min
Rainfall (mm/hr)
40 50 60 70 80 90 100 110
100-Yr,45-min
Rainfall (mm/hr)
40 50 60 70 80 90 100 110

Appendix C2

Ensemble IDF curves with 95% confidence interval for historical and future projected under the RCP8.5 scenario with 2-, 5-, 10-, 25-, 50-, and 100-year return periods using ANN

C2.1. Huntsville 1 SSW

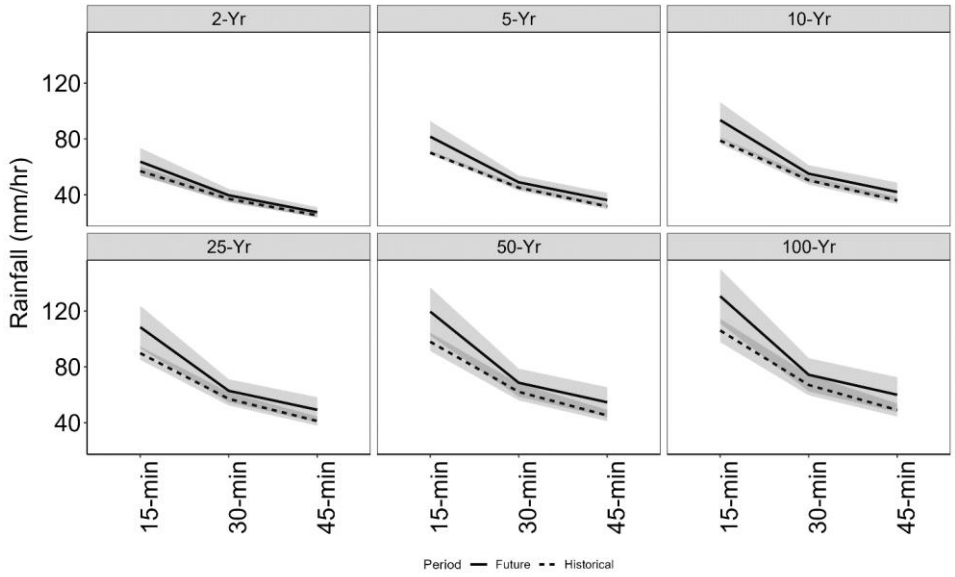

C2.2. Venice

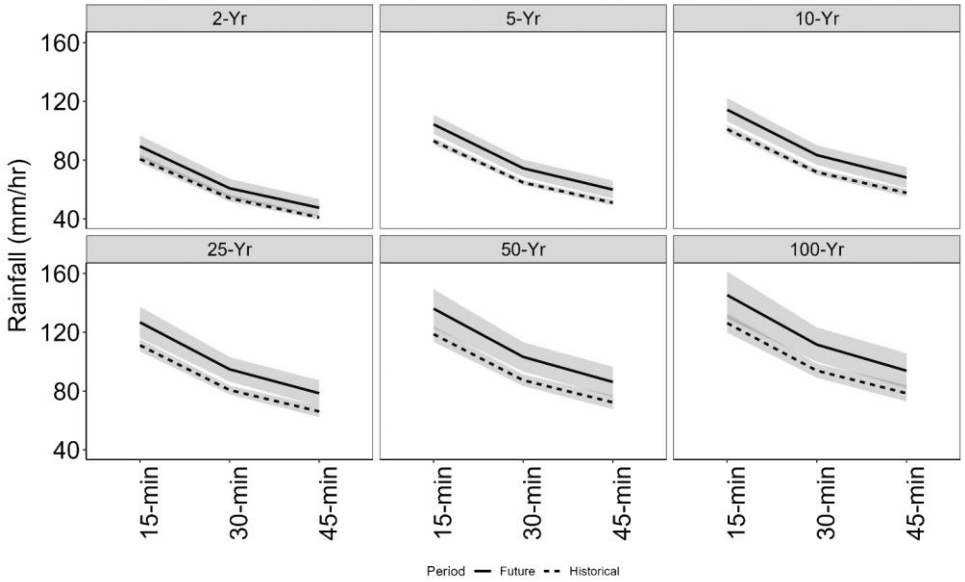

C2.3. New Orleans Audubon

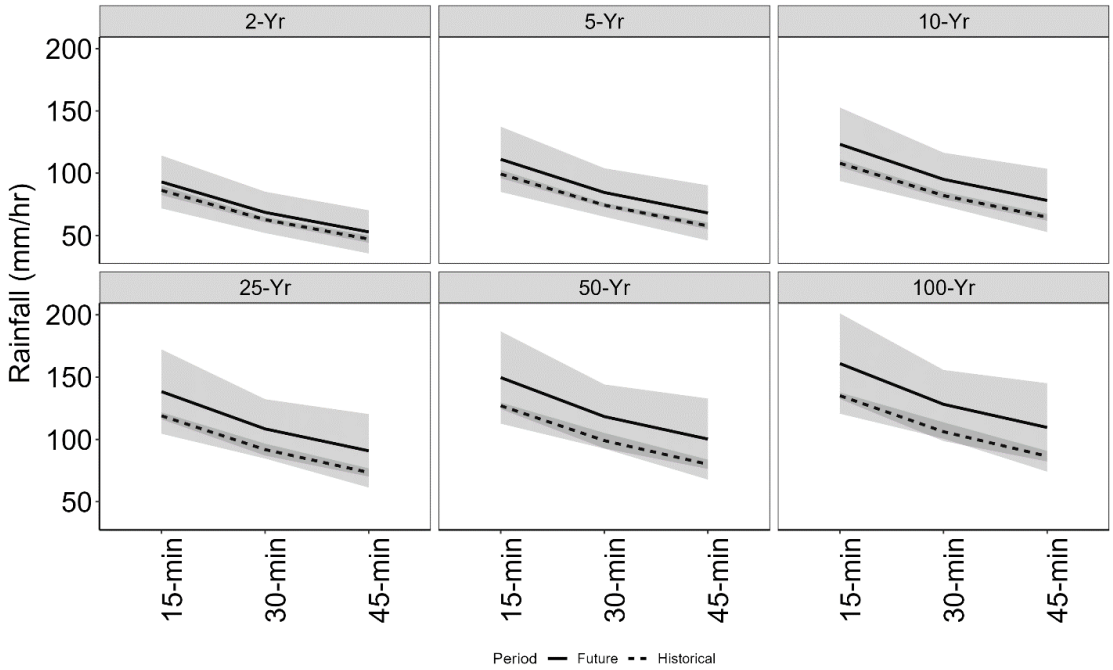

C2.4. Mullins

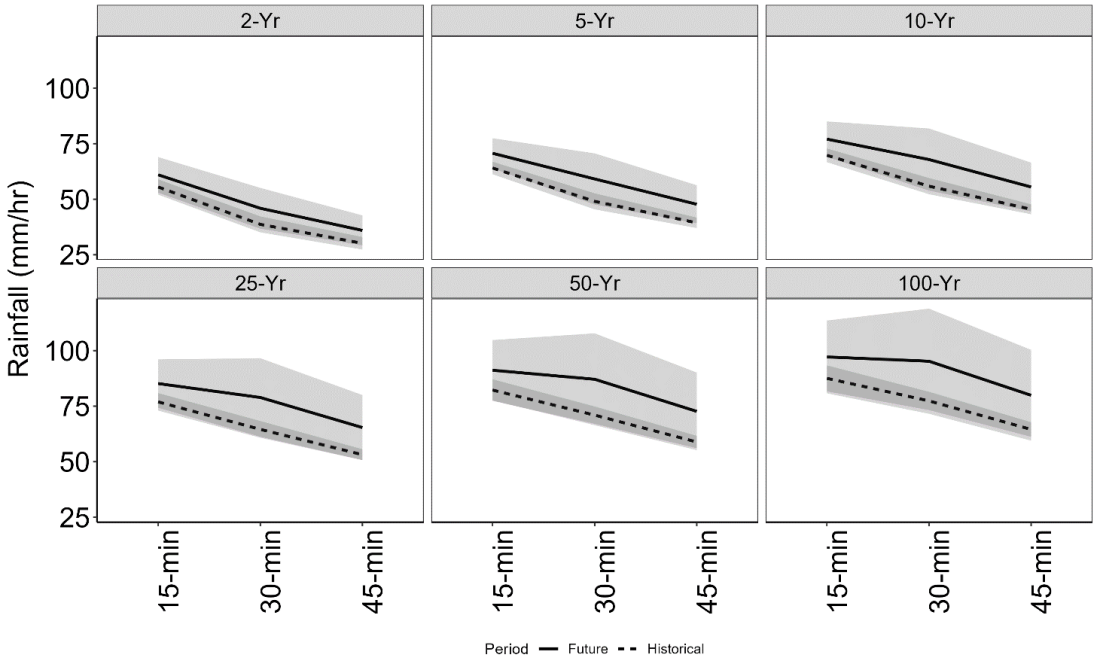

Appendix D1

Plot showing the rainfall Intensity-Duration-Frequency curves using the bootstrapping resampling technique for a site located at Manning, Virginia

D1.1. HADGEM

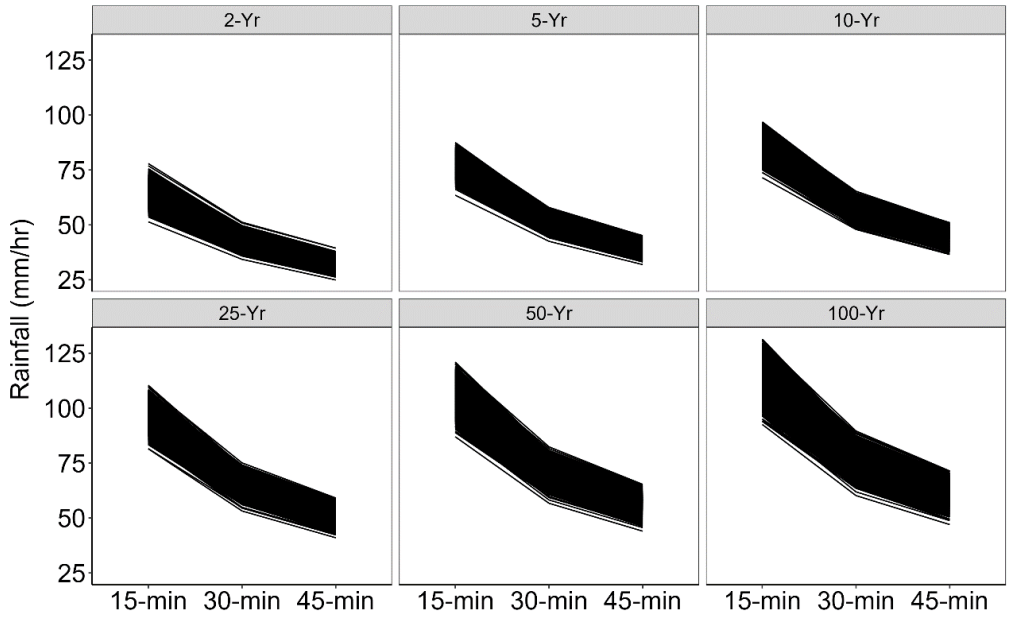

D1.2. GFDL

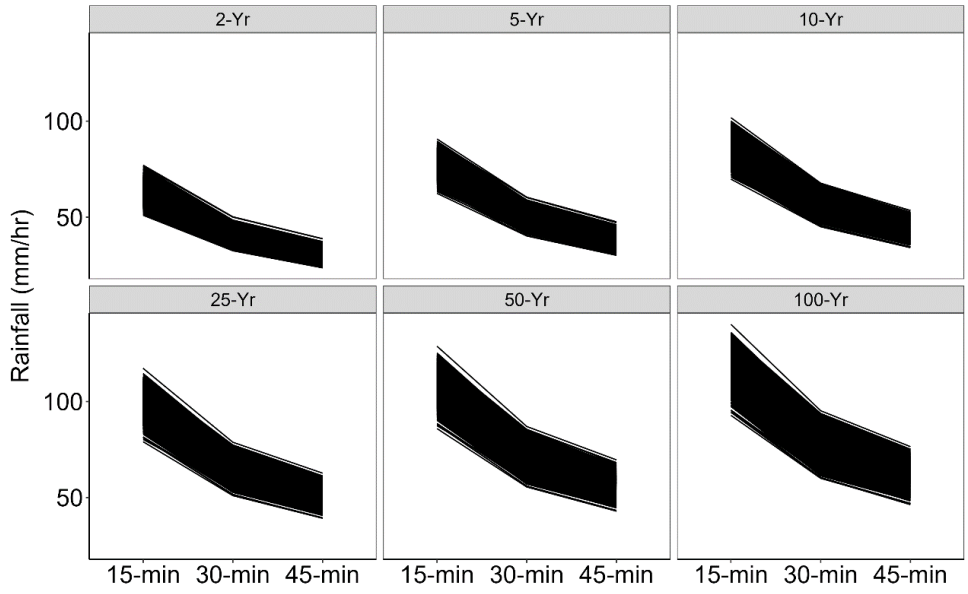

D1.3. MPIREG

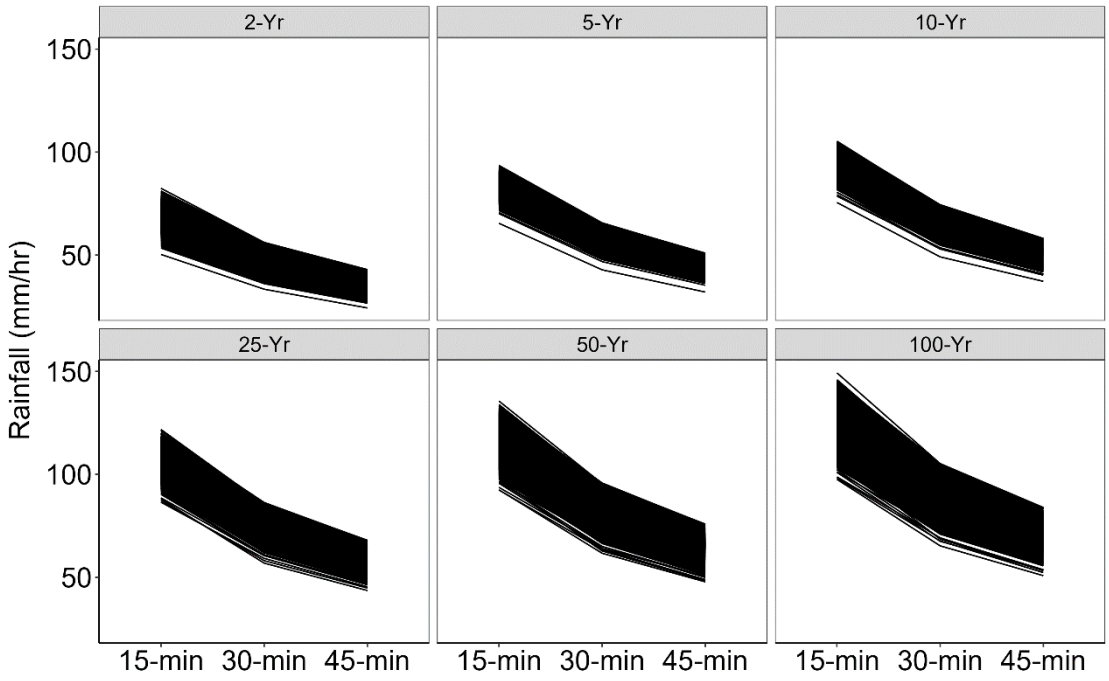

D1.4. MPIWRF

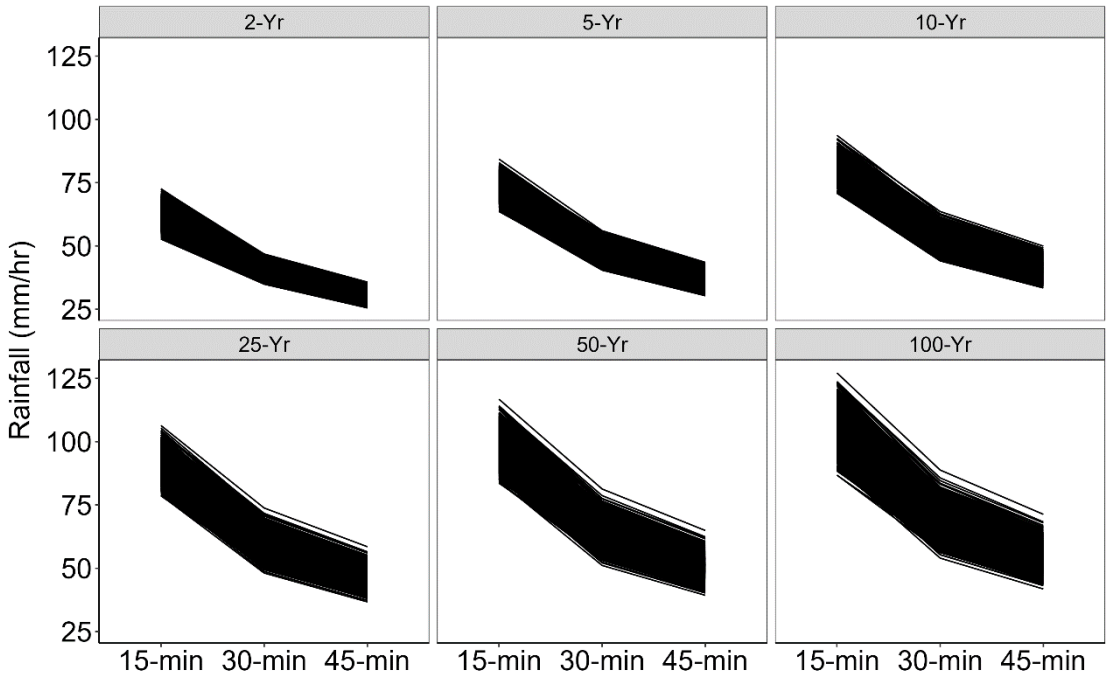

Appendix D2

Boxplots depicting the range of rainfall intensities for periods of 15-, 30-, and 45-min at return periods of 2-, 5-, 10-, 25-, 50-, and 100-Yr for all climate models. Asterisk denotes the average rainfall intensity

D2.1. Warrior, Arkansas

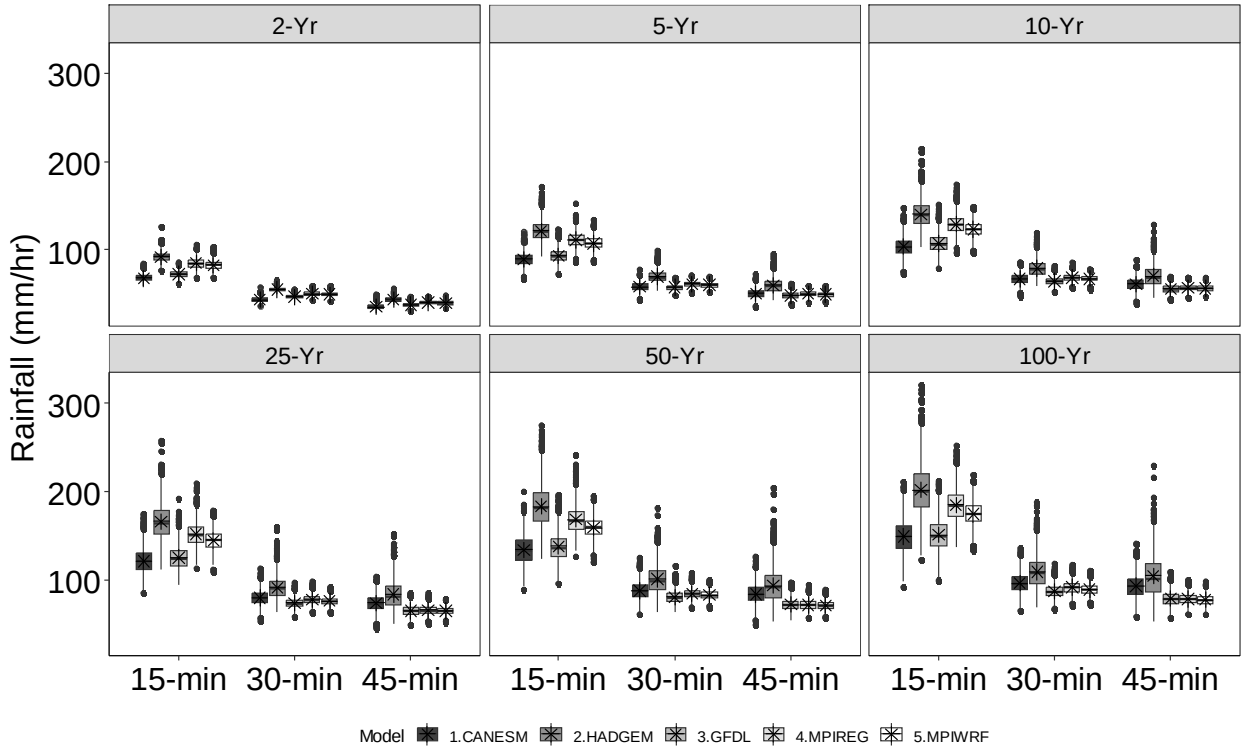

D2.2. Ferndale 6 E, Louisiana

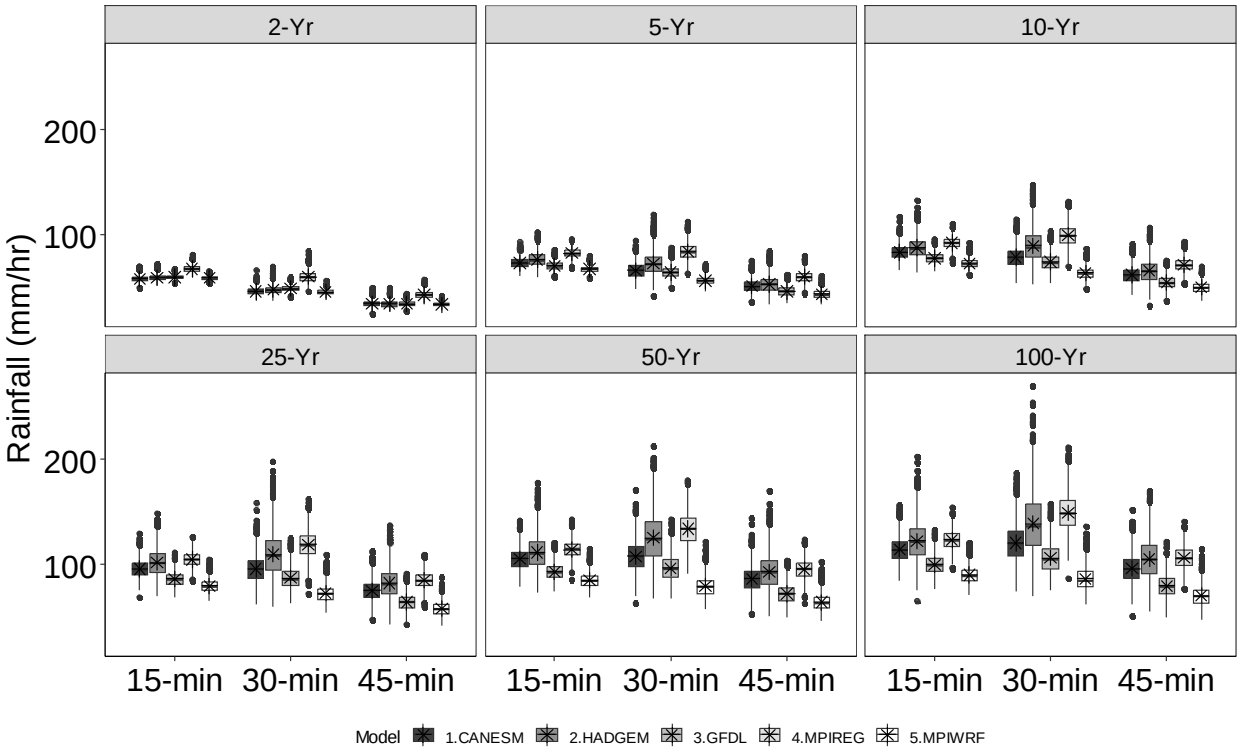

D2.3. Raiford State Prison, Mississippi

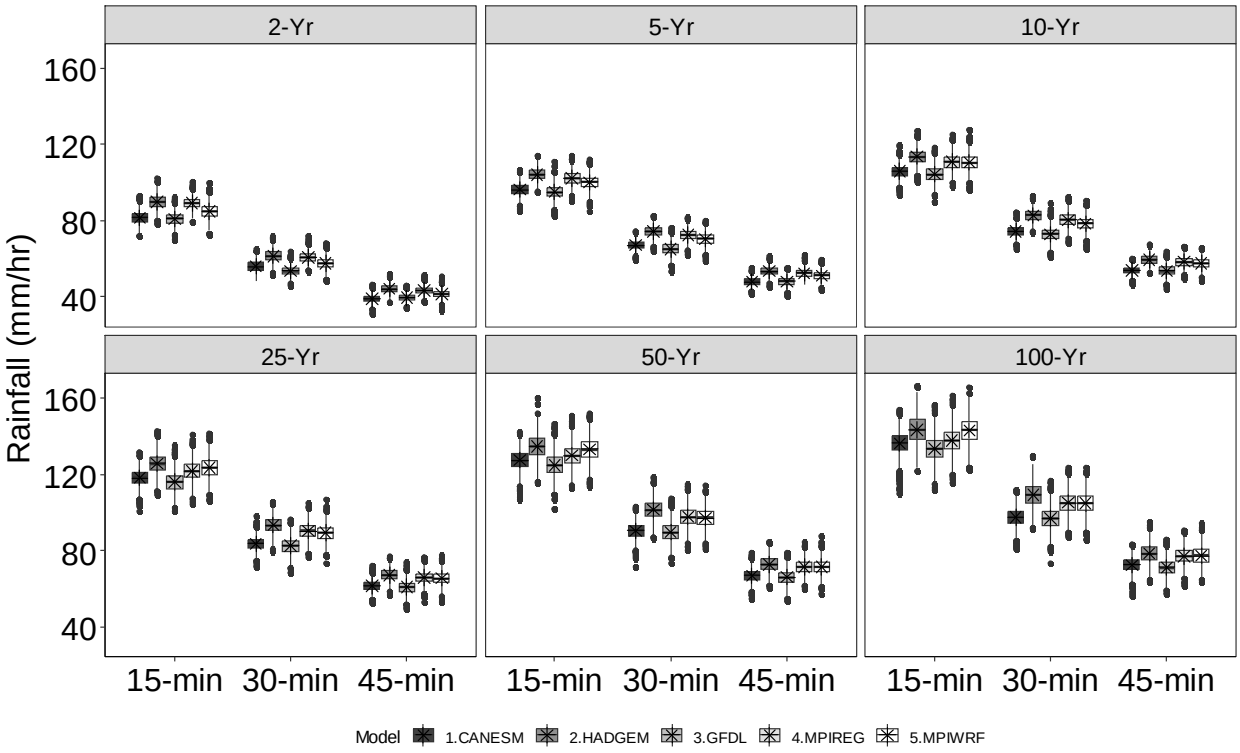

D2.4. Dallas 7 Ne, Alabama

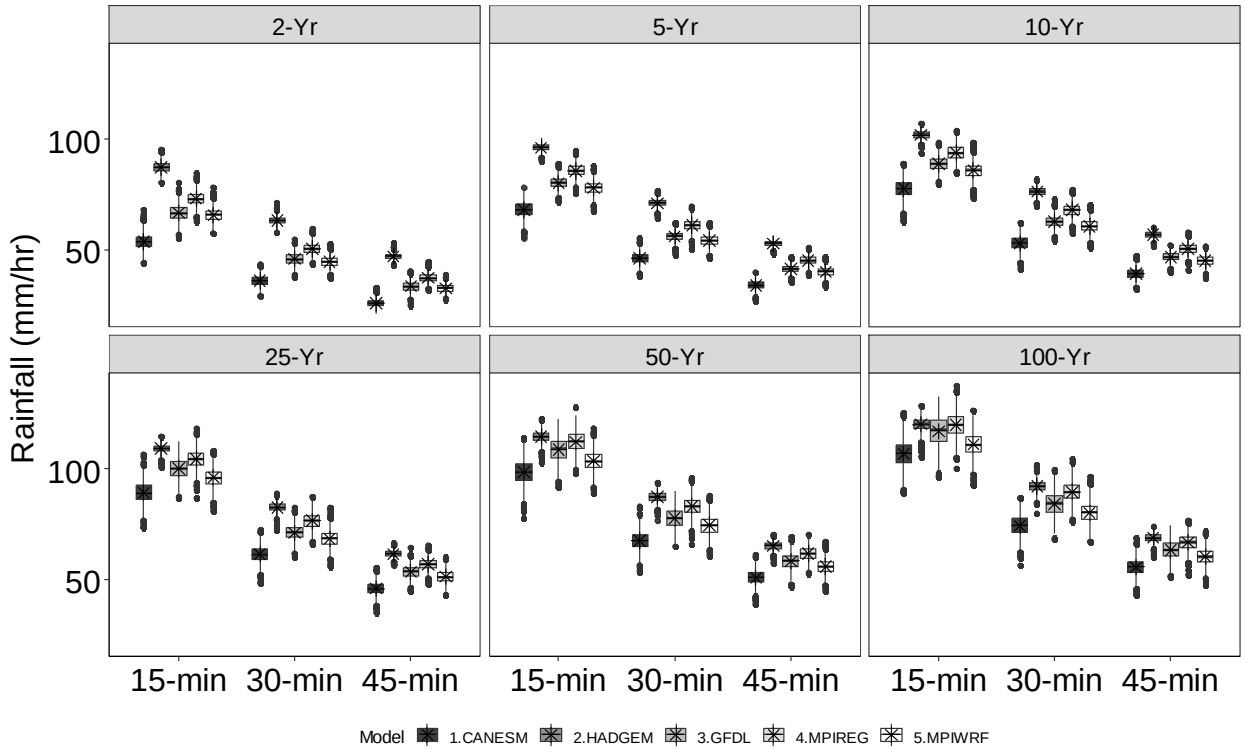

D2.5. Fordsville, Tennessee

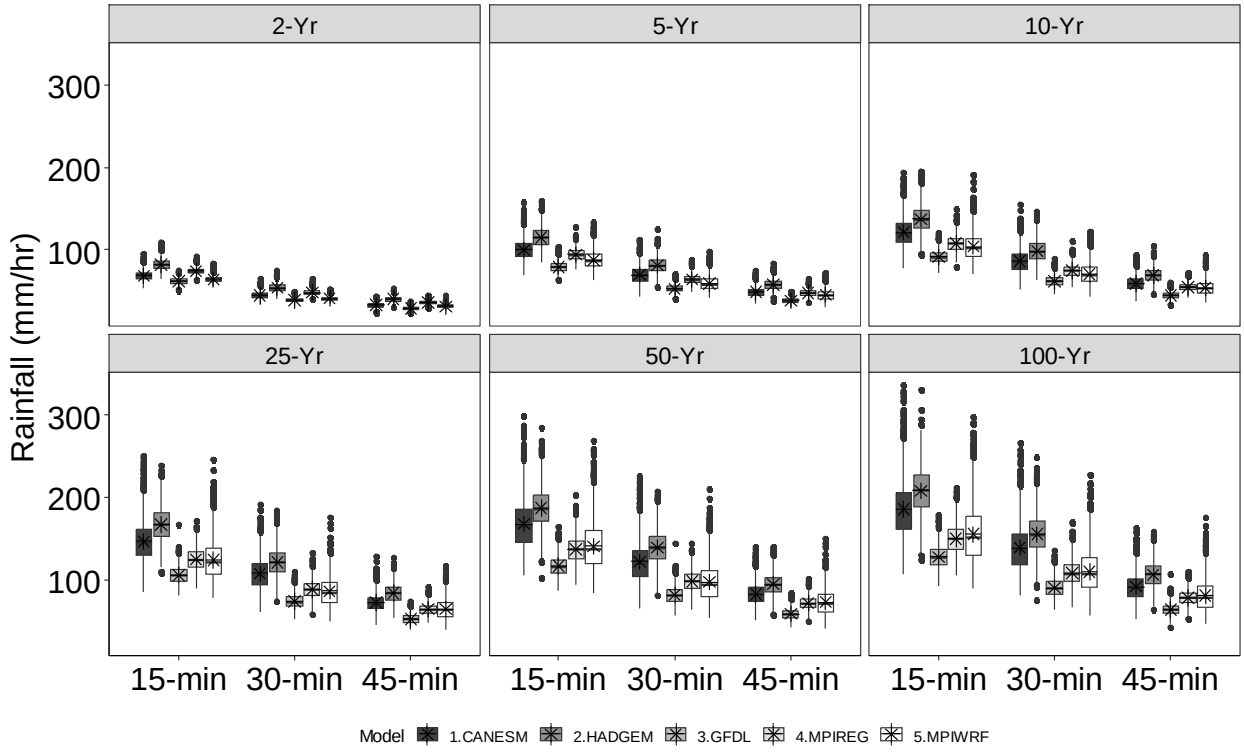

D2.6. New Orleans Audubon, Kentucky

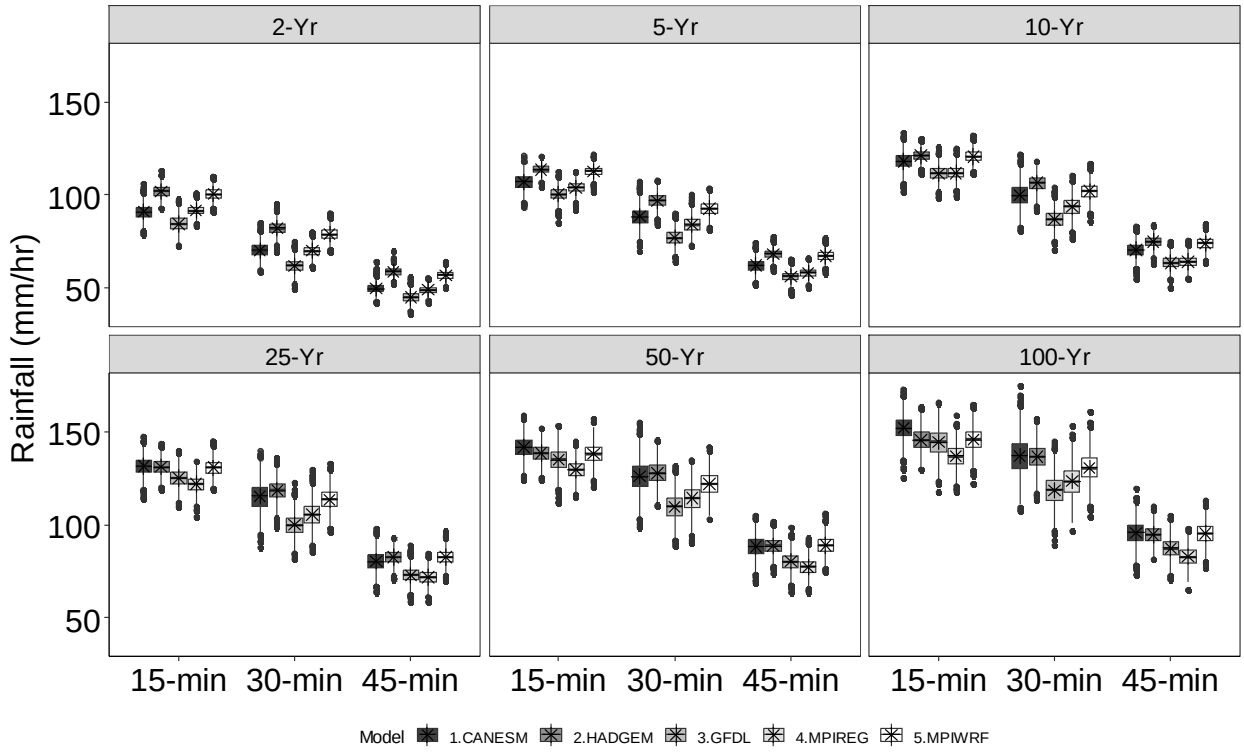

D2.7. Canton 4n, Georgia

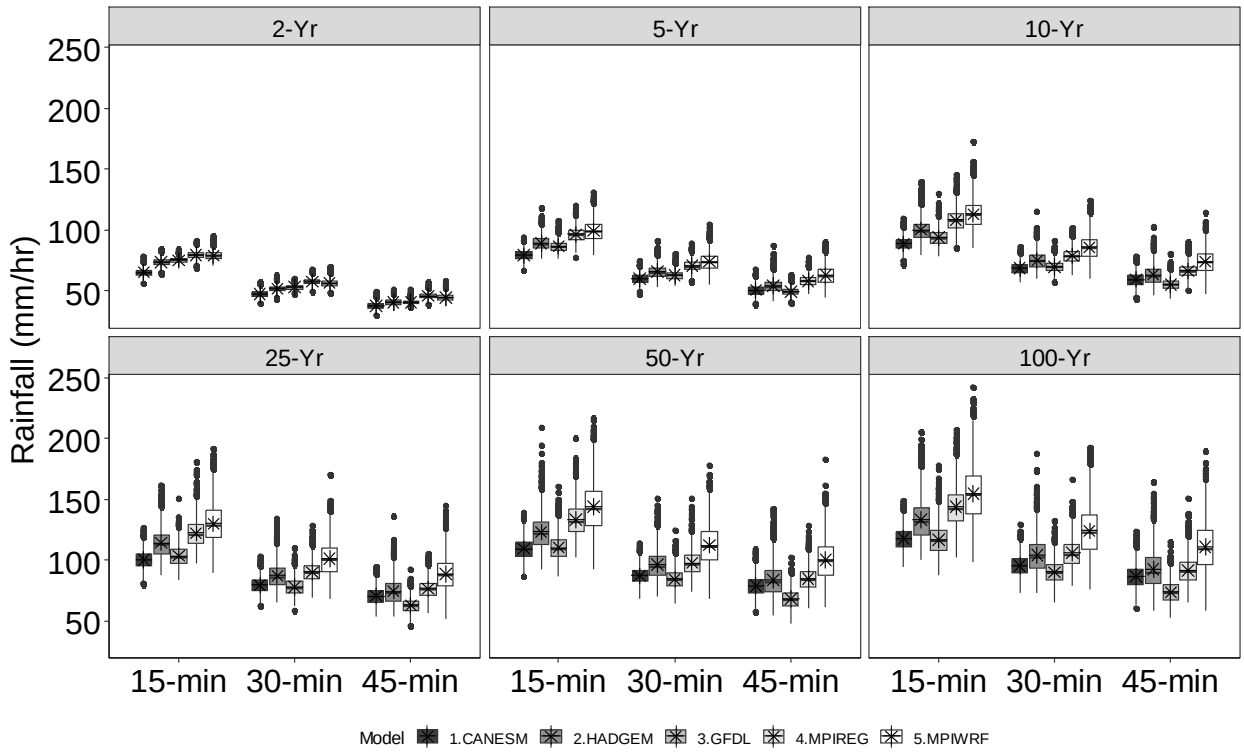

D2.8. Mount Pleasant, Florida

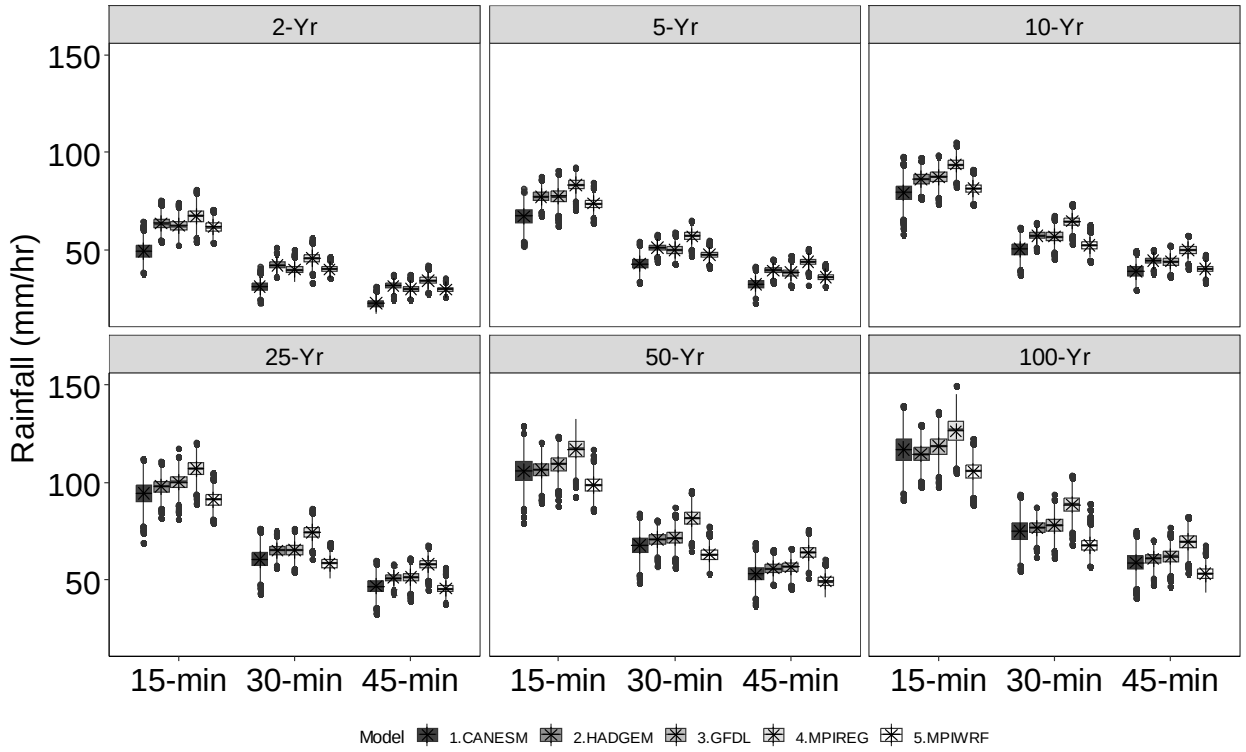

D2.9. Lebanon, North Carolina

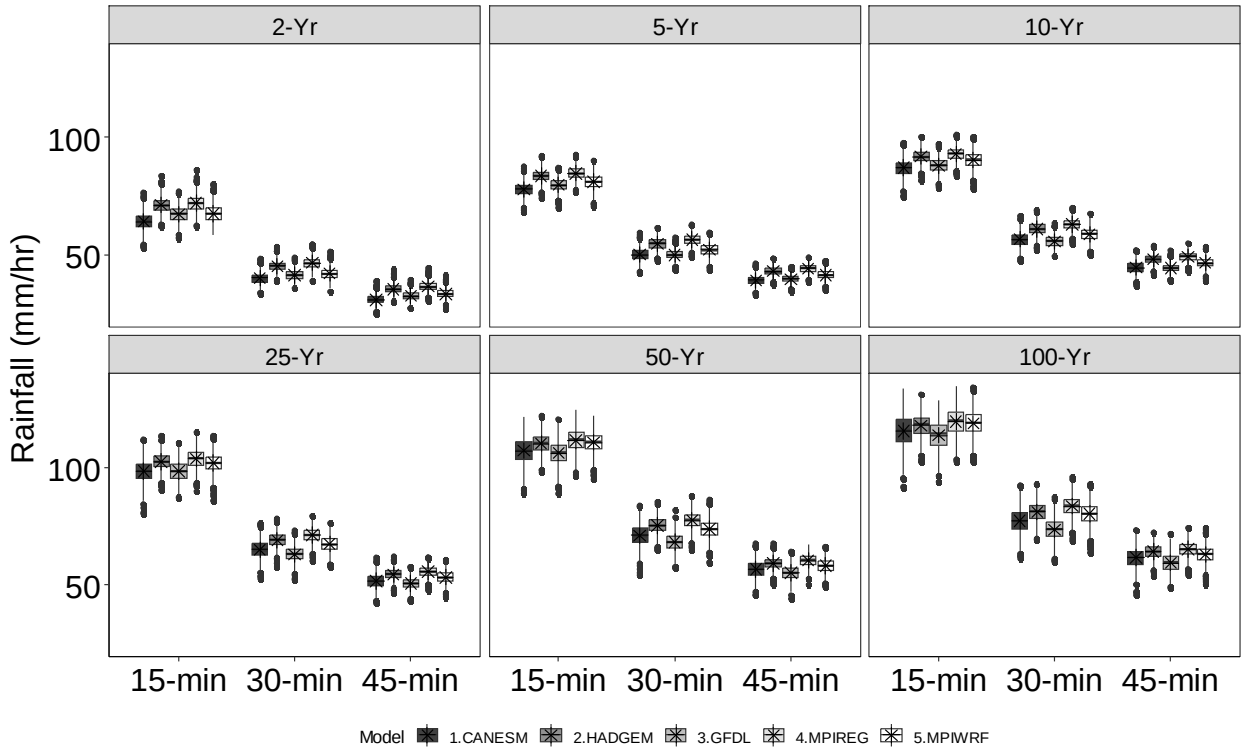

D2.10. Piedmont Research Sta, South Carolina

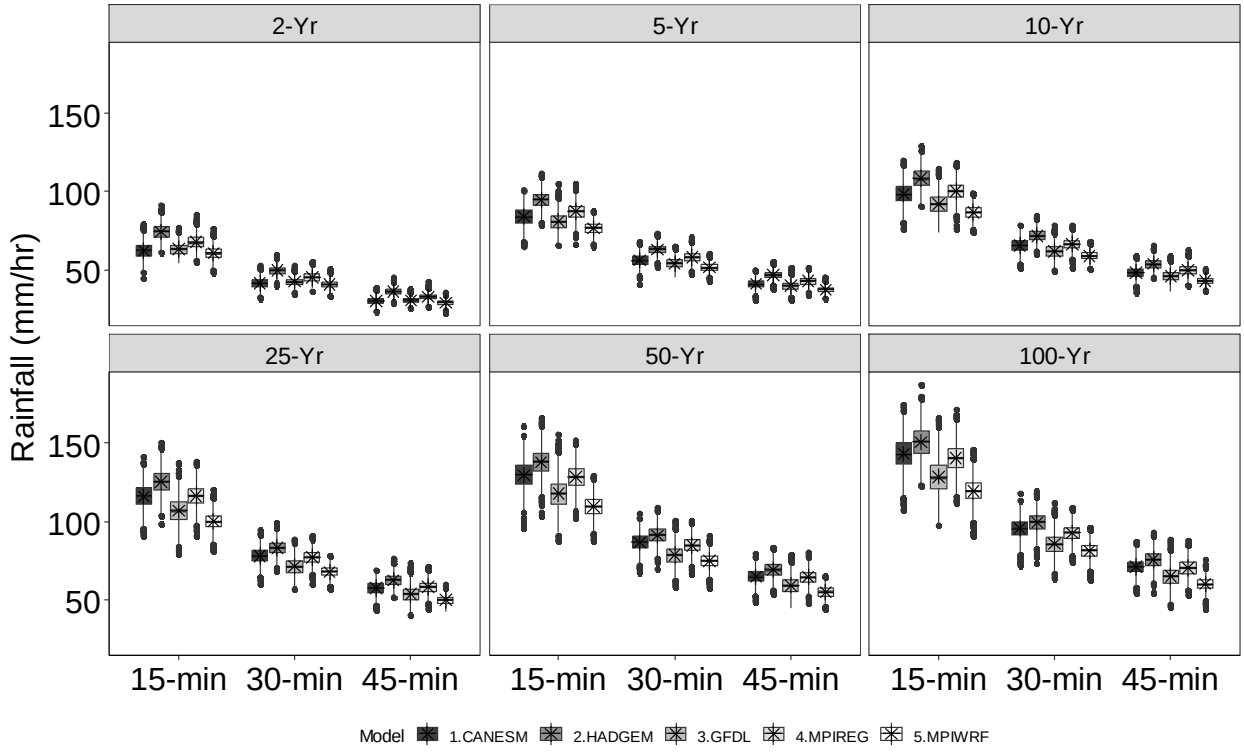

Appendix D3

Summary of annual maximum rainfall intensities with ensemble mean of five climate models for all stations. Median (Med) and mean values are in a range indicating the duration of 15-, 30-, and 45-min with return period of 2-, 5-, 10-, 25-, 50-, and 100-year.

	Annual maximum rainfall Intensity (mm h^{-1})			
Station	**Min**	**Med**	**Mean**	**Max**
1	33	39-171	39-172	243
2	28	36-119	36-120	192
3	34	41-139	41-139	161
4	30	35-115	35-115	130
5	26	34-163	34-165	271
6	44	52-145	52-145	165
7	35	42-132	42-133	196
8	24	30-116	30-116	135
9	28	34-120	35-120	161
10	28	34-117	34-117	132
11	25	32-136	32-136	169